

**Modeling and Experimental Analysis of Biogas
in Diesel and Solid Oxide Fuel Cell Generators**

BY

FRANCESCO QUESITO

Laurea, Politecnico di Torino, Turin, Italy, 2009

THESIS

Submitted as partial fulfilment of the requirements
for the degree of Master of Science in Mechanical Engineering
in the Graduate College of the
University of Illinois at Chicago, 2012

Chicago, Illinois

Defense Committee:

Suresh K. Aggarwal, Chair and Advisor
Kenneth Brezinsky
Massimo Santarelli, Politecnico di Torino

This thesis is dedicated to my father, Franco, without whose support it would never have been accomplished. Dad, thanks for giving me the chance to have what you were prematurely and shamefully deprived of by life. A father, a friend, and the best supporter ever.

ACKNOWLEDGEMENTS

I would like to thank my advisors, Prof. Suresh K. Aggarwal and Prof. Massimo Santarelli, for their assistance and guidance, without which it would have been impossible for me to accomplish my research goals. Also, I really want to thank Dr. Valerio Novaresio for the immense help received in building up the numerical model. A special thanks goes to *Edison S.p.a. – Centro Ricerca e Sviluppo*, Trofarello (Torino, Italy) for giving me the opportunity to improve my working skills; in particular, thanks to Dr. Davide Beretta and Gianfranco Berzovini for their kind assistance while working in the Fuel-Cells Laboratory). Moreover, thanks to Dr. Andrea Lanzini, for the guidance and help received before, while, and after performing the experimental tests, Dr. Cosimo Guerra, for providing the dry-reforming data, and my Combustion-Laboratory mates (Khurram Akber, Abdulhadi Madi, and Sudhanshu Jain), for the constant help received while working in Chicago. Eventually, I want to thank from the bottom of my heart my family and my friends for the unwavering support they always gave me while chasing this challenging but amazing achievement.

FQ

TABLE OF CONTENTS

<u>CHAPTER</u>		<u>PAGE</u>
1.	INTRODUCTION.....	1
	1.1 Motivations and Aims.....	1
	1.2 Biogas Background.....	2
	1.3 Biogas Research and Current Objectives.....	4
2.	BIOGAS COMBUSTION EQUILIBRIUM.....	7
	2.1 Introduction.....	7
	2.1.1 CHEMKIN Overview.....	7
	2.1.2 GRI 3.0 Mechanism.....	8
	2.1.3 Biogas Composition.....	9
	2.2 Combustion Equilibrium Study.....	10
	2.3 Determining Chemical Equilibria with CHEMKIN.....	11
	2.3.1 Minimization of Gibb’s Free Energy.....	12
	2.4 How to perform an Equilibrium Calculation with CHEMKIN.....	13
	2.5 Simulation Results.....	15
	2.5.1 Effect of Main Contaminants on Adiabatic Flame Temperature.....	17
	2.5.2 Influence of Equivalence Ratio on Adiabatic Flame Temperature.....	18
	2.5.3 Influence of Equivalence Ratio on Pollutant Emissions.....	19
3.	BIOGAS LAMINAR PREMIXED FLAMES.....	21
	3.1 Introduction.....	21
	3.2 Physical Description.....	21
	3.3 Analyzing 1-D Laminar Premixed Flames with CHEMKIN.....	23
	3.3.1 1-D Flame Equations.....	24
	3.3.2 Mixture-Averaged Transport Properties.....	25
	3.3.3 Finite Difference Approximations.....	26
	3.3.4 Boundary Conditions.....	28
	3.3.5 Transient Forms of the Equations.....	29
	3.4 How to Perform a Flame-Speed Calculation with CHEMKIN.....	30
	3.5 Simulation Results.....	31
	3.5.1 Flame-Speed Computation.....	37
	3.5.2 Influence of Equivalence Ratio on Flame Speed.....	38
	3.5.3 Methane Experimental Validation.....	39
	3.5.4 High-Pressure Study and Methane Validation.....	41
	3.5.5 Overall Reaction Order and Methane Validation.....	44
4.	BIOGAS PARTIALLY PREMIXED FLAMES.....	46
	4.1 Introduction.....	46
	4.2 Counter-Flow Flames.....	46
	4.3 Analyzing Opposed-flow Diffusion Flames with CHEMKIN.....	48
	4.3.1 Axisymmetric and Planar Diffusion.....	48
	4.3.2 Finite Difference Approximations.....	53
	4.3.3 Regrid Operation.....	53
	4.4 How to Perform an Opposed-Flow-Diffusion-Flame Calculation with CHEMKIN.....	55
	4.5 Simulation Results.....	56
	4.5.1 Best Cases.....	59
	4.5.2 Influence of Strain Rate and Equivalence Ratio.....	70

TABLE OF CONTENTS (continued)

<u>CHAPTER</u>	<u>PAGE</u>
4.5.3 Extraction of Stretched Flame Speed.....	73
4.5.4 Performance Outline.....	77
4.5.5 Dilution Study.....	77
4.5.6 Validation and Further Research.....	81
5. SOFC MODELING AND EXPERIMENTAL SETUP.....	82
5.1 Introduction.....	82
5.1.1 Electrolyte.....	83
5.1.2 Cathode.....	84
5.1.3 Anode.....	85
5.1.4 Interconnect.....	86
5.1.5 Stack Design.....	88
5.2 SOFC Modeling.....	91
5.2.1 Governing Equations.....	92
5.2.2 Finite Difference Approach.....	95
5.2.3 Electrochemistry.....	96
5.2.4 Reaction Mechanism.....	101
5.2.5 Heterogeneous Chemistry on Nickel.....	102
5.2.6 Model Description.....	106
5.3 Experimental Setup.....	109
6. SOFC EXPERIMENTAL SETUP AND MODEL VALIDATION.....	116
6.1 Introduction.....	116
6.2 Dry Reforming.....	116
6.2.1 Polarization Curves.....	116
6.2.2 Influence of Carbon-Dioxide Addition.....	119
6.2.3 Fuel Utilization Maps.....	122
6.2.4 Gas Analysis and Model Validation.....	126
6.2.5 Mole-Fraction Profiles.....	136
6.3 Steam Reforming.....	138
6.3.1 Polarization curves.....	139
6.3.2 Influence of Steam Addition.....	140
6.3.3 Influence of Cell Temperature.....	143
6.3.4 Fuel Utilization Map.....	144
6.3.5 Gas Analysis and Model Validation.....	146
6.3.6 Mole-Fraction Profiles.....	148
7. PERFORMANCE COMPARISON FOR PPF AND SOFC PROCESSES.....	150
8. CONCLUSIONS.....	153
APPENDICES.....	158
Appendix A.....	159
Appendix B.....	177
CITED LITERATURE.....	181
VITA.....	187

LIST OF TABLES

<u>TABLE</u>	<u>PAGE</u>
I. BIOGAS REFERENCE COMPOSITIONS EXPRESSED IN TERMS OF PERCENTAGE MOLE FRACTIONS.....	9
II. EQUILIBRIUM-COMPOSITION MOLE FRACTIONS OF ALL CHEMICAL SPECIES INVOLVED IN THE COMBUSTION PROCESS FOR ALL CONSIDERED FUELS ($\phi = 1, T_{in} = 298 \text{ K}, P = 1 \text{ atm}$).....	16
III. MAIN-POLLUTANT-EMISSIONS COMPARISON BETWEEN METHANE AND BIOGAS 1 AND 2 ($\phi = 1, T_{in} = 298 \text{ K}, P = 1 \text{ atm}$).....	16
IV. LOCATION OF PEAK SPECIES MOLE FRACTIONS AND TEMPERATURES IN SIMULATED METHANE-AIR AND BIOGAS-AIR COUNTER-FLOW DIFFUSION FLAMES ($a_s = 150 \text{ s}^{-1}$ AND $\phi = 1.4$ AT THE FUEL NOZZLE OUTLET).....	62
V. LOCATION OF PEAK SPECIES MOLE FRACTIONS AND TEMPERATURES IN SIMULATED METHANE-AIR AND BIOGAS-AIR COUNTER-FLOW DIFFUSION FLAMES ($a_s = 150 \text{ s}^{-1}$ AND $\phi = 3.0$ AT THE FUEL NOZZLE OUTLET).....	64
VI. LOCATION OF PEAK SPECIES MOLE FRACTIONS AND TEMPERATURES IN SIMULATED METHANE-AIR AND BIOGAS-AIR COUNTER-FLOW DIFFUSION FLAMES ($a_s = 200 \text{ s}^{-1}$ AND $\phi = 1.4$ AT THE FUEL NOZZLE OUTLET).....	66
VII. LOCATION OF PEAK SPECIES MOLE FRACTIONS AND TEMPERATURES IN SIMULATED METHANE-AIR AND BIOGAS-AIR COUNTER-FLOW DIFFUSION FLAMES ($a_s = 200 \text{ s}^{-1}$ AND $\phi = 3.0$ AT THE FUEL NOZZLE OUTLET).....	68
VIII. LOCATION OF PEAK SPECIES MOLE FRACTIONS AND TEMPERATURES IN SIMULATED METHANE-AIR COUNTER-FLOW DIFFUSION FLAMES ($a_s = 150 \text{ s}^{-1}$ AND $\phi = 10$ AT THE FUEL NOZZLE OUTLET).....	70
IX. LIST OF COMBINATIONS FOR THE PRESENT COMPUTATION.....	71
X. PEAK HEAT FLUXES IN W/cm^2 FOR METHANE-AIR AND BIOGAS-AIR COUNTER-FLOW FLAMES.....	77
XI. HETEROGENEOUS REACTION MECHANISM FOR METHANE REFORMING ON NICKEL-BASED CATALYSTS.....	105
XII. LIST OF DRY-REFORMING COMBINATIONS.....	151

LIST OF TABLES (continued)

<u>TABLE</u>		<u>PAGE</u>
XIII.	HEAT GENERATION PER UNIT MASS OF BIOGAS.....	152
XIV.	DRY-REFORMING TESTS: GENERAL INFORMATION.....	177
XV.	TEST 1, 2, 3. MATRIX DESIGN VARIABLE: METHANE FLOW RATE (Nml/min).....	177
XVI.	TEST 4, 5, 6. MATRIX DESIGN VARIABLE: FUEL UTILIZATION FACTOR.....	178
XVII.	STEAM-REFORMING TESTS: GENERAL INFORMATION.....	178
XVIII.	TEST 1. MATRIX DESIGN VARIABLE: METHANE FLOW RATE (Nml/min).....	179
XIX.	TEST 2. MATRIX DESIGN VARIABLE: FUEL UTILIZATION FACTOR.....	179
XX.	TEST 3, 4, 5. MATRIX DESIGN VARIABLES: STEAM-TO-BIOGAS RATIO AND CELL TEMPERATURE ($T_{cell} = 800, 750, 700^{\circ}\text{C}$).....	180

LIST OF FIGURES

<u>FIGURE</u>	<u>PAGE</u>
1. Effect of contaminants on adiabatic flame temperature ($\phi = 1, T_{in} = 500 \text{ K}, P = 1 \text{ atm}$).....	18
2. Effect of equivalence ratio on adiabatic flame temperature ($\phi = 1, T_{in} = 500 \text{ K}, P = 1 \text{ atm}$).....	19
3. Influence of equivalence ratio on carbon-monoxide emissions ($\phi = 1, T_{in} = 500 \text{ K}, P = 1 \text{ atm}$).....	20
4. Temperature, axial-velocity, heat generation, and selected species mole-fraction profiles for methane-air and biogas-air laminar premixed flames ($\phi = 1, T_{in} = 298 \text{ K}, P = 1 \text{ atm}$).....	33
5. NO_x -emission-index analysis ($\phi = 1, T_{in} = 298 \text{ K}, P = 1 \text{ atm}$).....	37
6. Flame speed of considered fuels ($\phi = 1, T_{in} = 298 \text{ K}, P = 1 \text{ atm}$).....	38
7. Influence of equivalence ratio on flame speed ($T_{in} = 298 \text{ K}, P = 1 \text{ atm}$).....	39
8. Experimental validation for the methane case ($P = 1 \text{ atm}$).....	40
9. Experimental validation for the methane case ($P = 2 \text{ atm}$).....	40
10. Experimental validation for the methane case ($P = 5 \text{ atm}$).....	41
11. Flame speed of considered fuels for pressures up to 50 atm ($\phi = 1, T_{in} = 300 \text{ K}$).....	42
12. Experimental validation for the methane case in the range 1-3 atm ($\phi = 1, T_{in} = 300 \text{ K}$).....	43
13. Experimental validation for the methane case in the range 1-20 atm ($\phi = 1, T_{in} = 300 \text{ K}$).....	44
14. Overall reaction order for a methane-air mixture for pressures up to 40 atm ($\phi = 1, T_{in} = 300 \text{ K}$).....	45
15. Experimental validation for the methane case for pressures up to 3 and 20 atm, respectively ($\phi = 1, T_{in} = 300 \text{ K}$).....	45
16. Counter-flow flame configuration. Diffusion flame lies above stagnation plane (dashed line) created by opposing streams of fuel and oxidizer.....	48

LIST OF FIGURES (continued)

<u>FIGURE</u>		<u>PAGE</u>
17.	Geometry of the axisymmetric opposed-flow diffusion flame. The dashed line represents the stagnation flame; the shaded region suggests the flame....	49
18.	Geometry of the planar opposed-flow diffusion flame. The dashed line represents the stagnation flame; the shaded region suggests the flame.....	50
19.	Temperature and axial-velocity profiles for methane-air and biogas-air counter-flow flames ($\phi = 1$, $T_{inlet} = 300$ K, $P = 1$ atm, $a_s = 150$ s ⁻¹).....	57
20.	Mole-fraction profiles of main chemical species for methane-air counter-flow flames ($\phi = 1$, $T_{inlet} = 300$ K, $P = 1$ atm, $a_s = 150$ s ⁻¹).....	59
21.	Temperature, axial-velocity, and mole-fraction profiles of main chemical species for methane-air and biogas-air counter-flow flames ($\phi = 1.4$, $T_{inlet} = 300$ K, $P = 1$ atm, $a_s = 150$ s ⁻¹).....	61
22.	Temperature, axial-velocity, and mole-fraction profiles of main chemical species for methane-air and biogas-air counter-flow flames ($\phi = 3.0$, $T_{inlet} = 300$ K, $P = 1$ atm, $a_s = 150$ s ⁻¹).....	63
23.	Temperature, axial-velocity, and mole-fraction profiles of main chemical species for methane-air and biogas-air counter-flow flames ($\phi = 1.4$, $T_{inlet} = 300$ K, $P = 1$ atm, $a_s = 200$ s ⁻¹).....	65
24.	Temperature, axial-velocity, and mole-fraction profiles of main chemical species for methane-air and biogas-air counter-flow flames ($\phi = 3.0$, $T_{inlet} = 300$ K, $P = 1$ atm, $a_s = 200$ s ⁻¹).....	67
25.	Temperature, axial-velocity, and mole-fraction profiles of main chemical species for methane-air counter-flow flames ($\phi = 10$, $T_{inlet} = 300$ K, $P = 1$ atm, $a_s = 150$ s ⁻¹).....	69
26.	Effect of strain-rate and equivalence-ratio variations on methane-air counter-flow flames for all considered cases ($T_{inlet} = 300$ K, $P = 1$ atm)....	72
27.	Carbon-monoxide-emission profiles for methane-air and biogas-air counter-flow flames ($\phi = 1$, $T_{inlet} = 298$ K, $P = 1$ atm, $a_s = 150$ s ⁻¹).....	74
28.	Extracted flame speed for methane-air and biogas-air counter-flow flames ($\phi = 1$, $T_{inlet} = 298$ K, $P = 1$ atm, $a_s = 150$ s ⁻¹).....	74

LIST OF FIGURES (continued)

<u>FIGURE</u>	<u>PAGE</u>	
29.	Influence of strain rate ($a_s = 150 \text{ s}^{-1}$ for a and c , $a_s = 200 \text{ s}^{-1}$ for b) and equivalence ratio ($\phi = 1.4$ for a and b , $\phi = 3$ for c) on extracted flame speed for methane-air and biogas-air counter-flow flames ($T_{inlet} = 298 \text{ K}$, $P = 1 \text{ atm}$).....	76
30.	Carbon-dioxide-dilution curves for both the fuel-stream-dilution (a) and the air-stream-dilution (b) case for all considered fuels ($\phi = 1.4$, $T_{inlet} = 300 \text{ K}$, $P = 1 \text{ atm}$, $a_s = 150 \text{ s}^{-1}$).....	78
31.	Influence of strain rate on carbon-dioxide-dilution curves for the fuel-stream-dilution case when burning methane ($\phi = 1.4$, $T_{inlet} = 300 \text{ K}$, $P = 1 \text{ atm}$).....	79
32.	Nitrogen-dilution curves for both the fuel-stream-dilution (a) and the air-stream-dilution (b) case for all considered fuels ($\phi = 1.4$, $T_{inlet} = 300 \text{ K}$, $P = 1 \text{ atm}$, $a_s = 150 \text{ s}^{-1}$).....	80
33.	Influence of strain rate on nitrogen-dilution curves for the fuel-stream-dilution case when burning methane ($\phi = 1.4$, $T_{inlet} = 300 \text{ K}$, $P = 1 \text{ atm}$).....	81
34.	Operating principle of a solid oxide fuel cell.....	83
35.	Illustration of planar cell stacks (top) and a tubular cell bundle (bottom).....	89
36.	Alternative tubular geometry cells being developed by Siemens.....	91
37.	Radial-wedge-to-rectangular-channel approximation.....	107
38.	Scheme of the tubular SOFC test rig showing the basic P&ID.....	110
39.	Acumentrics SOFC Test Stand.....	111
40.	Acumentrics tubular SOFC.....	112
41.	Polarization curves for different methane mass flow rates when carbon dioxide-to-biogas ratio is set to 1.....	117
42.	Polarization curves for different methane mass flow rates when carbon dioxide-to-biogas ratio is set to 1.5.....	118
43.	Polarization curves for different methane mass flow rates when carbon dioxide-to-biogas ratio is set to 2.....	118

LIST OF FIGURES (continued)

<u>FIGURE</u>		<u>PAGE</u>
44.	Polarization curves for different carbon dioxide-to biogas ratios when methane mass flow rate is set to 60 Nml/min.....	120
45.	Voltage polarization curve for different carbon dioxide-to biogas ratios when methane mass flow rate is set to 80 Nml/min.....	121
46.	Voltage polarization curve for different carbon dioxide-to biogas ratios when methane mass flow rate is set to 140 Nml/min.....	121
47.	Voltage polarization curve for different carbon dioxide-to biogas ratios when methane mass flow rate is set to 160 Nml/min.....	122
48.	Efficiency map when carbon dioxide-to-biogas ratio is set to 1.....	123
49.	Efficiency map when carbon dioxide-to-biogas ratio is set to 1.5.....	124
50.	Efficiency map when carbon dioxide-to-biogas ratio is set to 2.....	124
51.	Mole-fraction comparison for main dry-gas species when carbon dioxide-to-biogas ratio is set to 1 (OCV configuration).....	128
52.	Mole-fraction comparison for main dry-gas species when carbon dioxide-to-biogas ratio is set to 1.5 (OCV configuration).....	128
53.	Mole-fraction comparison for main dry-gas species when carbon dioxide-to-biogas ratio is set to 2 (OCV configuration).....	129
54.	Mole-fraction comparison for main dry-gas species when carbon dioxide-to-biogas ratio is set to 1 ($I = 15\text{ A}$, $FU = 50\%$).....	131
55.	Mole-fraction comparison for main dry-gas species when carbon dioxide-to-biogas ratio is set to 1.5 ($I = 15\text{ A}$, $FU = 50\%$).....	132
56.	Mole-fraction comparison for main dry-gas species when carbon dioxide-to-biogas ratio is set to 2 ($I = 15\text{ A}$, $FU = 50\%$).....	132
57.	Mole-fraction comparison for main dry-gas species when carbon dioxide-to-biogas ratio is set to 1.5 ($I = 25\text{ A}$, $FU = 50\%$).....	134
58.	Mole-fraction comparison for main dry-gas species when carbon dioxide-to-biogas ratio is set to 1.5 ($I = 15\text{ A}$, $FU = 25\%$).....	134
59.	Predicted mole-fraction profiles of main chemical species when carbon dioxide-to-biogas ratio is set to 1 (OCV configuration).....	136
60.	Predicted mole-fraction profiles of main chemical species when carbon dioxide-to-biogas ratio is set to 1.5 (OCV configuration).....	137

LIST OF FIGURES (continued)

<u>FIGURE</u>		<u>PAGE</u>
61.	Predicted mole-fraction profiles of main chemical species when carbon dioxide-to-biogas ratio is set to 1 ($I = 15 A$, $FU = 50\%$).....	138
62.	Polarization curves for different methane mass flow rates when steam-to-biogas ratio is set to 0.3 ($T = 800^{\circ}C$).....	139
63.	Polarization curves for different steam-to biogas ratios when methane mass flow rate is set to 100 Nml/min ($T = 800^{\circ}C$).....	141
64.	Polarization curves for different steam-to biogas ratios when methane mass flow rate is set to 100 Nml/min ($T = 750^{\circ}C$).....	141
65.	Polarization curves for different steam-to biogas ratios when methane mass flow rate is set to 100 Nml/min ($T = 700^{\circ}C$).....	142
66.	Polarization curves for different cell temperatures when methane mass flow rate is set to 100 Nml/min (steam-to-biogas ratio is set to 0.3).....	143
67.	Efficiency map when steam-to-biogas ratio is set to 0.3 ($T = 800^{\circ}C$).....	144
68.	Mole-fraction comparison for main dry-gas species when methane mass flow rate is set to 150 Nml/min (steam-to-biogas ratio equal to 0.3, OCV configuration, $T = 800^{\circ}C$).....	147
69.	Mole-fraction comparison for main dry-gas species when methane mass flow rate is set to 200 Nml/min (steam-to-biogas ratio equal to 0.3, OCV configuration, $T = 800^{\circ}C$).....	147
70.	Predicted mole-fraction profiles of main chemical species when methane mass flow rate is set to 200 Nml/min (steam-to-biogas ratio equal to 0.3, OCV configuration, $T = 800^{\circ}C$).....	149

SUMMARY

Biogas is a green fuel generally produced by agricultural or household waste, whose range of applications has become wider and wider in recent years. The present work is divided into two parts which cover two different fields of application, by investigating both chemical and electrochemical energy production through the use of biogas. On one hand, the first part presents an extensive *CHEMKIN* simulation analysis of biogas when involved in multiple combustion processes, with equilibrium composition, laminar premixed flames, and partially premixed flames being the main topics to be covered. On the other hand, the second part includes a wide experimental analysis of biogas when directly feeding a tubular anode-supported fuel cell provided by *Edison S.p.a.- Centro Ricerca e Sviluppo*, Trofarello (Torino, Italy), as well as the implementation and validation of a numerical model developed with *Cantera* and *MATLAB* for predicting the final composition of the anode exhaust gases and the mole-fraction profiles of main chemical species along the anode channel.

CHAPTER 1

INTRODUCTION

1.1 Motivations and Aims

The present work aims to show how biogas may represent an important and precious alternative to conventional methane in feeding multiple types of machines apt to produce energy through both the traditional and consolidated thermal machines (whose operation is based on a series of chemical reactions) and the innovative and promising electrochemical generators (exploiting electrochemical reactions). Biogas could play an important role for both energy pathways, even though they are significantly different from each other, and may create a great interest when investigating which of the two paths could lead to the best future perspectives.

In particular, the intent of the first part of this study is to outline how biogas can successfully be used in diesel generators as an effective alternative to methane, whose behavior when feeding diesel engines has been extensively studied in recent years. This can be demonstrated by carrying out a complete simulation analysis on biogas flames, in order to make an extensive and detailed comparison between biogas and methane, and to evaluate all quantities of interest in a way that covers and connects all crucial aspects. In fact, flame structure, heat production, and emissions of pollutants are the main fields to be investigated, in order to point out how biogas may be capable to guarantee performances which are close to those of methane by considerably breaking down emissions at the same time. The most important topic to be covered is the study of biogas partially premixed flames, since it is well-known that PPFs widely occur in diesel generators, where fuel ignites by being premixed with compressed air inside the combustion chamber. A simulation study on biogas capable to show good performances and low emissions could represent a first important step towards a wider analysis upon the use of biogas in actual diesel generators.

On the other hand, the second part of the present work aims to show how biogas can successfully be used to directly feed solid oxide fuel cells for electrochemically producing energy. In fact, SOFCs do not present the need of being fed with pure hydrogen, since they have the capability to internally reform biogas by mixing it either with carbon dioxide (dry reforming) or with water (steam reforming). In order to analyze the effectiveness of biogas internal reforming in SOFCs, a detailed numerical model based on pre-existent literature may be built up to evaluate the cell chemistry and validated through a series of experimental tests performed on a tubular anode-supported SOFC. The main intent is to acquire multiple data for different operational conditions, in order to draw performance maps of the cell, investigate the trend of main quantities, and analyze the influence of main variables. At the same time, we want to perform a deep gas analysis on the cell by collecting exhaust gases and analyzing them through a gas chromatograph. Once all data are acquired and properly post-processed, the numerical model can be validated. Consequently, a powerful tool to predict the cell behavior will be available for any further research.

1.2 Biogas Background

The term biogas typically refers to a gas produced by biological breakdown of organic matter in an oxygen-free environment^[1]. In particular, it is produced by anaerobic digestion or fermentation of biodegradable materials. The primary sources include biomass, green waste, plant material, manure, sewage, municipal waste and energy crops. Biogas is produced as a landfill gas (LFG) by using anaerobic digesters (plants that can be fed with energy crops such as maize silage, sewage sludge or food waste). The waste is put into an air-tight tank, it is covered and mechanically compressed by the weight of the material deposited above. This material prevents oxygen exposure thus allowing anaerobic microbes to thrive so that biogas can be released and collected. Composition of biogas may vary depending on the source and production process. In general, the major constituents are methane with concentrations of 50-75%, carbon dioxide with

concentrations of 25-40%, nitrogen with concentrations of 0-10% and small amounts of water vapour, oxygen, hydrogen and hydrogen sulphide. In some cases it can also contain siloxanes (formed from anaerobic decomposition of materials commonly found in soaps and detergents), ammonia, aromatic compounds and other substances that can also be hazardous for human health. During combustion of biogas containing siloxanes, silicon is released and can combine with free oxygen producing deposits which contain mostly silica or silicates, calcium, sulphur, zinc and phosphorus. Available technologies to remove siloxane deposits can be very expensive and difficult to perform. However, if the deposits exceed a certain threshold so that the operation is affected, their removal may be strictly necessary.

Since raw biogas is often of insufficiently high quality (for instance, in some cases the corrosive nature of hydrogen sulphide can completely destroy the internals of a power plant), biogas is upgraded or purified by a process able to absorb and scrub contaminants in the raw biogas stream. There are three main methods of biogas upgrading: water washing, pressure swing absorption and chemical treatment. Water washing is generally the most commonly used: a high-pressure gas flows into a column where carbon dioxide and other contaminants are scrubbed by cascading water running counter-flow to the gas. This solution can deliver up to 98% of methane by taking roughly 3-6% of the total energy that is chemically available in the final gas. Moreover, sometimes methane within biogas can be concentrated via a biogas upgrader to the standards of natural gas and becomes biomethane, that can be used in local gas distribution networks. Applications for biogas vary from electricity production to cooking, space heating, water heating and process heating. If compressed, biogas can replace compressed natural gas for vehicles, where it can feed an internal combustion engine or a system of fuel cells.

Biogas represents a renewable fuel and its utilization could address several energy and environmental issues. In the United States, biogas would generate enough electricity to meet up to 3% of the continent's electricity need and could potentially help reduce global climate change. Furthermore, manure that is left to decompose releases nitrous dioxide and methane, which are

hazardous gases that warm up the atmosphere more than carbon dioxide. A single cow could produce enough manure in one day to generate 3 KWh of electricity through the conversion of manure into biogas. According to a Webber and Cuellar 2008 study^[2], we could reduce 99 million metric tons of greenhouse gas emissions or about 4% of the greenhouse gases produced in the United States.

1.3 Biogas Research and Current Objectives

As most of chemical and engineering research has suggested in recent years, biogas may be an important alternative to conventional fuels in producing energy. In particular, the high methane content in its composition (depending on the primary source used for production) makes biogas a direct alternative to methane itself. In this sense, comparisons between biogas and methane come easy in order to better evaluate biogas potentiality and properties.

Among the most interesting applications, we can mention the use of biogas in running internal combustion engines for power and heat generation. In particular, feeding diesel engines with biogas has lately become an up-and-coming issue, since the latter engines present good characteristics to be modified for dual-fuel operation. Dual-fuel engines offer higher efficiencies than their spark-ignited counterparts, and this is basically due to the higher compression ratio reached. A higher efficiency results in a decrease of the fuel consumption and the polluting emissions (i.e., nitrogen and carbon oxides), and less particulate is released unlike diesel engines. Several experimental investigations have been performed so far for different types of diesel engines (for single-cylinder^{[3],[4]}, two-cylinder^[5], and four-cylinder engines^[6]) fed with biogas, with engine performances, exhaust emission characteristics, fuel consumption, and efficiency being the main fields to be investigated. All different studies were able to point out how dual-fuel engines remain an interesting alternative for producing power, using gases of low energy content like biogas. Starting from this, the present work wants to clearly provide an extensive combustion comparison between biogas and methane (whose behavior in combustion processes has been

widely modeled and experimentally validated in recent years), in order to create a strong basis for further experimental research, by performing a deep simulation study which covers some of the most important topics in modern combustion (equilibrium composition, laminar premixed flames, and partially premixed flames). Since partially premixed flames (PPF) widely occur in diesel engines, they represent the most important issue to be covered in order to provide future researchers with fundamental information for further experimental investigations on diesel generators fed with biogas. This is the reason why the primary objective of this work is to set up the theoretical basis for predicting the behavior of simulated biogas when burning inside PPF generators.

As biogas can be used to produce mechanical energy through a chemical process like combustion, it can be also used to feed solid oxide fuel cells in order to electrochemically produce energy. In fact, due to their particular characteristics, SOFCs may offer multiple advantages when compared both to the traditional thermal machines and to the so-called PEMFCs (standing for proton exchange membrane fuel cells). The most important advantage is that SOFCs may be run with other fuels than hydrogen. For this reason, current research, which mainly aims to model both the chemical processes (heterogeneous reactions) occurring on the anode surface^{[7],[8]} and the electrochemical reactions due to charge transfer^[9], is strongly trying to model and experimentally analyze the behavior of hydrocarbon fuels like methane when directly feeding SOFCs^{[10],[11],[12]}. As a matter of fact, hydrocarbon fuels are capable to go through a process of internal reforming inside SOFCs and turn into a mixture of synthetic gas (or syngas), basically composed of hydrogen (which remains the main fuel for fuel cells) and carbon monoxide. In this sense, by considering biogas to be a simplified mixture of pure methane and carbon dioxide (representing all contaminants arising from anaerobic digestion), the objective of the present work is to experimentally investigate a tubular anode-supported SOFC and to build up and validate a numerical model (based on previous literature^{[10],[11]}) for predicting the final composition of the exhaust gases coming out of the fuel cell as well as the mole-fraction profiles

of main chemical species along the anode channel, when different operational conditions are applied to the cell. In particular, both dry- and steam-reforming processes are to be investigated, in order to create a useful and complete tool for further research.

CHAPTER 2

BIOGAS COMBUSTION EQUILIBRIUM

2.1 Introduction

The first part of the following study has been developed by using *CHEMKIN 4.1* and *CHEMKIN 10101*, which are different versions of the same software produced by *Reaction Design, Inc.* These two products only differ in some details (graphical tools, GUI, convergence of numerical methods, etc.) by maintaining the same solid and powerful computational structure.

2.1.1 CHEMKIN Overview

CHEMKIN, a software suite used worldwide in the microelectronics, combustion and chemical processing industries, is one of the most successful and enduring products to come out of *Sandia National Laboratories*. *CHEMKIN* is a set of flexible and powerful tools for incorporating complex chemical kinetics into simulations of reacting flow. The software is a collection of programs and subroutine libraries, which work together to facilitate the formation, solution and interpretation of problems involving gas-phase and heterogeneous (gas-surface) chemical kinetics. Using *CHEMKIN*, researchers are able to investigate thousands of reaction combinations to develop a comprehensive understanding of a particular process, which might involve multiple chemical species, concentration ranges and gas temperatures.

Since its origins nearly thirty years ago, *CHEMKIN* has made significant strides in the modelling of complex chemical processes, such as combustion. It has become the standard for anyone involved in chemistry modelling and chemically reacting flow modelling. It has also become an important educational tool in chemical engineering, mechanical engineering and chemistry curricula^[13].

2.1.2 GRI 3.0 Mechanism

In order to run *CHEMKIN* simulations, it is necessary for the user to choose a mechanism, which is basically the set of chemical species, chemical reactions, data and properties needed for a combustion calculation.

Since biogas can be considered as a mixture of methane and carbon dioxide with little amounts of multiple contaminants, the mechanism chosen for the current study is the well-known GRI 3.0^[14]. It is essentially a list of elementary chemical reactions and associated rate constant expressions, mostly used to study the methane-air combustion problem. In particular, GRI 3.0 includes 53 chemical species and 325 chemical reactions. Most of the reactions listed have been studied in the laboratory and so the rate constant parameters mostly have more or less direct measurements behind them.

Here is a brief description of how GRI 3.0 was built and developed. Once the Berkeley researchers had a starting set of rate constant parameters, they undertook extensive sensitivity tests on a variety of experimental data related to natural gas ignition and flames. These tests told them which rate parameters should be considered closely to “tune” the set so as to get an optimum representation of the data. Then they went through a long process of simultaneous parameter optimization, most of it done automatically, to get the parameter set for each successive release. This was carried out with strict constraints to keep the rate parameters being optimized within predetermined bounds that they set on the basis of evaluations of the uncertainties in measurements of the rates of elementary reactions and by applications of conventional reaction rate theory. Once an optimal parameter set was found, it was checked against the literature in an extensive “validation round”. In addition to reviewing the literature rate constant data they also examined the thermochemistry of the free radicals in the mechanism. Since some of the thermochemical parameters in GRI 3.0 differ from those in the Sandia data base, they provided a file of the complete GRI 3.0 thermochemistry, represented as the coefficients of NASA polynomials.

2.1.3 Biogas Composition

The GRI 3.0 mechanism comprises only five chemical elements, which are carbon, oxygen, hydrogen, nitrogen and argon and this introduces obvious restraints to a complete biogas study. In fact, biogas often contains small but non-negligible amounts of contaminants like hydrogen sulphide, siloxanes, ammonia, aromatic compounds and other substances than may be hazardous for human health. Thus it would be very important to examine the behavior of these substances during the combustion process for two reasons. The first one is of course represented by the issue about the possible affection of human breathing, while the second one concerns the performance (some of the substances cited above could form deposits capable to widely affect the carrying out of combustion).

Since most of the chemical elements contained in the contaminants are not included in the GRI 3.0 mechanism, two different biogas reference compositions were considered and the smaller contaminants were neglected. According to most of the available sources about biogas production, the most commonly produced types of biogas are the ones made by using either waste of agrifood industry or household waste^[15]. The reference compositions for both biogas types studied in the current study is summarized in Table I.

TABLE I. BIOGAS REFERENCE COMPOSITIONS EXPRESSED IN TERMS OF PERCENTAGE MOLE FRACTIONS.

Chemical Species	Biogas 1 Agrifood Industry	Biogas 2 Household Waste
CH ₄	68%	60%
CO ₂	26%	33%
H ₂ O	5%	6%
N ₂	1%	1%
O ₂	0%	0%

2.2 Combustion Equilibrium Study

A preliminary equilibrium study can be useful in order to understand some important issues about the combustion of a certain fuel. In particular, the main thermodynamic properties can be evaluated to determine the goodness of the combustion process and an analysis of combustion products can provide a general overview about fuel emissions.

In high-temperature combustion processes, the products of combustion are not a simple mixture of ideal products, as may be suggested by a simple atom-balance to determine stoichiometry. Rather, the major species dissociate, producing a host of minor species. Under some conditions, what ordinarily might be considered a minor species is actually present in quite large quantities. For instance, the ideal combustion products for burning a hydrocarbon with air are CO_2 , H_2O , O_2 , and N_2 . Dissociation of these species and reactions among the dissociation products yields the following species: H_2 , OH , CO , H , O , N , NO ; and possibly others.

The problems we mainly address in this chapter are the calculation of the adiabatic flame temperature and the computation of the mole fractions of all of the product species at a given pressure, subject to the constraint of conserving the number of moles of each of the elements present in the initial mixture. This element constraint merely says that the number of C, H, O, and N atoms is constant, regardless of how they are combined in the various species.

If a fuel-air mixture burns adiabatically at constant pressure, the absolute enthalpy of the reactants at the initial state (say, $T = 298 \text{ K}$, $P = 1 \text{ atm}$) equals the absolute enthalpy of the products at the final state ($T = T_{ad}$, $P = 1 \text{ atm}$). Thus:

$$H_{\text{reac}}(T_i, P) = H_{\text{prod}}(T_{ad}, P) , \quad (1)$$

or, equivalently, on a per-mass-of-mixture basis:

$$h_{\text{reac}}(T_i, P) = h_{\text{prod}}(T_{ad}, P) . \quad (2)$$

This first-law statement defines what is called the constant-pressure adiabatic flame temperature. Conceptually, the adiabatic flame temperature is simple since it can be defined as the maximum temperature that the combustion process can reach in the absence of heat exchange; however,

evaluating this quantity requires knowledge of the composition of the combustion products. At typical flame temperatures, the products dissociate and the mixture comprises many species. Flame temperatures are typically several thousand kelvins.

For what concerns the computation of the product mole fractions, it is well-known that there are several ways to approach the calculation of equilibrium composition. Generally, it is preferred to focus on the equilibrium-constant approach and limit the discussion to the application of ideal gases^[16].

2.3 Determining Chemical Equilibria with CHEMKIN^[17]

In addition to chemically reacting flow applications, *CHEMKIN* includes an Equilibrium Reactor model. This model allows the user to determine the chemical state of a mixture under equilibrium conditions. Any number of gas-phase or condensed (bulk) species can be included in an equilibrium calculation, while surface site species are ignored. In this way, the Equilibrium Reactor model can be used to determine phase equilibrium, between gas and condensed phases, as well as chemical equilibrium. All that is required is thermodynamic data for all species in each phase.

An established method for evaluating chemical equilibrium is the element-potential method embodied in the Stanford software STANJAN^[18]. The *CHEMKIN* Equilibrium Reactor employs the STANJAN library of routines in its solution method. The equilibrium determines composition equilibrium and/or phase equilibrium. The results depend only on the thermodynamic properties of the species in the user's chemistry set, as well as the starting composition and conditions specified. The starting composition determines the relative amount of chemical elements in the system. An initial estimate of the equilibrium temperature can sometimes be used to select a "burned" equilibrium state from an "unburned" equilibrium state in the case where two equilibrium states are possible.

Currently, the equilibrium program assumes that the gas-phase is a mixture of ideal gases and that condensed phases are ideal solutions. The user selects atomic populations through identity of initial species and their fraction in each phase, as well as the state parameters. The user may specify the state parameters in a number of different ways, including:

- temperature and pressure;
- pressure and entropy;
- enthalpy and pressure;
- volume and entropy.

Species composition can be “frozen” in a given calculation, or the equilibrium composition can be determined. Calculations may be linked through continuations, such that the conditions calculated from a previous equilibrium case can be used as the starting point for a subsequent case with different constraints. In this way, the user can employ the Equilibrium Reactor Model to analyze stages in a thermodynamic cycle.

The Equilibrium Reactor Model is also commonly used to determine adiabatic flame temperatures for combustible gas mixtures. Such a simulation is performed by specifying an initial gas mixture and constraining equilibrium for constant enthalpy and constant pressure. The calculation can also be performed using constant internal energy and constant volume. An initial guess for the equilibrium temperature of about 1000 K or above is usually needed to cause the equilibrium solver to find the burned-gas solution. For accurate adiabatic-flame-temperature calculations, it is important to include all radical species that might occur in the flame, as well as stable reactants and products.

The following paragraph describes the equations solved and the methodology used for determining chemical and phase equilibria of arbitrary systems.

2.3.1 Minimization of Gibb’s Free Energy

The basic theory for the element-potential method of determining equilibrium is based on the minimization of Gibb’s free energy. The Gibb’s function of a system is:

$$G = \sum_{k=1}^K \bar{g}_k N_k , \quad (3)$$

where \bar{g}_k is the partial molar Gibb's function N_k and is the number of moles of each species k in the system. K is the total number of species.

For ideal-gas mixtures or ideal solutions, the partial molar Gibb's functions are given by:

$$\bar{g}_k = g_k(T, P) + RT \ln X_k , \quad (4)$$

where $g_k(T, P)$ is the Gibb's function for the pure species k , evaluated at the system temperature and pressure; R is the universal gas constant and X_k is the mole fraction of the k th species.

The equilibrium solution at a given temperature and pressure is the distribution of N_k that minimizes the system Gibb's function, G , subject to atomic population constraints (and non-negative N_k). The atomic population constraints are:

$$\sum_{k=1}^K n_{jk} N_k = p_j \quad j = 1, \dots, M , \quad (5)$$

where n_{jk} is the number of the j th atoms that appear in the k th molecule, p_j is the total population in moles of the j th atom in the system, and M is the total number of different elements that are present in the system.

Details regarding the relationship between the partial molar Gibb's functions and the elemental potentials for the atoms, as well as the explicit form of the equations solved in the STANJAN library, are described in the STANJAN report^{[18], p.99}.

2.4 How to Perform an Equilibrium Calculation with CHEMKIN

An important point about *CHEMKIN* is represented by the fact that the software has its own interface and this is what makes *CHEMKIN* a user friendly tool. In particular, when opening *CHEMKIN*, the user can decide whether to start their study from taking a sample file (*CHEMKIN*

library widely covers a lot of different chemical issues) or to create a new file so that everything can be set according to their own needs. The first window that the user has to deal with is the Pre-Processing one, where the user is required to set the working directory and the chemistry set. A new chemistry set can be created if working with a new project, otherwise the chosen set can be edited by changing the Gas-Phase Kinetics File (this is the only input file required to perform an equilibrium calculation; a thermodynamics data file can be also entered but it cannot influence the simulation anyhow). As said before, the Gas-Phase Kinetics File used to study biogas combustion processes is the one from GRI 3.0 mechanism. After setting all fields in the pre-processing window, the user has to open the Cluster window to define reactor physical properties, reactant species, and possible constrained species. For what concerns the reactor physical properties, the user is required to define the type of problem (for instance, choose *Constant Pressure Enthalpy* to get pressure fixed), initial temperature, pressure, as well as the estimated equilibrium temperature (it is not explicitly required but sometimes it can help to quicken the computation). After that, the user can define the reactant species by expressing them on a mole-fraction or mass-fraction base and by specifying the equivalence ratio. In particular, mole fractions of the fuel-mixture species, mole fractions of the oxidizer-mixture species, and complete combustion products must be entered. Constrained species can be also specified in the same way if any. The last option in the Cluster section concerns the possibility for the user to set a certain number of continuations, which are subsequent calculation sessions that let the user change a parameter group as well as the type of problem or a single parameter without running multiple simulations. When everything is set in the Cluster window, a simulation can be run by creating an input file first. When the simulation is done (it generally takes a few seconds), the user can examine all quantities of interest since they are collected in a simple output file. Furthermore, a post-processor can be run so that the user can make plots, see the data or export them to an Excel sheet, and exploit all *CHEMKIN* utilities and tools.

2.5 Simulation Results

Table II presents a general summary about the equilibrium-composition mole fractions of all chemical species involved in the mechanism. Equivalence ratio is set to unity ($\phi = 1$), while initial temperature is 298 K and pressure is 1 atm. Mole-fraction values of starred species represent the mole fractions of complete-combustion products: water vapour content practically does not vary for all fuels (although the initial content is different for both biogases), while, the more the fuel contains carbon dioxide in its initial composition, the more carbon-dioxide production is increased (we should not talk about “production” since it is very difficult to state how much carbon dioxide is really produced or consumed during the combustion process, but, since we are examining an initial and a final state, we can refer to the latter state as the condition in which every chemical species has been produced or consumed). Nitrogen content is the same for both biogas types in the initial composition, thus it is easy to state that its different final content in the products has to deal with other chemical species containing nitrogen (in particular, it is well-known how nitrogen oxides play a fundamental role).

Table III shows a preliminary comparison between methane and both biogas types chosen by considering the emissions of main pollutants like carbon and nitrogen oxides reported in Table II. Conditions are the same as above. Both biogas types guarantee a considerable reduction of nitrogen-oxides emissions and a strong decrease of carbon-monoxide production. What increases is the content of carbon dioxide (more than 50% for biogas 2), which is, however, contained in both fuels. Hence it is easy to state that, from a preliminary emission study based on the equilibrium composition, biogas seems to present lower emissions than methane in combustion processes, considering that carbon dioxide contained in the fuel can have a strong effect on final products. In fact, carbon dioxide can be considered to be the main contaminant for biogas and its final content can be considerably large even if its production rate remains low.

TABLE II. EQUILIBRIUM-COMPOSITION MOLE FRACTIONS OF ALL CHEMICAL SPECIES INVOLVED IN THE COMBUSTION PROCESS FOR ALL CONSIDERED FUELS ($\phi = 1, T_{in} = 298 \text{ K}, P = 1 \text{ atm}$).

Chemical species	Methane	Biogas 1	Biogas 2
N ₂ *	0.70879	0.68115	0.66989
H ₂ O*	0.18351	0.18417	0.18390
CO ₂ *	0.08549	0.11752	0.13095
CO	0.00884	0.00751	0.00688
H ₂	0.00355	0.00232	0.00195
H	0.00038	0.00019	0.00014
O ₂	0.00455	0.00374	0.00341
O	0.00021	0.00011	0.00008
OH	0.00282	0.00192	0.00162
NO	0.00186	0.00136	0.00119
NO ₂	$3.40 \cdot 10^{-7}$	$2.54 \cdot 10^{-7}$	$2.22 \cdot 10^{-7}$
CH ₄	$2.90 \cdot 10^{-17}$	$1.08 \cdot 10^{-17}$	$7.12 \cdot 10^{-18}$
HO ₂	$4.87 \cdot 10^{-7}$	$3.18 \cdot 10^{-7}$	$2.63 \cdot 10^{-7}$
H ₂ O ₂	$4.49 \cdot 10^{-8}$	$3.24 \cdot 10^{-8}$	$2.80 \cdot 10^{-8}$
HCO	$7.64 \cdot 10^{-10}$	$3.82 \cdot 10^{-10}$	$2.81 \cdot 10^{-10}$
CH ₂ O	$1.28 \cdot 10^{-11}$	$7.11 \cdot 10^{-12}$	$5.48 \cdot 10^{-12}$
N	$1.36 \cdot 10^{-8}$	$4.88 \cdot 10^{-9}$	$3.18 \cdot 10^{-9}$
NH	$2.26 \cdot 10^{-9}$	$8.50 \cdot 10^{-10}$	$5.65 \cdot 10^{-10}$
NH ₂	$9.10 \cdot 10^{-10}$	$3.94 \cdot 10^{-10}$	$2.78 \cdot 10^{-10}$
NH ₃	$2.64 \cdot 10^{-9}$	$1.53 \cdot 10^{-9}$	$1.22 \cdot 10^{-9}$
NNH	$7.32 \cdot 10^{-10}$	$3.38 \cdot 10^{-10}$	$2.45 \cdot 10^{-10}$
N ₂ O	$9.85 \cdot 10^{-8}$	$7.11 \cdot 10^{-8}$	$6.17 \cdot 10^{-8}$
HNO	$3.28 \cdot 10^{-8}$	$1.88 \cdot 10^{-8}$	$1.49 \cdot 10^{-8}$
HCN	$1.85 \cdot 10^{-11}$	$8.21 \cdot 10^{-12}$	$5.78 \cdot 10^{-12}$
HOCN	$1.09 \cdot 10^{-12}$	0	0
HNCO	$3.77 \cdot 10^{-10}$	$2.54 \cdot 10^{-10}$	$2.12 \cdot 10^{-10}$
NCO	$1.48 \cdot 10^{-11}$	$7.27 \cdot 10^{-12}$	$5.30 \cdot 10^{-12}$

TABLE III. MAIN-POLLUTANT-EMISSIONS COMPARISON BETWEEN METHANE AND BIOGAS 1 AND 2 ($\phi = 1, T_{in} = 298 \text{ K}, P = 1 \text{ atm}$).

Chemical species	Biogas 1 Agrifood industry	Biogas 2 Household waste
CO	-15.1%	-22.2%
CO ₂	+37.5%	+53.2%
NO	-26.6%	-35.9%
NO ₂	-25.2%	-34.6%

2.5.1 Effect of Main Contaminants on Adiabatic Flame Temperature

Figure 1 shows how adiabatic flame temperature can vary with respect to the molar concentration of main biogas contaminants. Combustion process is considered to start from a temperature of 500 K (the higher is the initial temperature, the more the influence of different contaminants will be emphasized), equivalence ratio is set to unity, and pressure is 1 atm. Contaminants are taken one by one, by considering the fuel as a mixture of only methane and the contaminant itself. Then the contaminant concentration is supposed to vary by consequently reducing the content of methane. On one hand, from Figure 1a we can easily deduce that carbon dioxide can largely reduce adiabatic flame temperature, which can be brought down by up to 25°C for biogas containing 30% of carbon dioxide in its initial composition. On the other hand, Figure 1b presents a general summary of the effect of smaller contaminants. In particular, nitrogen and water vapour are always present in small quantities and do not almost affect adiabatic flame temperature, with water vapour having more effect than nitrogen (considering the composition of current types of biogas, 1°C drop is the maximum effect for nitrogen, while water vapour contained in biogas 2 can reduce adiabatic flame temperature up to 7°C). Oxygen can be present in relatively small quantity and can increase adiabatic flame temperature by helping the oxidation process (2% of molecular oxygen in the fuel will increase the temperature by 7°C).

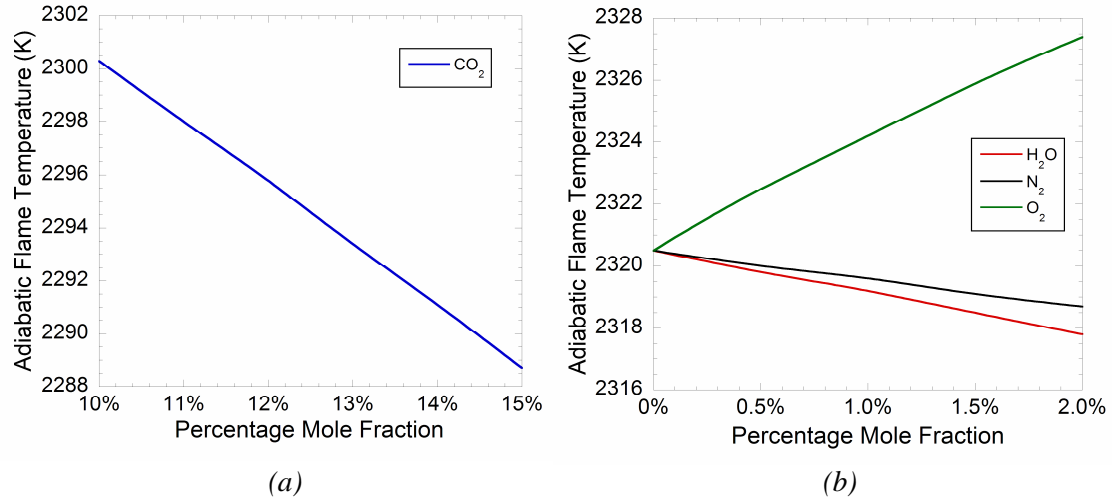


Figure 1. Effect of contaminants on adiabatic flame temperature ($\phi = 1, T_{in} = 500$ K, $P = 1$ atm).

2.5.2 Influence of Equivalence Ratio on Adiabatic Flame Temperature

Figure 2 shows how adiabatic flame temperature varies with respect to the equivalence ratio of the air-fuel mixture. Combustion process is considered to start from a temperature of 500 K, while pressure keeps constant and is set to 1 atm. By analyzing the trend of the three different curves, which is practically the same for all fuels, it is easy to understand that biogas behaves like methane: adiabatic flame temperature increases for equivalence ratios lower than 1, while it decreases for values which are higher than 1.1, with the slope of the descending branch being higher than the growing one; maximum temperature for all fuels is for equivalence ratios contained in the range 1-1.1, with values tending to 1 for biogas and to 1.1 for methane. Biogas curves are offset with respect to the methane curve: generally, the more biogas contains methane, the closer its curve will be to the methane curve, i.e., biogas from agrifood industry is allowed to reach higher adiabatic flame temperatures than biogas produced from household waste. This means that, for biogas, adiabatic flame temperature is somehow proportional to the methane content in the fuel.

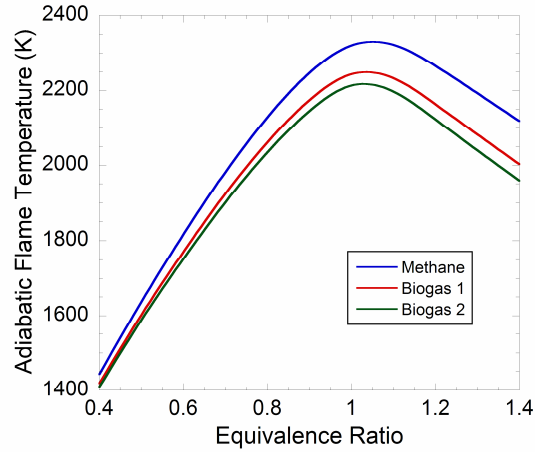


Figure 2. Effect of equivalence ratio on adiabatic flame temperature ($\phi = 1$, $T_{in} = 500$ K, $P = 1$ atm).

2.5.3 Influence of Equivalence Ratio on Pollutant Emissions

For what concerns emissions for varying equivalence ratios, it is well-known that the emissions of carbonaceous pollutants reasonably increase for richer mixtures and, since applied combustion literature is full of examples^[16], they will not be further examined in this chapter. In this sense, only Figure 3 is reported to show how carbon-monoxide production rapidly increases for richer air-fuel mixtures, with the two biogas curves practically coinciding.

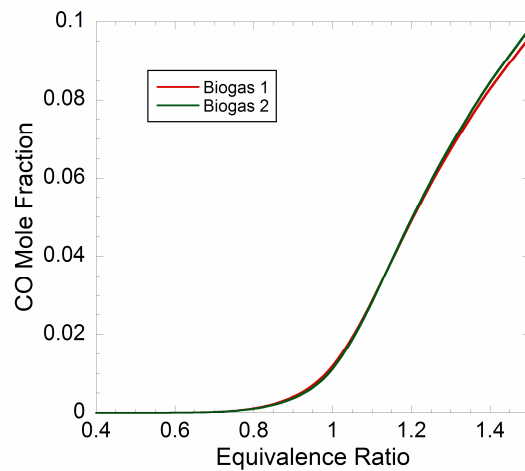


Figure 3. Influence of equivalence ratio on carbon-monoxide emissions ($\phi = 1, T_{in} = 500$ K, $P = 1$ atm).

CHAPTER 3

BIOGAS LAMINAR PREMIXED FLAMES

3.1 Introduction

Laminar premixed flames have application in many residential, commercial, and industrial devices and processes. Examples include gas ranges and ovens, heating appliances, and Bunsen burners. Laminar premixed flames are by themselves important; but, perhaps more importantly, understanding laminar flames is a necessary prerequisite to the study of turbulent flames. In both laminar and turbulent flows, the same physical processes are active, and many turbulent flame theories are based on an underlying laminar flame structure. In this chapter, we will focus on the essential characteristics of laminar premixed flames in order to see what factors influence the laminar flame speed and the flame thickness, which are the main parameters in understanding flame structure. It will be easy to see how equivalence ratio, temperature, pressure, and fuel type affect these fundamental quantities. Flame speed is emphasized because it is the property that dictates flame shape and important flame-stability characteristics^[16].

3.2 Physical Description

A flame is a self-sustaining propagation of a localized combustion zone at subsonic velocities. This definition clearly contains several key words. First, a flame must be localized; that is, a flame occupies a small portion of the combustible mixture at any one time. Secondly, a flame must be subsonic. A discrete combustion wave that travels subsonically is termed a deflagration. It is also possible for combustion waves to propagate at supersonic velocities, and such a wave is called a detonation. The fundamental propagation mechanisms are different in deflagrations and detonations, and, because of this, these are distinct phenomena.

A flame may be freely propagating, as occurs when a flame is initiated in a tube containing a combustible gas mixture. The appropriate coordinate system would be fixed to the propagation

combustion wave. An observer riding with the flame would experience the unburned mixture approaching at the flame speed, S_L . This is equivalent to a flat flame stabilized on a burner. Here, the flame is stationary to the laboratory reference frame, and, once again, the reactants enter the flame with a velocity equal to the flame propagation velocity, S_L . In both examples, we assume that the flame is one dimensional and that the unburned gas enters the flame in a direction normal to the flame sheet. Since a flame heats the products, the product density is less than the reactant density. Continuity thus requires the burned gas to be greater than the velocity of the unburned gas:

$$\rho_u S_L A \equiv \rho_u v_u A = \rho_b v_b A , \quad (6)$$

where the subscripts u and b refer to the unburned and burned gases, respectively. For a typical hydrocarbon-air flame at atmospheric pressure, the density ratio is approximately seven. Thus, there is a considerable acceleration of the gas flow across the flame.

Generally, it is convenient to divide a flame into two zones: the preheat zone, where little heat is released, and the reaction zone, where the bulk of the chemical energy is released. At atmospheric pressure, the flame thickness is quite thin, of the order of a millimeter. It is useful to divide the reaction zone further into a thin region of very fast chemistry followed by a much wider region of slow chemistry. The destruction of the fuel molecules and the creation of many intermediate species occur in the fast-chemistry region. This region is dominated by bimolecular reactions. At atmospheric pressure, the fast-reaction zone is quite thin, typically less than a millimeter. Because this zone is thin, temperature gradients and species concentration gradients are very large. These gradients provide the driving forces that cause the flame to be self-sustaining, i.e., the diffusion of heat and radical species from the reaction zone to the preheat zone. In the secondary reaction zone, the chemistry is dominated by three-body radical recombination reactions, which are much slower than typical bimolecular reactions, and the final burnout of CO via $CO + OH \rightarrow CO_2 + H$. This secondary reaction zone may extend several millimeters in a 1-atm flame. Additional information may be found in Fristrom^[19].

Hydrocarbon flames are also characterized by their visible radiation. Within an excess of air, the fast-reaction zone appears blue. This blue radiation results from excited CH radicals in the high-temperature zone. When the air is decreased to less than stoichiometric proportions, the zone appears blue-green, now as a result of radiation from excited C₂. In both flames, OH radicals also contribute to the visible radiation, and to a lesser degree, chemiluminescence from the reaction $CO + O \rightarrow CO_2 + hv$. If the flame is made richer still, soot will form, with its consequent blackbody continuum radiation. Although the soot radiation has its maximum intensity in the infrared, the spectral sensitivity of the human eye causes us to see a bright yellow (nearly white) to dull orange emission, depending on the flame temperature^[16].

3.3 Analyzing 1-D Laminar Premixed Flames with CHEMKIN^[17]

CHEMKIN includes two different Reactor Models for studying laminar-premixed-flame phenomena. They are the following:

- Premixed Laminar Burner-stabilized Flame;
- Premixed Laminar Flame-speed calculation.

These Premixed Flame Models solve the set of governing differential equations that describe the flame dynamics using implicit finite difference methods, as well as a combination of time-dependent and steady-state methods. The solver algorithm employed automates coarse-to-fine grid refinement as a means to enhance the convergence properties of the steady-state approach and as a means to provide optimal mesh placement.

The Burner-stabilized Flame Model is the one most often used for analyzing species profiles in flame experiments, where the mass flow rate through the burner is known, while the Flame-speed Calculation Model (the one on which this work is focused) involves a freely propagating flame. The latter configuration is used to determine the characteristic flame speed of the gas mixture at specified pressure and inlet temperature. In this case there are no heat losses (by definition) and thus the temperatures should be computed from the energy equation. Flame

speed depends, in part, on the transport of heat, and predicting the temperature distribution is an integral part of the flame speed calculation.

3.3.1 1-D Flame Equations

For the following equations, we assume one-dimensional flow with uniform inlet conditions. The governing conservation equations reduce to:

- *Continuity:*

$$\dot{M} = \rho u A , \quad (7)$$

- *Energy conservation:*

$$\dot{M} \frac{dT}{dx} - \frac{1}{c_p} \frac{d}{dx} \left(\lambda A \frac{dT}{dx} \right) + \frac{A}{c_p} \sum_{k=1}^K \dot{\omega}_k h_k W_k = 0 , \quad (8)$$

- *Species conservation:*

$$\dot{M} \frac{dY_k}{dx} + \frac{d}{dx} (\rho A Y_k V_k) - A \dot{\omega}_k W_k = 0 \quad k = 1, \dots, K_g , \quad (9)$$

- *Equation of state:*

$$\rho = \frac{P \bar{W}}{RT} . \quad (10)$$

In these equations x denotes the spatial coordinate, \dot{M} the mass flow rate (which is independent of x), T the temperature, Y_k the mass fraction of the k th species (there are K_g gas species), P the pressure, u the velocity of the fluid mixture, ρ the mass density, W_k the molecular weight of the k th species, \bar{W} the mean molecular weight of the mixture, R the universal gas constant, λ the thermal conductivity of the mixture, c_p the constant-pressure heat capacity of the mixture, c_{pk} the constant pressure heat capacity of the k th species, $\dot{\omega}_k$ the molar rate of production by chemical reaction of the k th species per unit volume, h_k the specific enthalpy of the k th species, V_k the diffusion velocity of the k th species, and A the cross-sectional area of the stream tube encompassing the flame (normally increasing due to thermal expansion) normalized by the burner

area. The user may provide an area profile (APRO) or alternatively a subroutine to specify the area as a function of the spatial coordinate. By default, the stream tube area is taken to be constant and equal to unity.

The net chemical production rate $\dot{\omega}_k$ of each species results from a competition between all the chemical reactions involving that species. We presume that each reaction proceeds according to the law of mass action and the forward rate coefficients are in the modified Arrhenius form:

$$k_f = AT^\beta e^{-\frac{E_a}{RT}}. \quad (11)$$

This expression will be discussed in the second part of this study, since it represents a fundamental point for studying chemical reactions occurring inside solid-oxide fuel cells.

In addition to chemical reaction rates, we must also be concerned with the transport properties of the species, i.e., thermal conductivities and diffusion coefficients. Stockmayer potentials are used throughout in evaluating transport properties. The user has the option of evaluating transport properties using mixture-averaged formulas or a multicomponent diffusion model. A brief description about the first option is provided here, since it is the one used throughout the calculation made.

3.3.2 Mixture-Averaged Transport Properties

For the mixture-averaged formula, we assume the diffusion velocity V_k to be composed of three parts:

$$V_k = v_k + w_k + V_c, \quad (12)$$

where v_k is the ordinary diffusion velocity and is given in the Curtiss-Hirschfelder^[20], p.80 approximation by:

$$v_k = D_{km} \frac{1}{X_k} \frac{dX_k}{dx}, \quad (13)$$

where X_k is the mole fraction, and where the mixture-averaged diffusion coefficient D_{km} is given explicitly in terms of the binary diffusion coefficients D_{kj} :

$$D_{km} = \frac{1 - Y_k}{\sum_{j \neq k}^K \frac{X_j}{D_{kj}}} . \quad (14)$$

A non-zero thermal diffusion velocity is included only for the low molecular weight species H , H_2 , and He . The trace, light-component limit is employed in determining w_k , i.e.:

$$w_k = \frac{D_{km} \Theta_k}{X_k} \frac{1}{T} \frac{dT}{dx} , \quad (15)$$

where Θ_k is the thermal diffusion ratio^{[21], p.92}. The sign of Θ_k makes the lower molecular weight species diffuse from low to high temperature regions.

The correction velocity V_c (independent of species but a function of the distance) is included to insure that the mass fractions sum to unity or equivalently:

$$\sum_{k=1}^K Y_k V_k = 0 . \quad (16)$$

The formulation of the correction velocity is the one recommended by Coffee and Heimerl^{[22], p.72,}
80 in their extensive investigation of approximate transport models in hydrogen and methane flames.

3.3.3 Finite Difference Approximations

The first task in solving the flame problem is to discretize the governing conservation equations. We use finite difference approximations on a non-uniform grid with points numbered from 1 at the cold boundary to J at the hot boundary. On the convective terms the user has the choice of using either first order windward differences or central differences. Both cases are illustrated using the convective term in the energy equation. The windward difference is given as:

$$\left(\dot{M} \frac{dT}{dx} \right)_j \approx \dot{M}_j \left(\frac{T_j - T_{j-1}}{x_j - x_{j-1}} \right) , \quad (17)$$

where the index j refers to the mesh point. The central difference formula is:

$$\left(\dot{M} \frac{dT}{dx} \right)_j \approx \dot{M}_j \left(\frac{h_{j-1}}{h_j(h_j + h_{j-1})} T_{j+1} + \frac{h_j - h_{j-1}}{h_j h_{j-1}} T_j - \frac{h_j}{h_{j-1}(h_j + h_{j-1})} T_{j-1} \right), \quad (18)$$

where $h_j = x_{j+1} - x_j$. The windward difference formula introduces artificial diffusion on a coarse mesh; this has the effect of spreading out the solution and making the convergence of Newton's method less sensitive to the starting estimate. However, because the mesh is refined in regions of high gradient, the artificial diffusion becomes relatively unimportant after the solution has progressed to the fine meshes. Nevertheless, for a given mesh, the windward difference approximation is less accurate than the central difference formula. Therefore, the user may want to select the central difference formula on finer meshes or in cases where the solution is converging without difficulty.

The first derivative in the summation term in the energy equation is always approximated by a central difference formula:

$$\left(\frac{dT}{dx} \right)_j \approx \dot{M}_j \left(\frac{h_{j-1}}{h_j(h_j + h_{j-1})} T_{j+1} + \frac{h_j - h_{j-1}}{h_j h_{j-1}} T_j - \frac{h_j}{h_{j-1}(h_j + h_{j-1})} T_{j-1} \right), \quad (19)$$

and the coefficients in the summation are evaluated at j .

The second derivative term in the energy equation is approximated by the following second order central difference:

$$\frac{d}{dx} \left(\lambda A \frac{dT}{dx} \right)_j \approx \left(\frac{2}{x_{j+1} - x_{j-1}} \right) \left[(\lambda A)_{j+\frac{1}{2}} \left(\frac{T_{j+1} - T_j}{x_{j+1} - x_j} \right) + \left(-(\lambda A)_{j+\frac{1}{2}} \right) \left(\frac{T_j - T_{j-1}}{x_j - x_{j-1}} \right) \right]. \quad (20)$$

The coefficients in this formula (at $j \pm 1/2$) are evaluated using the averages of the dependent variables between mesh points.

The diffusive term in the species conservation equation is approximated in a similar way, but it appears to be different because we have written it using diffusion velocities. The ordinary

equation (13) and thermal equation (15) diffusion velocities are approximated at the $j \pm 1/2$ positions as illustrated by the following mixture-averaged evaluation:

$$(Y_k v_k)_{j+\frac{1}{2}} \approx - \left(\frac{W_k D_{km}}{\bar{W}} \right)_{j+\frac{1}{2}} \left(\frac{X_{k,j+1} - X_{k,j}}{x_{j+1} - x_j} \right), \quad (21)$$

and:

$$(Y_k w_k)_{j+\frac{1}{2}} \approx - \left(\frac{W_k D_{km} \Theta_k}{\bar{W} T} \right)_{j+\frac{1}{2}} \left(\frac{T_{j+1} - T_j}{x_{j+1} - x_j} \right). \quad (22)$$

Since the mole fraction of a species can be zero, we avoid difficulties by forming $Y_k V_k$, rather than V_k itself ($Y_k = X_k W_k / \bar{W}$). After the diffusion velocities are computed at all the mesh midpoints, the correction velocity V_c is computed at the midpoints from:

$$V_c = \sum_{k=1}^K (v_k + w_k). \quad (23)$$

Upon forming the full diffusion velocities $V_k = v_k + w_k + V_c$ the diffusion term is evaluated with the following difference approximation:

$$\frac{d}{dx} (\rho A Y_k V_k)_j \approx \frac{(\rho A Y_k V_k)_{j+\frac{1}{2}} - (\rho A Y_k V_k)_{j-\frac{1}{2}}}{x_{j+\frac{1}{2}} - x_{j-\frac{1}{2}}}. \quad (24)$$

All the non-differentiated terms, such as the chemical production rate terms, are evaluated at the mesh points j . Coefficients not appearing within derivatives are also evaluated at the mesh points.

3.3.4 Boundary Conditions

Two different types of flame are considered: burner-stabilized flames and adiabatic, freely propagating flames. The conservation equations governing the two are the same, but the boundary conditions differ. In both cases the appropriate boundary conditions may be deduced from the early work of Curtiss and Hirschfelder^{[20], p.80}.

For freely propagating flames \dot{M} is an eigenvalue and must be determined as part of the solution. Therefore, an additional constraint is required, or alternatively one degree of freedom must be removed from the problem. We choose to fix the location of the flame by specifying and fixing the temperature at one point. This is sufficient to allow for the solution of the flame speed eigenvalue \dot{M} . The user must select this point in such a way as to insure that the temperature and species gradients “nearly” vanish at the cold boundary. If this condition is not met then the resultant will be too low because some heat will be lost through the cold boundary.

The boundary conditions are relatively easily implemented. At the cold boundary we specify the mass flux fractions and the temperature, i.e. we solve:

$$\mathcal{E}_{k,1} - Y_{k,1} - \left(\frac{\rho A Y_k V_k}{\dot{M}} \right)_{j=\frac{11}{2}} = 0, \quad (25)$$

and:

$$T_1 - T_b = 0, \quad (26)$$

where $\mathcal{E}_{k,1}$ is the inlet reactant fraction of the k th species and T_b is the specified burner temperature. At the hot boundary we specify that all gradients vanish, i.e.:

$$\frac{Y_{k,J} - Y_{k,J-1}}{x_J - x_{J-1}} = 0, \quad (27)$$

and:

$$\frac{T_J - T_{J-1}}{x_J - x_{J-1}} = 0. \quad (28)$$

3.3.5 Transient Forms of the Equations

Although the Premixed Flame models are solved as steady-state problems, the steady-state solution algorithm sometimes requires pseudo time-stepping to condition the solution iterate. For this reason, we extend the discussion of the governing equations presented before to include the transient terms used in time-stepping procedures. The transient equations are obtained by adding the time derivatives to equation (8) and equation (9), obtaining:

$$\rho A \frac{\partial T}{\partial t} + \dot{M} \frac{\partial T}{\partial x} - \frac{1}{c_p} \frac{\partial}{\partial x} \left(\lambda A \frac{\partial T}{\partial x} \right) + \frac{A}{c_p} \sum_{k=1}^K \rho Y_k V_k c_{pk} \frac{\partial T}{\partial x} + \frac{A}{c_p} \sum_{k=1}^K \dot{\omega}_k h_k W_k = 0, \quad (29)$$

and:

$$\rho A \frac{\partial Y_k}{\partial t} + \dot{M} \frac{\partial Y_k}{\partial x} + \frac{\partial}{\partial x} (\rho A Y_k V_k) - A \dot{\omega}_k W_k = 0 \quad k = 1, \dots, K. \quad (30)$$

The full system now becomes a system of parabolic partial differential equations, rather than an ordinary differential equation boundary value system. Solution is obtained via the backward-Euler method. In this method, the time derivatives are approximated by finite differences as illustrated by:

$$\rho A \frac{\partial T}{\partial t} \approx \rho_j^{n+1} A_j \left(\frac{T_j^{n+1} - T_j^n}{h} \right), \quad (31)$$

where the superscript n indicates the time level and h represents the size of the time step. All other terms are approximated with finite differences as before, but at time level $n+1$. Since all variables are known at time level n , the discretized problem is just a system of nonlinear algebraic equations for the dependent variable vector ϕ at time level $n+1$.

3.4 How to Perform a Flame-Speed Calculation with CHEMKIN

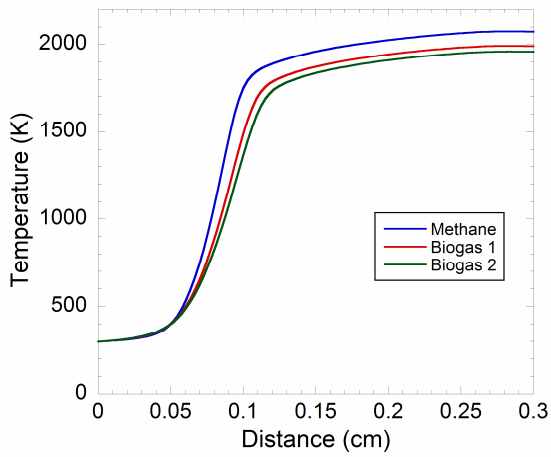
When performing a flame-speed calculation, the user has to face a more complex problem setup than the equilibrium one. First of all, the user has to choose again whether to use a *CHEMKIN* sample or to create a new chemistry set if working with a new project. If the first option is chosen, after setting the working directory, three different files have to be entered: the Gas-Phase Kinetics File, the Thermodynamics Data File, and the Gas Transport Data File (all of them are taken from GRI 3.0 mechanism). After that, the user has to open the Cluster window and hence to define reactor physical properties (in particular, temperature profile, pressure, and fixed temperature to constrain flame position must be set; the user has also to decide to use Mixture-averaged Transport Model or Multicomponent Model and to check the *Use Correction Velocity*

Formalism cell), initial grid properties (mainly containing the data regarding grid points and axial position), and species-specific properties (if any). Then stream properties and species-specific properties must be specified in the Inlet window: the user has to set the mass flow rate or the inlet velocity and to define the reactant species by expressing them on a mole-fraction or mass-fraction base and by specifying the equivalence ratio. In particular, mole fractions of the fuel-mixture species, mole fractions of the oxidizer-mixture species, and complete combustion products must be entered. Added species can be also specified in the same way if any. Remaining parameters to be set in order to run a simulation are the Solver data (concerning tolerances, time-stepping, and finite difference methods) and the Output Control data (where Print Level Control is the only necessary parameter to be set). The last option in the Cluster section concerns again the possibility for the user to set a certain number of continuations. When everything is set in the latter window, a simulation can be run by creating an input file first. When the simulation is done, the user can examine all quantities of interest by opening the output file and post-processor can be run.

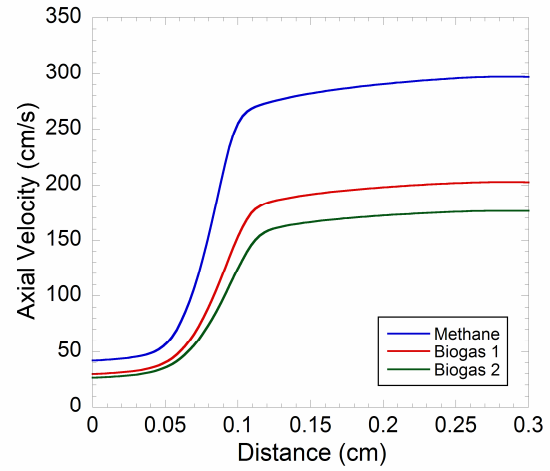
3.5 Simulation Results

We can now use the previously described analysis to obtain an understanding of the detailed structure of a premixed flame for all considered fuels. Figure 4 shows the temperature, the axial-velocity, and the heat generation distributions, and selected species mole-fraction profiles through 1-atm, stoichiometric, methane-air and biogas-air flames, simulated using *CHEMKIN* with GRI 3.0 mechanism. Initial temperature is 298 K, while axial distance is set to 3 mm. Figure 4c, 4d, and 4e show the main carbon-containing species (methane, carbon monoxide and carbon dioxide). Here it is easy to see the consumption of the fuel, the appearance of carbon monoxide, which is an intermediate species, and burn-out of carbon monoxide in order to form carbon dioxide. Carbon-monoxide concentration has its peak at approximately the same location where the methane concentration goes to zero, while the carbon dioxide concentration at first lags

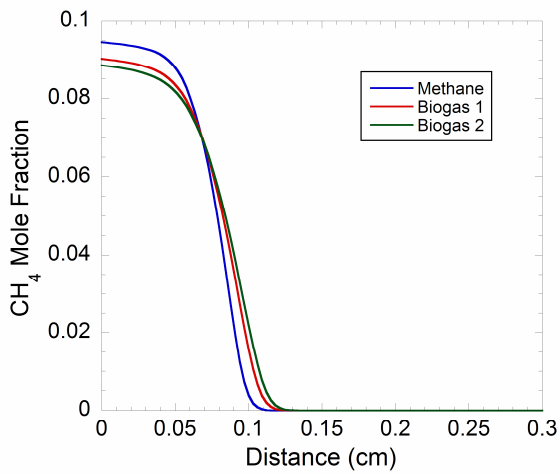
the carbon-monoxide one but then rises as the carbon monoxide is oxidized. This would be even clearer if a local-molar-production/destruction-rate analysis was made for the selected species^[16]. The bulk of the chemical activity is contained in an interval extending from about 0.5 mm to 1.5 mm. Figure 4f, 4g, and 4h show, similarly, that the carbon-containing intermediate species, CH₃, CH₂O, and HCO, are produced and destroyed in a narrow interval (0.4-1.1 mm), as is the CH radical (Figure 4i). The hydrogen-intermediates, HO₂ and H₂O₂ (Figure 4j and 4k), have somewhat broader profiles than the carbon-intermediates, and their peak concentrations appear slightly earlier in the flame. Also, water vapour reaches the major portion of its equilibrium much sooner than does carbon dioxide, i.e., approximately 0.9 mm versus 2 mm.



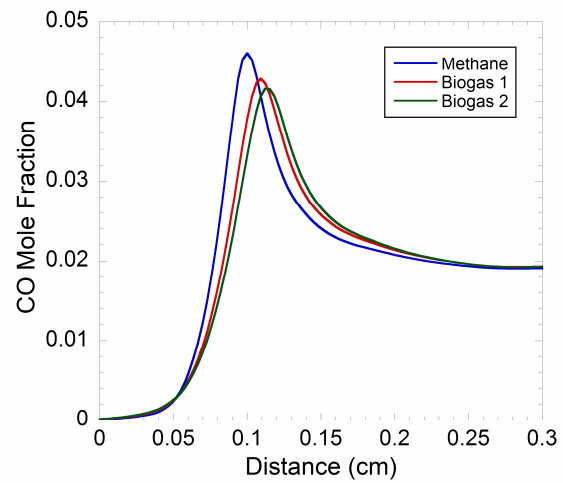
(a)



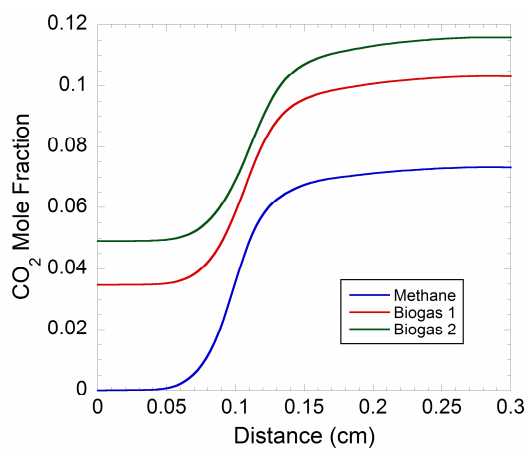
(b)



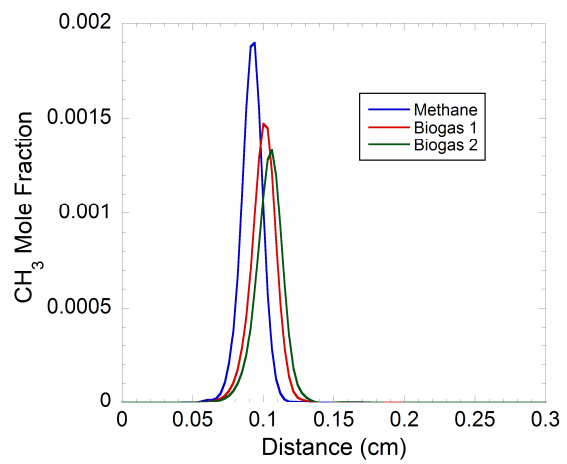
(c)



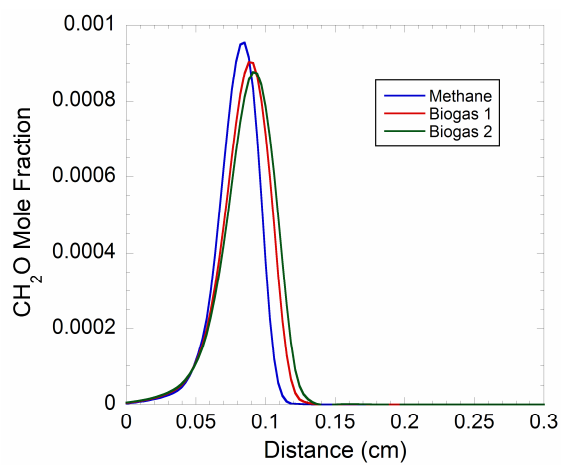
(d)



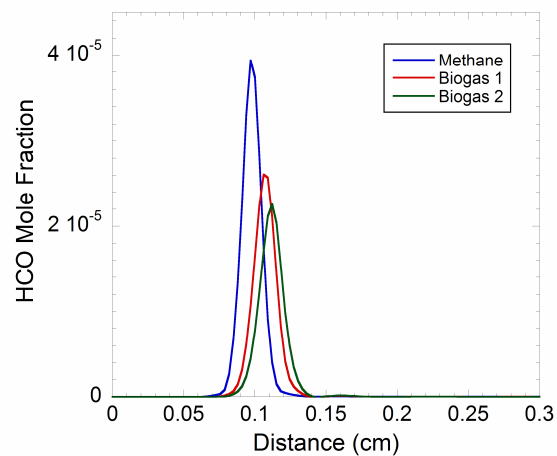
(e)



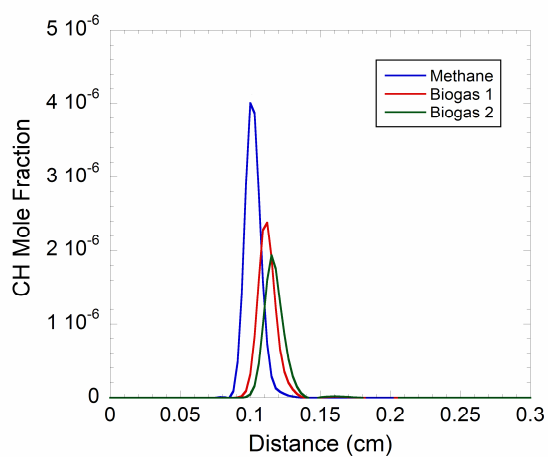
(f)



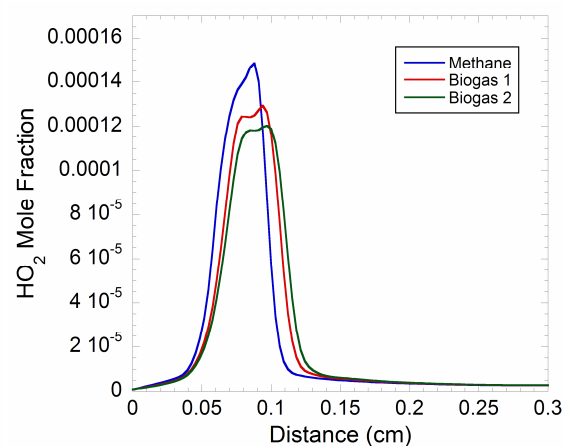
(g)



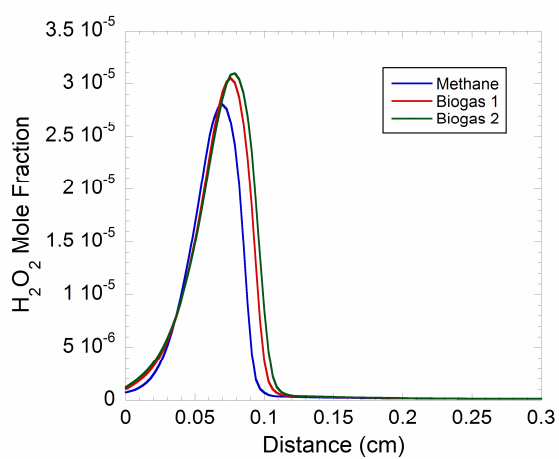
(h)



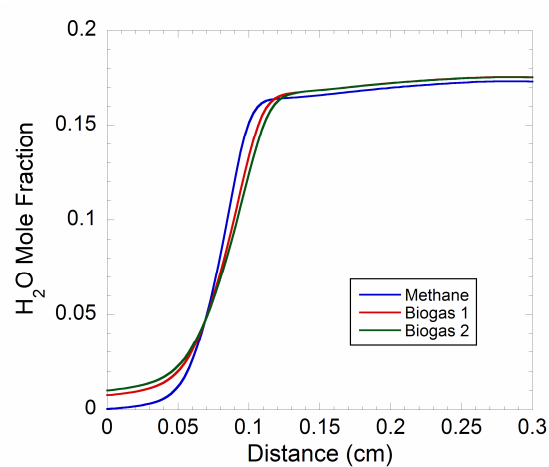
(i)



(j)



(k)



(l)

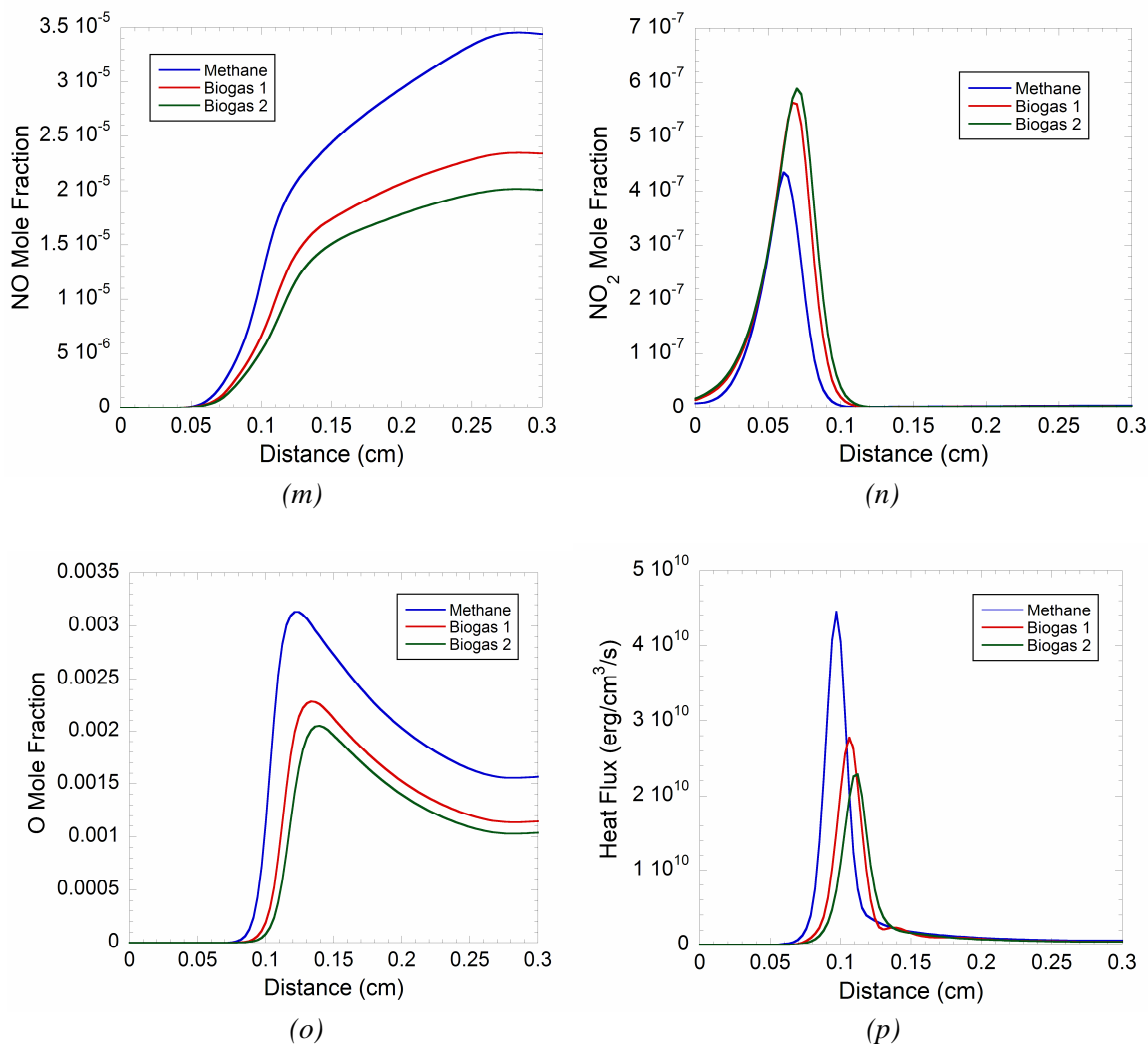


Figure 4. Temperature, axial-velocity, heat generation, and selected species mole-fraction profiles for methane-air and biogas-air laminar premixed flames ($\phi = 1$, $T_{in} = 298$ K, $P = 1$ atm).

While the fuel is completely gone in about 1 mm and the major portion of the total temperature rise occurs in the same interval, the approach to equilibrium conditions is relatively slow beyond this threshold. In fact, we can see that equilibrium has yet to be reached even at the 3-mm location. This slow approach to equilibrium is primarily a consequence of the dominance of three-body recombination reactions in this region. Plotting mole fractions as a function of distance, rather than time, emphasizes the slow approach to equilibrium somewhat as a

consequence of the stretching of the distance-time relation ($dx = v_x dt$) through continuity ($\rho v_x = \text{const}$). For instance, given the same time interval, a fluid particle in the hot, high-velocity region of the flame travels along a distance which is greater than a fluid particle in the cold, low-velocity region.

Figure 4m focuses on nitric oxide production. Here we can see a rapid rise in the nitric oxide mole fraction in the same region where the CH radical is present in the flame. This is followed by a continual, almost linear, increase in the nitric oxide mole fraction. In the latter region, nitric oxide formation is dominated by Zeldovich kinetics. Of course, the nitric oxide mole-fraction curve must bend over at some point downstream, as reverse reactions become more important, and approach the equilibrium condition asymptotically.

For what concerns fuel comparisons, we can easily state that biogas behaves again like methane, since the curve trend seems to be the same for all fuels, although all quantities can present quite large discrepancies. In particular, Figure 4a shows how temperature is almost the same for all cases, while the axial-velocity profiles are very far from each other, with methane presenting considerably higher values. The latter fact also occurs when analyzing the heat generation, since it is easy to see how the heat flux produced when burning methane is considerably higher than that of both considered biogases (in particular, biogas 1 and 2 lose respectively 38.2% and 48.8% of heat production if compared to methane). Speaking about emissions, biogas carbon-dioxide emissions are higher than for methane, and this is once again due to the fact that carbon dioxide is contained in the fuel itself, while biogas carbon-monoxide emissions are lower than for methane (as well as in the equilibrium calculation), with the mole-fraction peak moving to the right as methane content in the fuel is decreased. An interesting point is represented by the fact that, while nitric-oxide emissions are higher for the methane case (as were in the equilibrium calculation), nitrogen-dioxide production is higher for the biogas cases, with biogas 2 being more polluting than biogas 1. However, an NO_x -emission-index analysis (as reported in Figure 5) can easily confirm how methane nitrogen-oxides emissions are generally

more important than for both chosen biogases. In fact, methane presents an NO_x -emission index which is almost twice as that of both biogases, with curves being strongly affected by nitrogen-oxide emissions (higher for methane) over nitrogen-dioxide production (higher for both biogases). This turns out to be even clearer by comparing Figure 5 to Figures 4m and 4n, with the first and the second figure basically showing the same evolution.

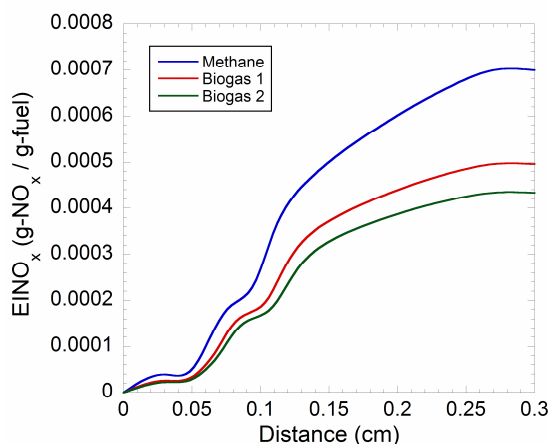


Figure 5. NO_x -emission-index analysis ($\phi = 1$, $T_{in} = 298$ K, $P = 1$ atm).

3.5.1 Flame-Speed Computation

Figure 6 presents a bar diagram showing different values of flame speed for each fuel, with the same conditions used above (initial temperature is 298 K, equivalence ratio is set to unity, and pressure is 1 atm, while the axial distance is set to be 3 mm). Flame speed can be easily computed by *CHEMKIN*, since it is simply the first value in the axial-velocity column solution, i.e., the velocity of the flame front. Once again, it is clear that the more methane is contained in the fuel the higher will be the flame speed. In particular, biogas 1 has a flame speed (with stoichiometric

conditions) which is lower than that of methane of about 29%, while biogas 2 loses 37% of flame speed with respect to methane. When feeding a generator with biogas, these considerably large losses would probably strongly affect the performance, but it is well-known how losing performance may be necessary when the designer is aiming to bring down the emissions of pollutants.

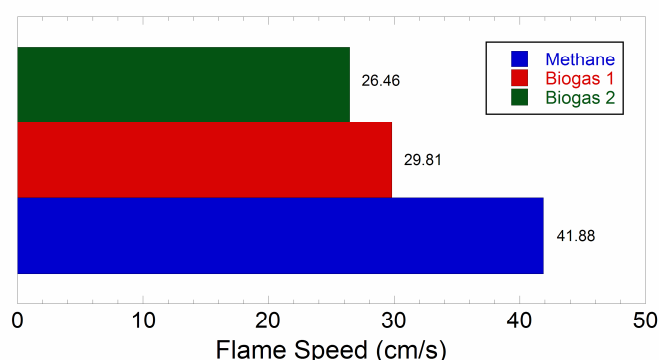


Figure 6. Flame speed of considered fuels ($\phi = 1$, $T_{in} = 298$ K, $P = 1$ atm).

3.5.2 Influence of Equivalence Ratio on Flame Speed

Figure 7 presents how equivalence ratio can largely affect flame speed. Initial temperature is 298 K, while pressure is set to be 1 atm. Generally, flame speed increases for poor mixtures and decreases when burning a rich mixture. Peak flame speed is for equivalence ratios contained inbetween 1 and 1.1. Trend is the same for each curve, with biogas curves looking somehow enlarged in correspondence of the maximum peak. In particular, both biogases show a practically constant flame speed for equivalence ratios inbetween 0.85 and 1.15, while the methane peak flame speed turns out to be much easier to detect.

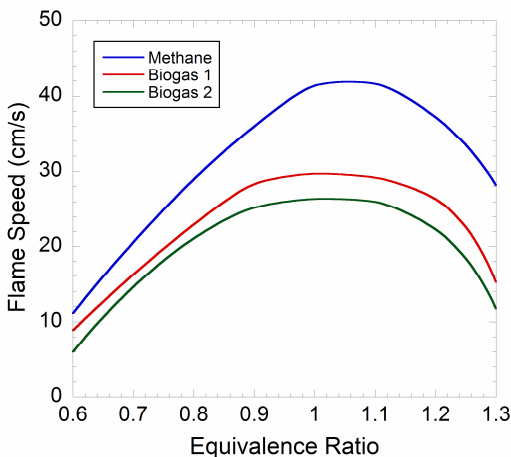


Figure 7. Influence of equivalence ratio on flame speed ($T_{in} = 298$ K, $P = 1$ atm).

3.5.3 Methane Experimental Validation

Figure 8, 9, and 10 present an experimental validation for the methane case. In fact, they show how methane flame speed varies with respect to equivalence ratio at different pressures (1, 2, and 5 atm, respectively). Flame speed gets a considerably lower value as pressure increases; in particular, at 5 atm the flame speed of a stoichiometric mixture is halved than at atmospheric pressure. The match between simulation and experimental results (taken from available literature^{[23]-[27]} for non-stretched laminar flames) is quite good, except for the 5-atm curves, where *CHEMKIN* points out considerably lower values of flame speed as the methane-air mixture gets richer.

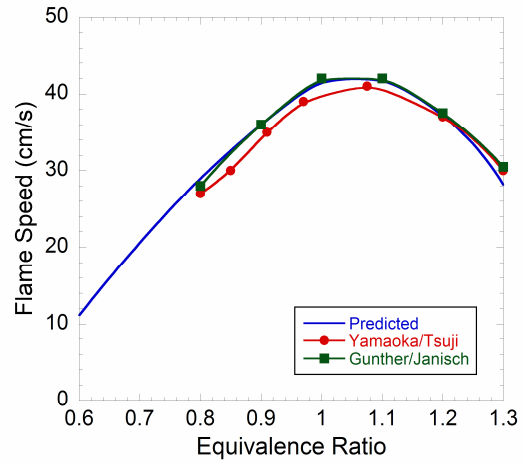


Figure 8. Experimental validation for the methane case ($P = 1$ atm).

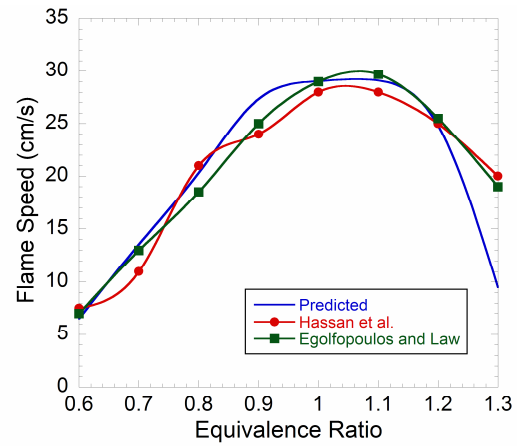


Figure 9. Experimental validation for the methane case ($P = 2$ atm).

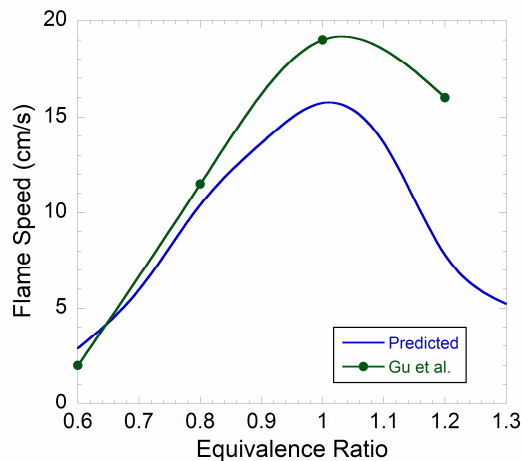


Figure 10. Experimental validation for the methane case ($P = 5$ atm).

No experimental validation for biogas is given in the present work. In particular, available literature does not contain much about biogas combustion and this could represent a good challenge for the future studies. The aim of this work, as we said before, is to examine biogas as it was a mixture of methane and a certain number of main contaminants. In this sense, methane experimental validation (widely made in the past for the principal combustion issues) can be enough, and simulation work may become a precious tool for the study of alternative fuels, since it may guarantee good approximations and a sensible gain in terms of time and costs (we must not forget how the build-up of an experimental setup can take many months and can be affected by sensible costs).

3.5.4 High-Pressure Study and Methane Validation

Figure 11 shows how flame speed of the considered fuels varies as pressure increases up to 50 atm. Initial temperature is set to 300 K and equivalence ratio is set to unity. Each curve presents the same trend again, with flame speed dramatically decreasing between 1 atm and 7 atm and slightly decreasing for higher pressures. In particular, at 7 atm flame speed feels a 30 cm/s drop off for methane and a 20 cm/s drop off for both biogases (if compared with the atmospheric-

pressure case), with an only 2-3 cm/s drop off for pressures contained in the range 7-50 atm for all fuels.

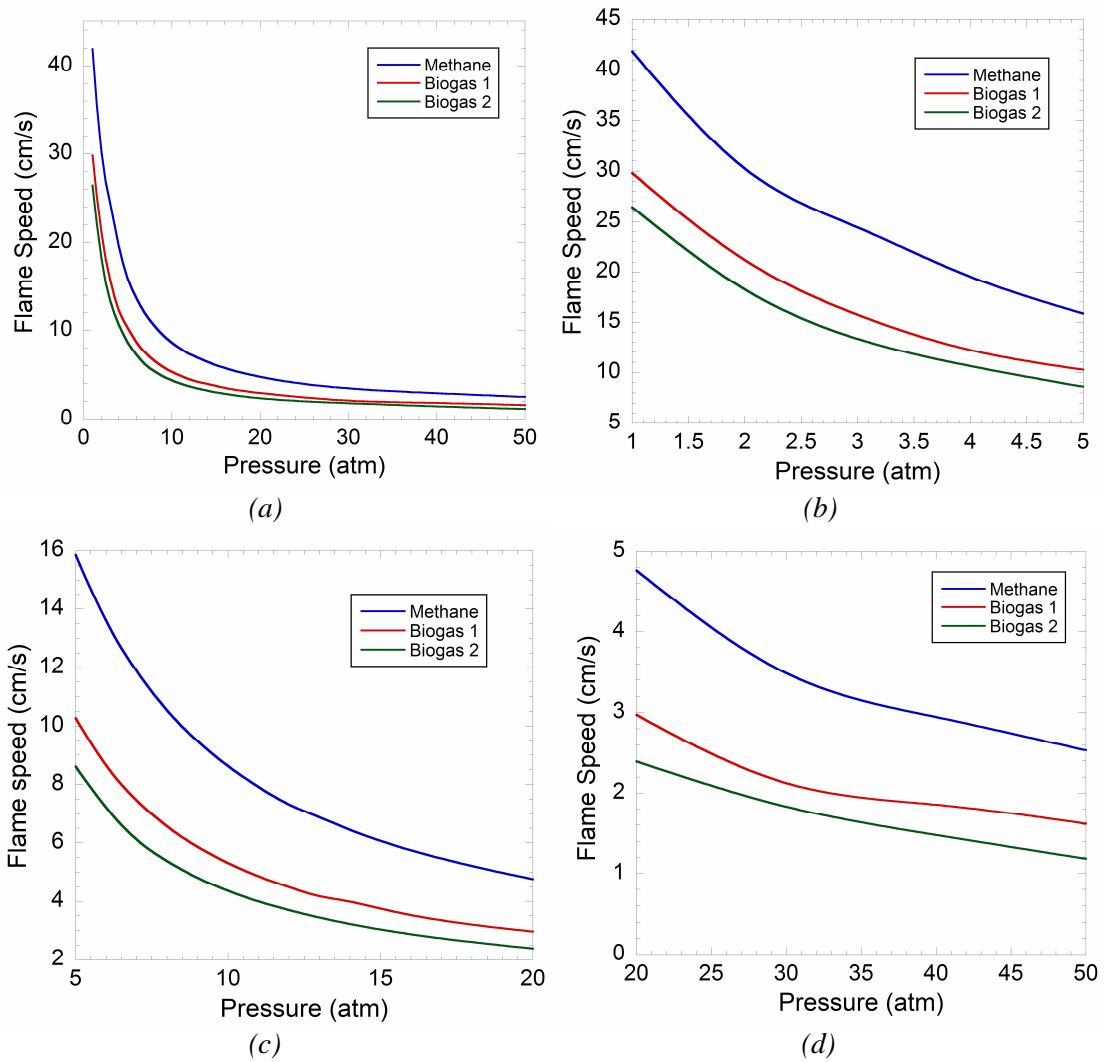


Figure 11. Flame speed of considered fuels for pressures up to 50 atm ($\phi = 1$, $T_{in} = 300$ K).

Figure 12 presents an experimental validation for methane (with data taken again from available literature^{[28]-[30]}) for pressures which are contained in the range 1-3 atm. Initial temperature is 300

K, while equivalence ratio is set to unity. Although flame-speed values may show quite large discrepancies, depending on the different experimental setups made for each case, we can state that the match between simulation and experimental results is quite good.

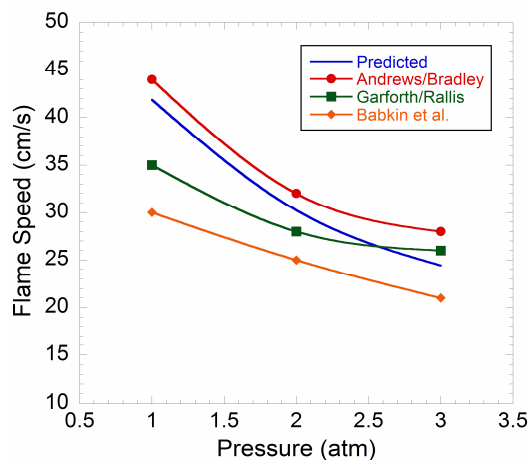


Figure 12. Experimental validation for the methane case in the range 1-3 atm ($\phi = 1$, $T_{in} = 300$ K).

At last, Figure 13 presents another experimental validation for methane for pressures up to 20 atm^[31], showing a good match between simulation and experimental results. Initial temperature is 300 K and equivalence ratio is set to unity. No experimental validation for biogas is given.

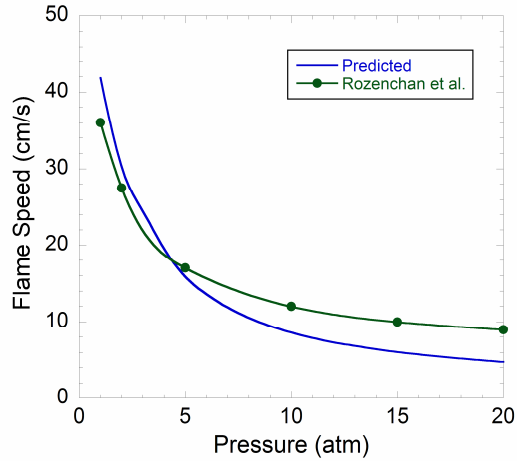


Figure 13. Experimental validation for the methane case in the range 1-20 atm ($\phi = 1$, $T_{in} = 300$ K).

3.5.5 Overall Reaction Order and Methane Validation

Figure 14 shows the trend of the overall reaction order for a stoichiometric methane-air mixture for pressures up to 40 atm. Initial temperature is set to be 300 K. The overall reaction order, which is very useful to understand how pressure can affect flame speed, is defined as follows^[25]:

$$n = 2 + 2 \left(\frac{\partial \ln S_u^0}{\partial \ln P} \right), \quad (32)$$

where P pressure and S_u^0 is the non-stretched laminar flame speed, since S_u^0 can be expressed as a function of pressure:

$$S_u^0 = P^{\frac{n}{2}-1}. \quad (33)$$

Figure 15 presents an experimental validation for methane overall reaction order for pressures up to 3 atm (with data taken from Egolfopoulos and Law^[26]) and for pressures up to 20 atm (with data taken from Rozenchan et al.^[31]). Experimental data exhibit a quite good agreement with GRI

3.0 simulation results, as shown in Som and Aggarwal^[32]. No experimental data are available for biogas yet.

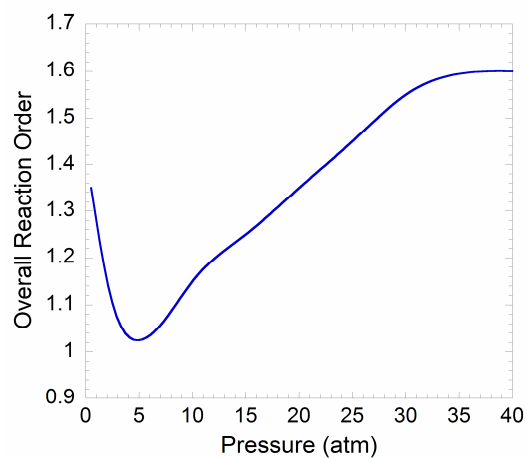


Figure 14. Overall reaction order for a methane-air mixture for pressures up to 40 atm ($\phi = 1$, $T_{in} = 300$ K).

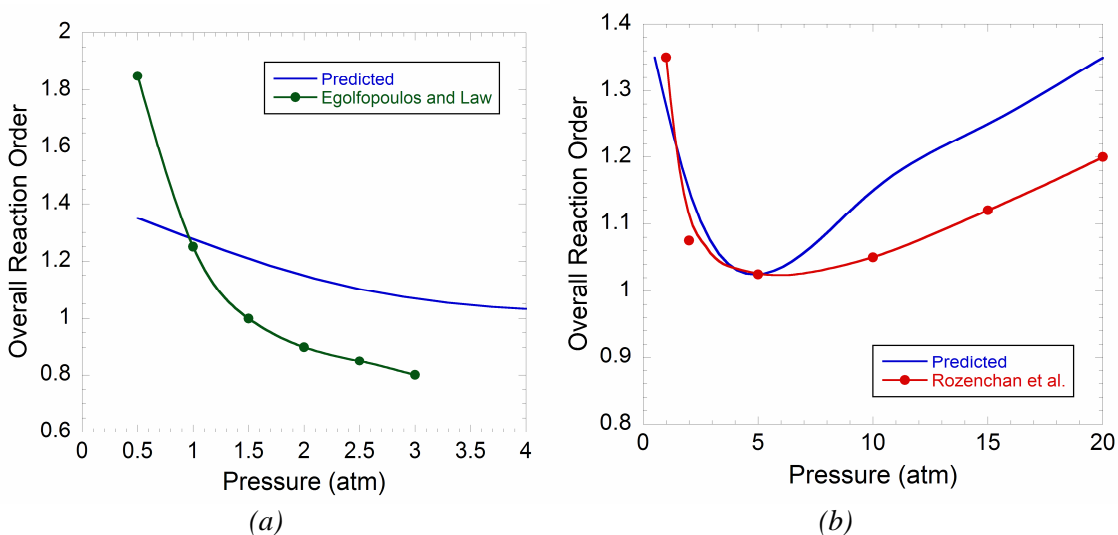


Figure 15. Experimental validation for the methane case for pressures up to 3 and 20 atm, respectively ($\phi = 1$, $T_{in} = 300$ K).

CHAPTER 4

BIOGAS PARTIALLY PREMIXED FLAMES

4.1 Introduction

Partially premixed flames have been the subject of much fundamental research and recently they have been used to develop models capable to explain how soot is formed in diffusion burning. Many residential gas appliances, like cooking ranges and ovens, employ partially premixed flames. In these applications, the fuel stream is usually partially premixed with air, which is essential to provide non-sooting operation. Although many analytical and numerical analysis of partially premixed flames have been performed, recent concerns with indoor air quality and pollutant emissions have resulted in the use of more complex design methods. Of particular concern are the emissions of nitrogen dioxide and carbon monoxide, both of which are detrimental to human health^[16].

4.2 Counter-Flow Flames

In the past few decades, many theoretical and experimental studies have been conducted on flames fed by opposing jets of fuel and oxidizer. Such flames are of fundamental research interest because they approximate a one-dimensional character and because residence times within the flame zone can be easily varied. In fact, modelling a two-dimensional axis-symmetric jet flame may show many complexities; in contrast, the one-dimensionality of counter-flow flames makes both experiments and calculations much more practicable. For instance, in experiments, temperature and species conservation measurements need only to be made along a single line; while, in theoretical studies, only modest run times are needed for computation using extremely complex chemical kinetics. The counter-flow flames provide fundamental understanding of the detailed structure of diffusion flames and their extinction characteristics. Furthermore, the laminar counter-flow flames have been proposed as a fundamental element in the complex

structure of turbulent non-premixed flames. A rather large counter-flow literature has developed and continues to expand^{[33]-[36]}, with applications varying from gas turbine combustors to spark ignition^[37] and diesel engines^[38].

Before presenting a mathematical description, it is important to understand the basic features of counter-flow flames. A typical experimental arrangement is illustrated in Figure 16. Here we can see opposing jets of fuel and oxidizer, which create a stagnation plane ($v_x = 0$) whose location depends on the relative magnitudes of the oxidizer and fuel jet initial momentum fluxes. For equal momentum fluxes ($\dot{m}_F v_F = \dot{m}_{Ox} v_{Ox}$), the stagnation plane lies at the midpoint between the nozzle exit planes; however, if the momentum flux of one stream is increased over the other, the stagnation plane moves closer to the low-momentum-flux stream outlet. Given appropriate conditions, a diffusion flame can be established between the two nozzles, the location of which is where the mixture fraction is nominally stoichiometric. For most hydrocarbon fuels burning in air, stoichiometric conditions require considerably more air than fuel ($f_{stoic} \approx 0.06$). In this case, then, the fuel must diffuse across the stagnation plane to the flame location, as shown in Figure 16. Conversely, if a reactant pair in which more fuel than oxidizer is required for stoichiometric conditions ($f_{stoic} > 0.5$), the flame would lie on the fuel side of the stagnation plane. An important characteristic of the opposed flow is that the flame established between the nozzles is essentially flat (a disk for round nozzles) and one-dimensional, having dependencies only in the x -direction^[15].

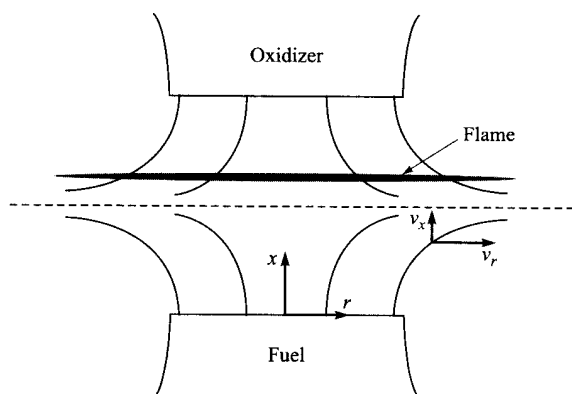


Figure 16. Counter-flow flame configuration. Diffusion flame lies above stagnation plane (dashed line) created by opposing streams of fuel and oxidizer.

4.3 Analyzing Opposed-flow Diffusion Flames with CHEMKIN^[17]

Governing equations for opposed-flow flames rely on a similarity transformation that reduces the three-dimensional nature of the flow to a one-dimensional (axial) dependence of the governing equations. This discussion pertains to the *CHEMKIN* Reactor Model: Diffusion or Premixed Opposed-flow Flame.

4.3.1 Axisymmetric and Planar Diffusion

For the Opposed-flow Flame model, a steady-state solution is computed for either axisymmetric or planar diffusion flames between two opposing nozzles. The opposed-flow geometry makes an attractive experimental configuration, because the flames are flat, allowing for detailed study of the flame chemistry and structure. The two or three-dimensional flow is reduced mathematically to one dimension by assuming that the y - or radial velocity varies linearly in the y - or radial direction, which leads to a simplification in which the fluid properties are functions of the axial distance only. The one-dimensional model then predicts the species, temperature, and velocity profiles in the core flow between the nozzles (neglecting edge effects). Both premixed and non-premixed flames can be simulated.

The axisymmetric geometry consists of two concentric, circular nozzles directed towards each other, as in Figure 17. This configuration produces an axisymmetric flow field with a stagnation plane between the nozzles. The planar geometry consists of two concentric linear nozzles directed towards each other as shown in Figure 18. This configuration produces a two-dimensional planar flow field with a stagnation line between the two nozzles. An axisymmetric geometry has been employed for the present study, in order to point out the dominance of the phenomena occurring along the axial coordinate (one-dimensional problem). The location of the stagnation plane depends on the momentum balance of the two streams. When the streams are premixed, two premixed flames exist, one on either side of the stagnation plane. When one stream contains fuel and the other oxidizer, a diffusion flame is established. Since most fuels require more air than fuel by mass, the diffusion flame usually sits on the oxidizer side of the stagnation plane; fuel diffuses through the stagnation plane to establish the flame in a stoichiometric mixture.

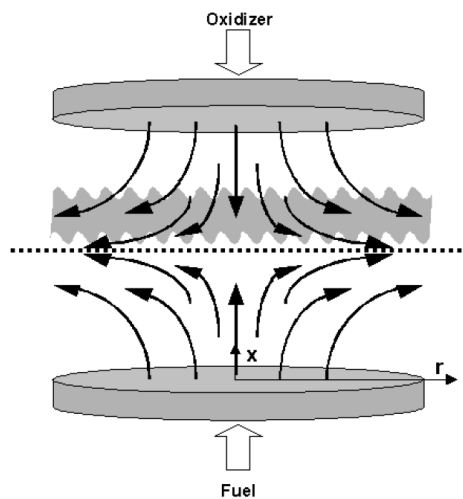


Figure 17. Geometry of the axisymmetric opposed-flow diffusion flame. The dashed line represents the stagnation flame; the shaded region suggests the flame.

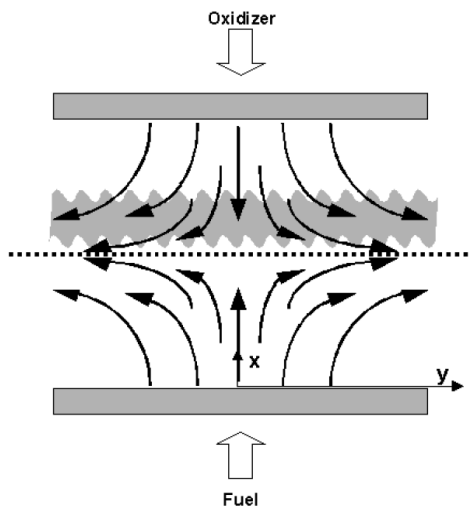


Figure 18. Geometry of the planar opposed-flow diffusion flame. The dashed line represents the stagnation flame; the shaded region suggests the flame.

Our Opposed-flow Flame Model is derived from a model that was originally developed by Kee, et al.^[39] for premixed opposed-flow flames. The reduction of the three-dimensional stagnation flow is based upon similarity solutions advanced for incompressible flows by von Karman^[40], which are more easily available in Schlichting^[41]. The *CHEMKIN* impinging and stagnation-flow models are based on a finite domain, where the user specifies the nozzle separation. For this approach, an eigenvalue must be included in the solution of the equations and the strain rate varies, such that a characteristic strain rate must be determined from the velocity profile. Following the analysis of Evans and Grief^[42], Kee, et al.^[39] showed that this formulation allowed more accurate predictions of the extinction limits for premixed flames than other approaches.

The geometry and axes for the axisymmetric and planar configurations are sketched in Figure 17 and Figure 18, respectively. In the following equations, ξ represents either the radial direction r for the axisymmetric case, or the perpendicular direction y for the planar case. The coordinate parameter n allows us to present one set of equations for both cases, with $n = 3$ for the three-dimensional axisymmetric flow and $n = 2$ for the two-dimensional planar case. A more

detailed derivation of the governing equations for the opposed-flow geometry is provided by Kee, et al.^{[39], p.192}.

At steady-state, conservation of mass in cylindrical or planar coordinates is:

$$\frac{\partial(\rho u)}{\partial x} + \frac{1}{\xi^{n-2}} \frac{\partial(\rho v_\xi \xi^{n-2})}{\partial \xi} = 0, \quad (34)$$

where u and v_ξ are the axial and radial (or cross-flow) velocity components, and ρ is the mass density. Following von Karman^{[40], p.192}, who recognized that v_ξ/ξ and other variables should be functions of x only, we define:

$$G(x) = \frac{\rho v_\xi}{\xi}, \quad (35)$$

$$F(x) = \frac{\rho u}{n-1}, \quad (36)$$

for which the continuity equation (34) reduces to:

$$G(x) = \frac{dF(x)}{dx}, \quad (37)$$

for the axial velocity u . Since F and G are functions of x only, so are ρ , u , T and Y_k . The perpendicular momentum equation is satisfied by the eigenvalue:

$$H = \frac{1}{\xi^{n-2}} \frac{\partial p}{\partial \xi} = \text{constant}. \quad (38)$$

The perpendicular momentum equation is:

$$H - (n-1) \frac{d}{dx} \left(\frac{FG}{\rho} \right) + \frac{nG^2}{\rho} + \frac{d}{dx} \left[\mu \frac{d}{dx} \left(\frac{G}{\rho} \right) \right] = 0. \quad (39)$$

Energy and species conservations are:

$$\rho u \frac{dT}{dx} - \frac{1}{c_p} \frac{d}{dx} \left(\lambda \frac{dT}{dx} \right) + \frac{\rho}{c_p} \sum_k c_{pk} Y_k V_k \frac{dT}{dx} + \frac{1}{c_p} \sum_k h_k \dot{\omega}_k = 0, \quad (40)$$

$$\rho u \frac{dY_k}{dx} + \frac{d}{dx} (\rho Y_k V_k) - \dot{\omega}_k W_k = 0 \quad k = 1, \dots, K, \quad (41)$$

where the diffusion velocities are given by either the multicomponent formulation:

$$V_k = \frac{1}{X_k \bar{W}} \sum_{j \neq k}^K W_j D_{k,j} \frac{dX_j}{dx} - \frac{D_k^T}{\rho Y_k} \frac{1}{T} \frac{dT}{dx}, \quad (42)$$

or the mixture-averaged formulation:

$$V_k = -\frac{1}{X_k} D_{km} \frac{dX_k}{dx} - \frac{D_k^T}{\rho Y_k} \frac{1}{T} \frac{dT}{dx}, \quad (43)$$

where:

$$D_{km} = \frac{1 - Y_k}{\sum_{j \neq k}^K \frac{X_j}{D_{jk}}}, \quad (44)$$

and $D_{k,j}$, D_{km} , D_{jk} , D_k^T are the multicomponent, mixture-averaged, binary, and thermal diffusion coefficients, respectively.

The boundary conditions for the fuel (F) and oxidizer (O) streams at the nozzles are:

$$x = 0 : \quad F = \frac{\rho_F u_F}{n-1}; \quad G = 0; \quad T = T_F; \quad \rho u Y_k + \rho Y_k V_k = (\rho u Y_k)_F; \quad (45)$$

$$x = L : \quad F = \frac{\rho_O u_O}{n-1}; \quad G = 0; \quad T = T_O; \quad \rho u Y_k + \rho Y_k V_k = (\rho u Y_k)_O. \quad (46)$$

Note that the inflow boundary condition (46) specifies the total mass flux, including diffusion and convection, rather than the fixing species mass fraction $Y_k = Y_{k,F}$. If gradients exist at the boundary, these conditions allow diffusion into the nozzle.

The differential equation (37) through equation (41) and boundary conditions (46) form a boundary value problem for the dependent variables (F , G , H , T , Y_k). The GAS-PHASE KINETICS Subroutine Library provides the reaction rates and thermodynamic properties, while the TRANSPORT package evaluates the transport properties for these equations.

4.3.2 Finite Difference Approximations

Discretization of the differential equations uses conventional finite differencing techniques for non-uniform mesh spacing. Diffusive terms use central differences, with truncation error that is second-order in the mesh spacing. For better convergence, convective terms use upwind differencing, which uses the sign of the velocity to choose which direction the spatial difference will go. If $u_j = 0$, for example, then the convective term in the energy equation is differenced as:

$$\rho u \frac{dT}{dx} \approx \rho_i u_j \left(\frac{T_j - T_{j-1}}{x_j - x_{j-1}} \right). \quad (47)$$

The truncation error of this approximation is first-order in the mesh spacing, leading to what is often called “artificial diffusion”, but this form avoids unwanted oscillations during the solution on a coarse mesh. Alternatively, the convective terms can be centrally differenced, but the default windward differencing is recommended.

4.3.3 Regrid Operation

A Regrid operation is specified by supplying a new number of grid points during a restart or continuation, which allow a new flame solution to begin from an initial guess based on the solution of a previous flame.

The steady-state solver, TWOPNT, automatically refines the grid by adding points in regions where they are needed to resolve the first and second derivatives of the solution, using criteria controlled by the Gradient and Curvature grid parameters. However, TWOPNT does not move or remove points. If it reaches a maximum number of points (internally defined by the dimensions), a warning message is printed and the adaptation is terminated. In some cases, then, it may be necessary to reduce the number of points when starting a new solution from a previous result. The Regrid operation redefines the solution guess on the user-specified number of mesh points.

The Regrid operation is different from the grid-point insertion operation performed by TWOPNT. Both operations attempt to resolve the gradient and curvature in the solution, except

that TWOPNT considers all solution components, whereas Regrid only considers the temperature profile. TWOPNT only adds points, leaving the old points as they were, but Regrid alters the location and solution of all the points interior to the boundaries. Regrid computes new locations for exactly the given number of points, and then interpolates the solution from the previous grid to obtain a new approximation of the solution. Regrid does not conserve any properties of the solution; in fact, it tends to smooth the solution by the error inherent in the interpolation.

Regrid redistributes a weighting function of the first and second derivatives of the temperature. The profiles of the other dependent variables are ignored on the assumption that the temperature profile defines the flame location well enough for the purposes of realigning the mesh for an initial condition. The redistribution uses a transformation from the physical coordinate x to a new coordinate η :

$$\frac{dx}{d\eta} W(x, T) = C \quad , \quad (48)$$

with the weighing function:

$$W(x, T) = 1 + b_1 \left| \frac{dT}{dx} \right| + b_2 \left| \frac{d^2T}{dx^2} \right| \quad . \quad (49)$$

Integration over the entire domain defines the constant:

$$C = \frac{1}{N-1} \int_0^L W(x, T) dx \quad . \quad (50)$$

Integrating over a portion of the domain gives an expression for the point locations in η -space:

$$\eta = 1 + \frac{1}{C} \int_0^x W(x, T) dx \quad . \quad (51)$$

The new grid locations come by interpolation between the computed values of η defined using the old mesh, onto a uniform mesh in η -space. Since $d\eta$ is constant on this uniform mesh, the solution to equation (48) states that $W(x, T)dx$ is constant, so the new values of will be concentrated where the weighting function is large.

4.4 How to Perform an Opposed-Flow-Diffusion-Flame Calculation with CHEMKIN

When performing a partially-premixed-flames simulation, the user has to carry out the same preliminary operation as done in the previous cases (it is necessary to choose whether to use a *CHEMKIN* sample or to create a new chemistry set if working with a new project; the working directory must be set and three different files must be entered: the Gas-Phase Kinetics File, the Thermodynamics Data File, and the Gas Transport Data File, which are all taken from GRI 3.0 mechanism). After opening the Cluster window, the user has to define reactor physical properties (problem type, i.e., *Solve Gas Energy Equation*, plateau profile for initial guess, maximum temperature for initial profile, and pressure must be set; the user can also decide to use Mixture-averaged Transport Model or Multicomponent Model), initial grid properties (containing the data regarding grid points and axial position), and species-specific properties (if any). Then stream properties and species-specific properties must be specified in the Inlet windows (for both the fuel and the oxidizer): the user has to set the mass flow rate (or the inlet velocity) and the inlet temperature, and to define the reactant species by expressing them on a mole-fraction or mass-fraction base. In particular, mole fractions of the fuel-mixture species, mole fractions of the oxidizer-mixture species, and complete combustion products must be entered. Remaining parameters to be set in order to run a simulation are the Solver data (concerning tolerances, time-stepping, and finite difference methods) and the Output Control data (where Print Level Control is the only necessary parameter to be set). The last option in the Cluster section concerns again the possibility for the user to set a certain number of continuations. When everything is set in the latter window, a simulation can be run by creating an input file first. When the simulation is done, the user can examine all quantities of interest by opening the output file and post-processor can be run.

4.5 Simulation Results

We can now employ the counter-flow flame model described above together with *CHEMKIN* library codes to analyze the structure of methane-air and biogas-air diffusion flames. Figure 19 shows computed temperature and velocity profiles between the fuel (left) and air (right) nozzles. Distance between the nozzles is set to be 2 cm, pressure is 1 atm, equivalence ratio at the fuel nozzle is set to unity, and the global strain rate is set to 150 s^{-1} , while inlet temperature is 300 K for both the fuel and the oxidizer streams. Before analyzing the flame structure, it is important to explain how to define all these input parameters. When studying partially premixed flames, the main parameters of interest are the equivalence ratio of the fuel stream and the strain rate; thus, in order to carry out an interesting computation, it may be necessary to fix both of them. Since *CHEMKIN* opposed-flow-flame model does not allow the user to directly define the equivalence ratio of the fuel inlet in the Cluster window, the most useful way to proceed is to fix the equivalence ratio by computing the air premixing and, consequently, the mole fractions of every chemical species at the fuel nozzle, and to fix the global strain rate by computing inlet densities and velocities for both the fuel and the oxidizer. In particular, this latter operation can be made by solving a linear system of the following two equations:

$$a_s = \frac{2|v_o|}{L} \left(1 + \frac{|v_f|}{|v_o|} \sqrt{\frac{\rho_f}{\rho_o}} \right) \quad [43], \quad (52)$$

where a_s represents the global strain rate, L is the distance between the nozzles, v is the inlet velocity, and ρ is the density, while the subscripts indicate whether the quantities refer to the fuel or to the oxidizer, and:

$$\rho_o v_o^2 = \rho_f v_f^2, \quad (53)$$

which represents the conservation of momentum. Eventually, when the equivalence ratio at the fuel nozzle and the global strain rate are fixed, all computed input parameters can be entered and simulation can be run.

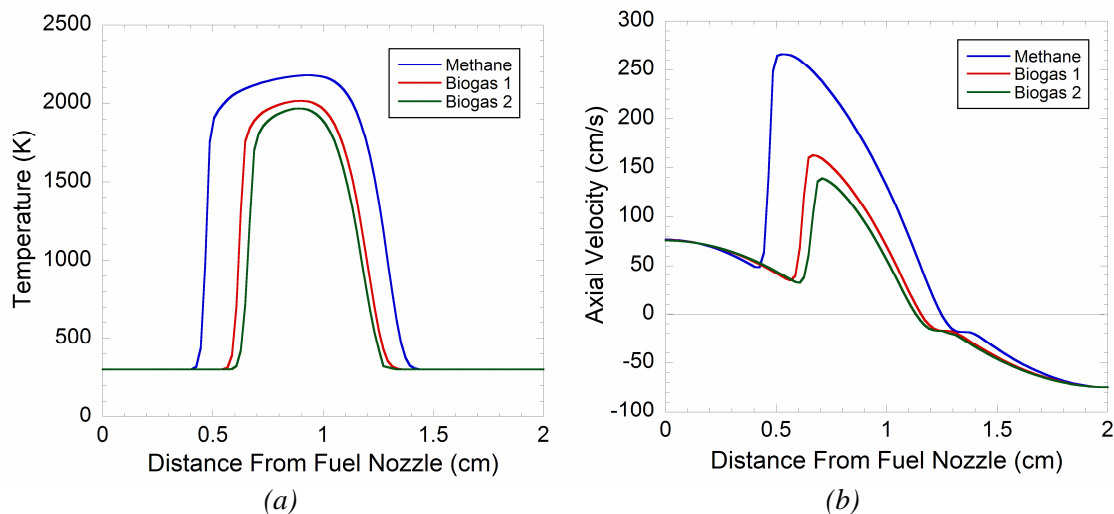


Figure 19. Temperature and axial-velocity profiles for methane-air and biogas-air counter-flow flames ($\phi = 1$, $T_{inlet} = 300$ K, $P = 1$ atm, $a_s = 150$ s⁻¹).

Focusing on the velocity profile, we see in Figure 19b that the stagnation plane ($v_x = 0$) lies to the right of the center plane between the two nozzles flows for all fuels, as expected, since the higher density of air causes the momentum flux of the air stream to be greater than that of the fuel stream for almost equal outlet velocities. The velocity profile exhibits interesting behavior in the heat-release region of the flame, where the maximum values ($v_x = 266.2$ cm/s for methane, $v_x = 162.8$ cm/s for biogas 1, $v_x = 139.2$ cm/s for biogas 2, respectively) occur to the fuel side of the peak temperatures (at $x = 0.53$ cm, $x = 0.66$ cm, $x = 0.70$ cm). We also note that these are the maximum absolute values of velocity. This result is understood as a consequence of continuity, with the gas speed increasing in response to the density decreasing. Frequently, a velocity gradient, dv_x/dx , is used to characterize the strain rate in counter-flow flames; for the twin-nozzle geometry, the relatively long region of essentially constant slope after the velocity maximum is used as a characteristic gradient. For the particular cases illustrated in Figure 19b,

we can easily see how the value of the velocity gradient is approximately the chosen value ($a_s = 150 \text{ s}^{-1}$).

A close inspection of Figure 19a reveals that the location of the peak temperatures is $x = 0.9$ for all fuels, while the values are $T = 2167.1 \text{ K}$ for methane, $T = 2015.2 \text{ K}$ for biogas 1, and $T = 1967.3 \text{ K}$ for biogas 2.

Turning to the species profiles reported in Figure 20, we focus first on the reactants. Here we see that both methane and oxygen mole fractions fall to near-zero values at axial locations which are very close to the center plane; this corresponds closely with the occurrence of the peak temperature. We also note some overlap, or non-simultaneous consumption of methane and oxygen, however small, in the region immediately preceding the maximum temperature (it may depend on the particular conditions of the simulations, since kinetics may be not sufficiently fast to guarantee a true approximation to a flame-sheet). Another interesting reactants-related feature is the presence of nitrogen deep on both sides. Since nitrogen in the flame system has its origins with the air, nitrogen must partly diffuse across the stagnation plane to yield the already relatively high concentrations we observe on the fuel side of the flame. Of course, the presence of fuel to the right of the stagnation plane is a result of diffusion in the direction opposite to nitrogen.

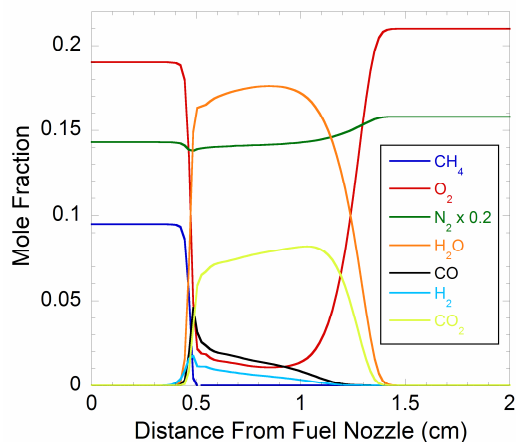


Figure 20. Mole-fraction profiles of main chemical species for methane-air counter-flow flames ($\phi = 1$, $T_{inlet} = 300$ K, $P = 1$ atm, $a_s = 150$ s⁻¹).

The stoichiometric case studied above can be considered as a general introduction to the flame structure study, since, usually, the fuel stream contains rich or slightly rich mixtures at the outlet. More realistic and specific cases will be treated in the next few paragraphs.

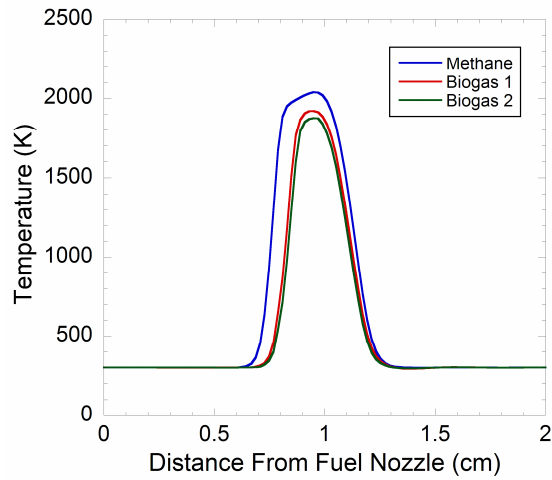
4.5.1 Best Cases

Figure 21 through Figure 24, together with Table IV through Table VII, are aimed to provide a wide range of data for a complete understanding of the flame structure for both methane and chosen biogases. Axial-velocity, temperature, and species mole-fraction profiles are reported. Distance between the two nozzles is 2 cm, pressure is 1 atm, while inlet temperature is set to 300 K for both the fuel and the oxidizer streams. Equivalence ratio of the fuel outlet varies, as well as the strain rate. In particular, equivalence ratio is set respectively to 1.4 and 3.0 (to help a comparison with experimental data taken from combustion literature, where these two values are the most commonly used^[32]), while the strain rate is set respectively to 150 s⁻¹ and 200 s⁻¹ (in order to guarantee relatively high inlet velocities). All combinations made by using the previous values are presented. Also, Figure 25 presents the particular case of a largely rich methane-air

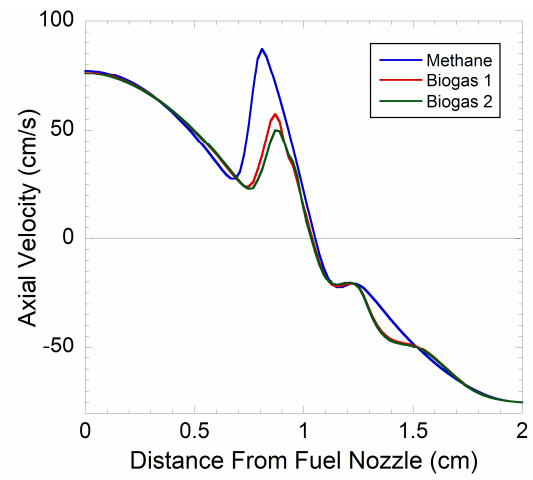
mixture at the fuel outlet ($\phi = 10$), with $a_s = 150 \text{ s}^{-1}$, in order to provide a better understanding of the influence of equivalence ratio at the fuel outlet.

Starting with some general considerations, we can easily state that biogas flames are generally narrower than methane flames, with biogas 2 having the narrowest flame, while axial velocity generally reaches higher values for the methane case. For what concerns the emissions of pollutants, we see how carbon-monoxide emissions are higher for methane, while carbon-dioxide emissions remain higher for the biogas cases, with biogas 1 being more polluting than biogas 2 again (carbon-dioxide content in the fuel is higher for biogas 1). Moreover, nitrogen-oxide production is higher for methane (followed by biogas 1 and biogas 2, respectively), while nitrogen-dioxide mole fraction shows a particular trend with two peaks, with emissions being practically zero in the middle point between the two nozzles: for slightly rich mixtures and higher strain rates, nitrogen-dioxide emissions become higher for biogas 1 than for methane, since the peak mole fractions of both biogas types exceed that of methane in the premixed zone. Eventually, C_2H_2 emissions are considerably lower for biogas for all cases, and this means a large reduction of soot formation in the exhaust gas.

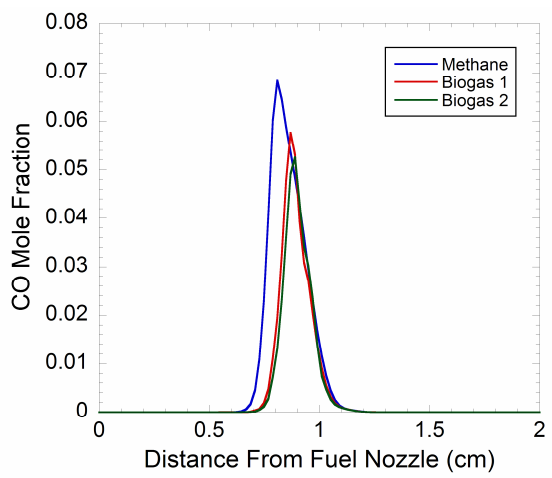
The location of peak species mole fractions and temperatures are shown in Table IV through Table VIII.



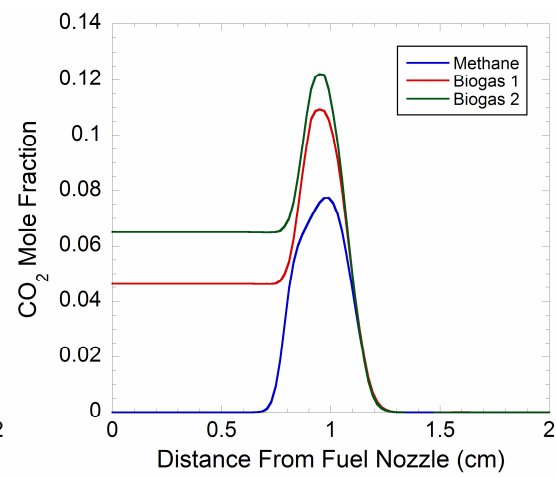
(a)



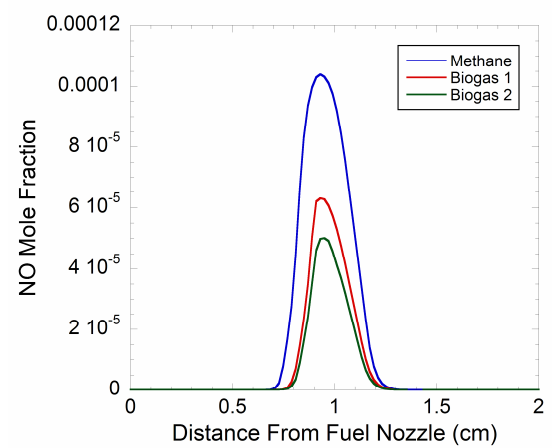
(b)



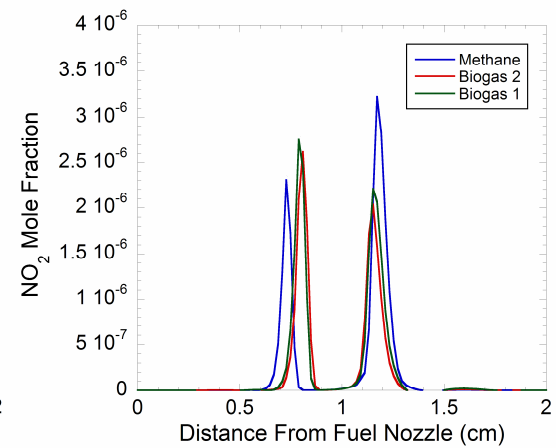
(c)



(d)



(e)



(f)

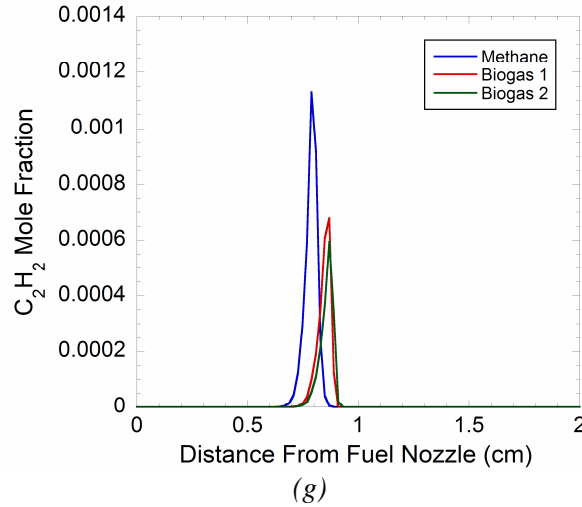
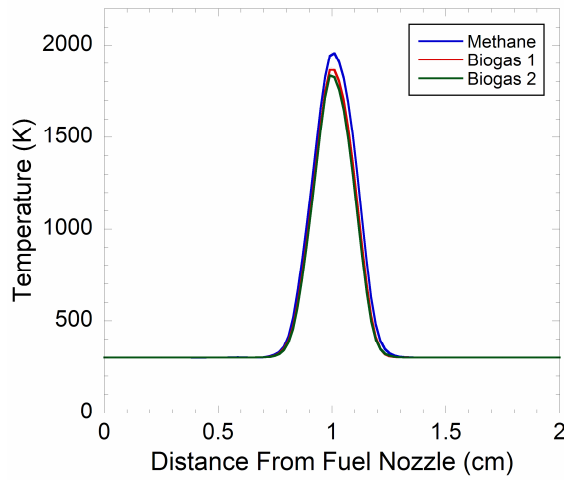


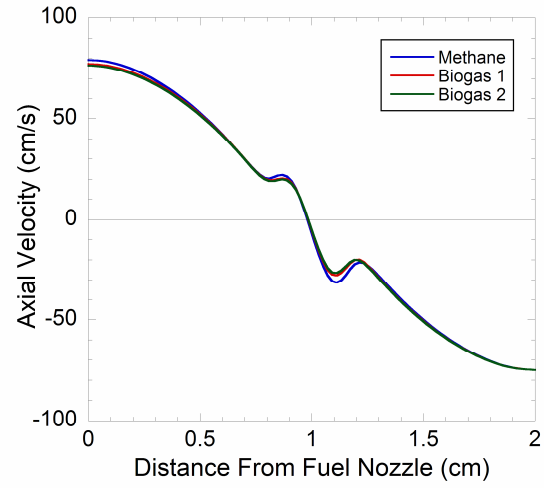
Figure 21. Temperature, axial-velocity, and mole-fraction profiles of main chemical species for methane-air and biogas-air counter-flow flames ($\phi = 1.4$, $T_{inlet} = 300$ K, $P = 1$ atm, $a_s = 150$ s⁻¹).

TABLE IV. LOCATION OF PEAK SPECIES MOLE FRACTIONS AND TEMPERATURES IN SIMULATED METHANE-AIR AND BIOGAS-AIR COUNTER-FLOW DIFFUSION FLAMES ($a_s = 150$ s⁻¹ AND $\phi = 1.4$ AT THE FUEL NOZZLE OUTLET).

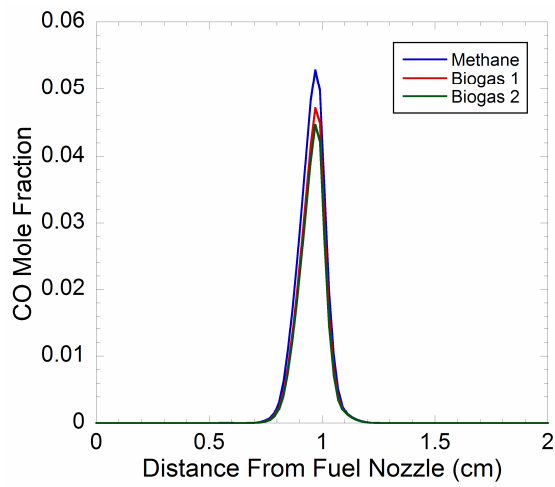
Species	Maximum Mole Fraction	Location of Maximum, x (cm)	Temperature (K)
Methane ($T = T_{max} = 2039.5$ K at $x = 0.95$ cm)			
H ₂	0.0395	0.7969	1792.2
H ₂ O	0.1703	0.8297	1952.6
CO	0.0683	0.8063	1873.3
CO ₂	0.0768	1	2003.1
NO	$1.03 \cdot 10^{-4}$	0.95	2039.5
NO ₂	$3.26 \cdot 10^{-6}$	1.175	737.1
Biogas 1 ($T = T_{max} = 1920.3$ K at $x = 0.95$ cm)			
H ₂	0.0244	0.8578	1646.2
H ₂ O	0.1698	0.9	1884.8
CO	0.0579	0.8719	1790.7
CO ₂	0.1094	0.95	1920.3
NO	$6.31 \cdot 10^{-5}$	0.9375	1917.7
NO ₂	$2.78 \cdot 10^{-6}$	0.7969	719.0
Biogas 2 ($T = T_{max} = 1877.2$ K at $x = 0.95$ cm)			
H ₂	0.0204	0.8672	1580.8
H ₂ O	0.1675	0.9063	1845.8
CO	0.0532	0.8813	1740.6
CO ₂	0.1224	0.95	1877.2
NO	$5.01 \cdot 10^{-5}$	0.9375	1875.2
NO ₂	$2.61 \cdot 10^{-6}$	0.8063	691.9



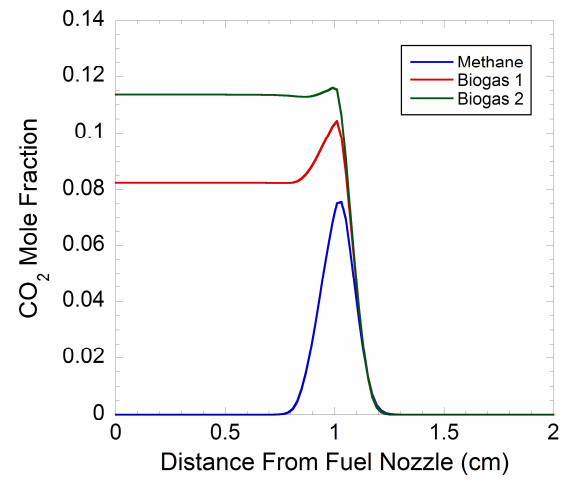
(a)



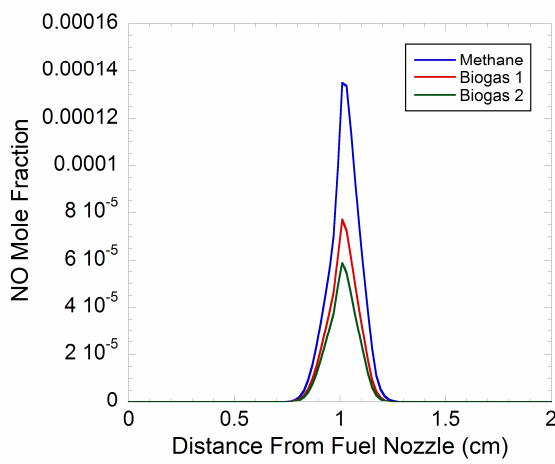
(b)



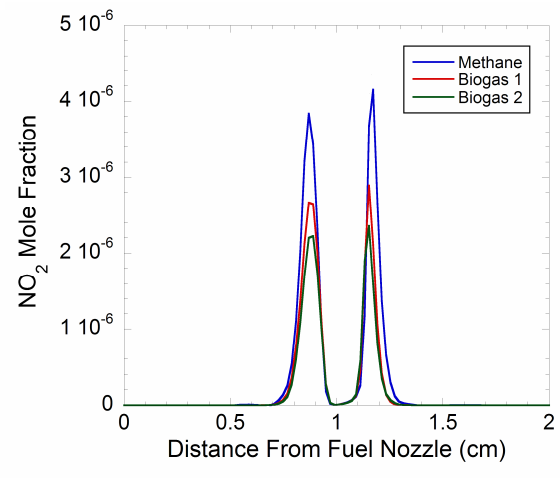
(c)



(d)



(e)



(f)

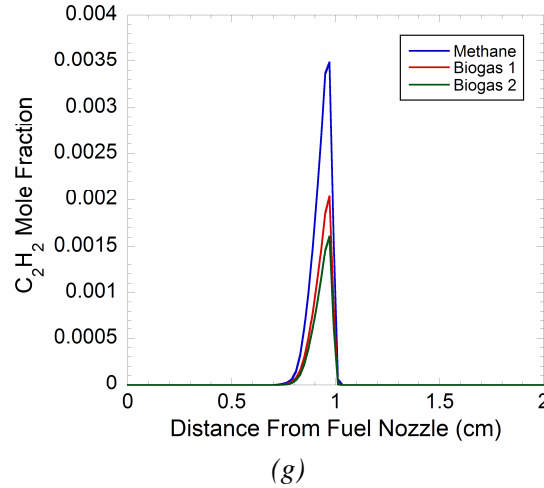
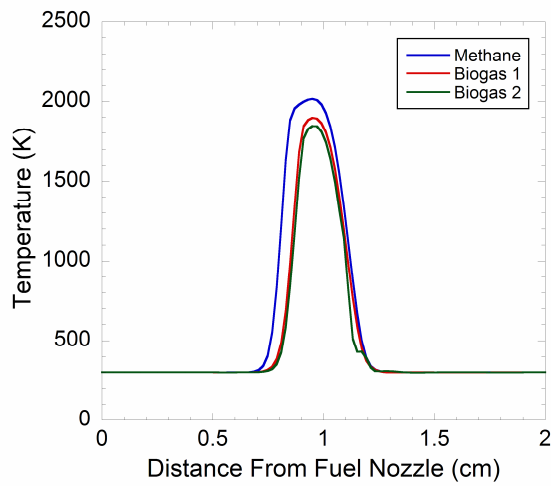


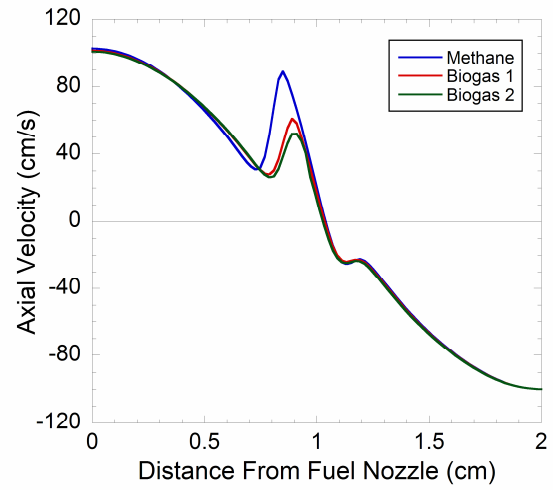
Figure 22. Temperature, axial-velocity, and mole-fraction profiles of main chemical species for methane-air and biogas-air counter-flow flames ($\phi = 3.0$, $T_{inlet} = 300$ K, $P = 1$ atm, $a_s = 150$ s⁻¹).

TABLE V. LOCATION OF PEAK SPECIES MOLE FRACTIONS AND TEMPERATURES IN SIMULATED METHANE-AIR AND BIOGAS-AIR COUNTER-FLOW DIFFUSION FLAMES ($a_s = 150$ s⁻¹ AND $\phi = 3.0$ AT THE FUEL NOZZLE OUTLET).

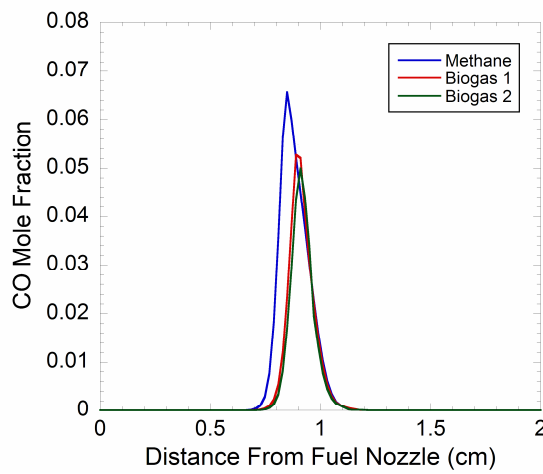
Species	Maximum Mole Fraction	Location of Maximum, x (cm)	Temperature (K)
Methane ($T = T_{max} = 1963.0$ K at $x = 1$ cm)			
H ₂	0.0289	0.9625	1771.4
H ₂ O	0.1616	1	1963.0
CO	0.0530	0.975	1866.2
CO ₂	0.0764	1.025	1924.4
NO	$1.37 \cdot 10^{-4}$	1.0125	1953.3
NO ₂	$4.34 \cdot 10^{-6}$	1.1656	681.2
Biogas 1 ($T = T_{max} = 1878.3$ K at $x = 1$ cm)			
H ₂	0.0202	0.9625	1685.0
H ₂ O	0.1613	0.9938	1874.1
CO	0.0477	0.975	1786.5
CO ₂	0.1044	1.0063	1872.0
NO	$7.73 \cdot 10^{-5}$	1.0125	1859.7
NO ₂	$2.84 \cdot 10^{-6}$	1.1469	743.8
Biogas 2 ($T = T_{max} = 1843.7$ K at $x = 0.9969$ cm)			
H ₂	0.0177	0.9625	1657.7
H ₂ O	0.1604	0.9938	1841.6
CO	0.0452	0.975	1759.4
CO ₂	0.1164	1	1842.8
NO	$5.89 \cdot 10^{-5}$	1.0125	1820.0
NO ₂	$2.40 \cdot 10^{-6}$	1.1469	697.4



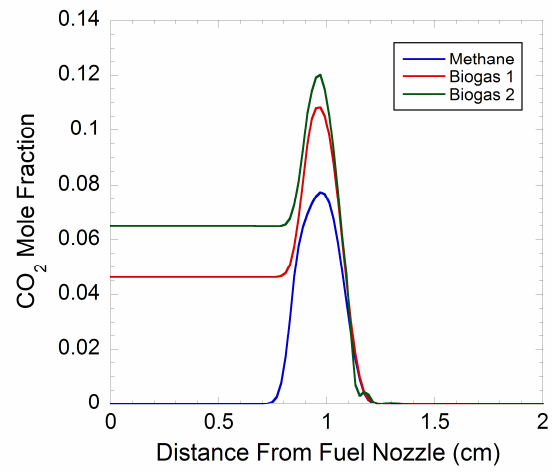
(a)



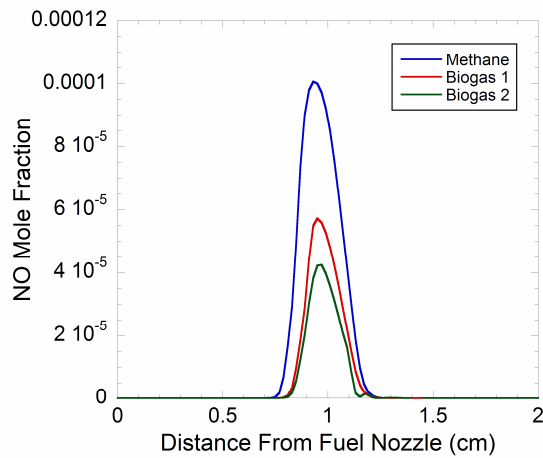
(b)



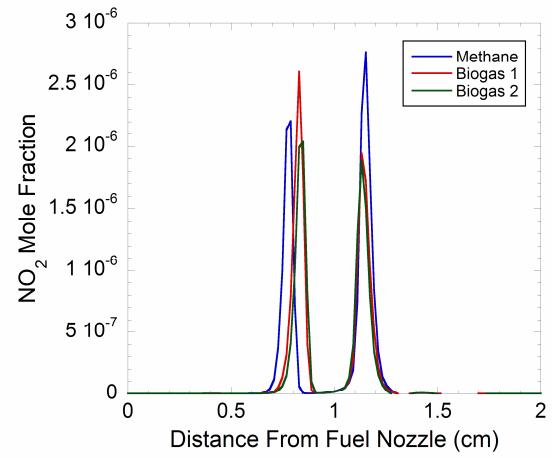
(c)



(d)



(e)



(f)

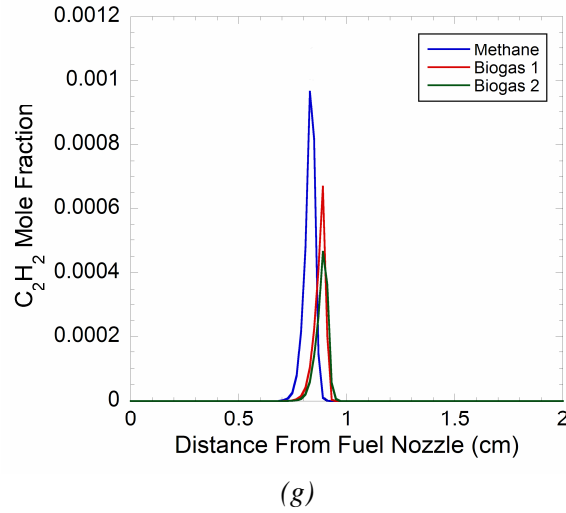
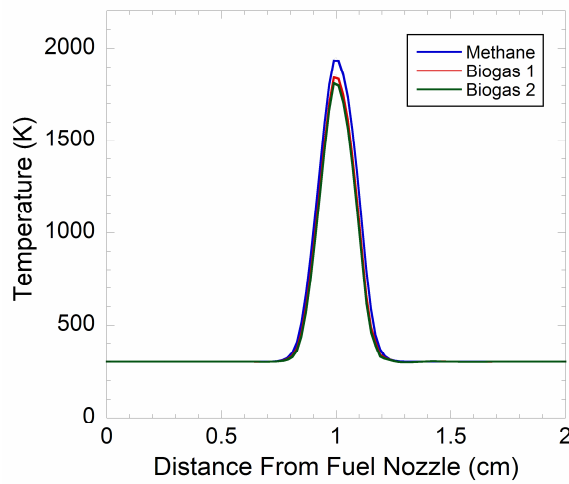


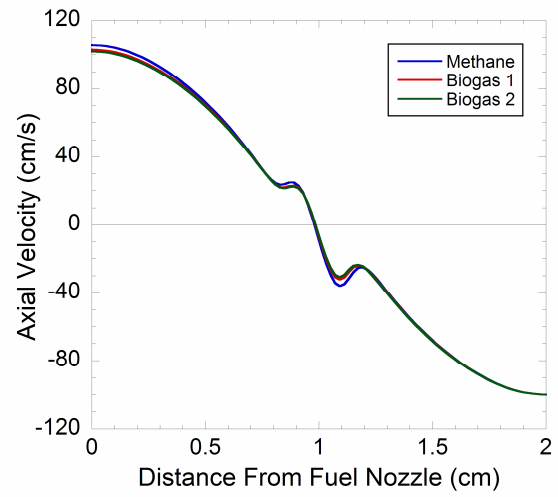
Figure 23. Temperature, axial-velocity, and mole-fraction profiles of main chemical species for methane-air and biogas-air counter-flow flames ($\phi = 1.4$, $T_{inlet} = 300$ K, $P = 1$ atm, $a_s = 200$ s⁻¹).

TABLE VI. LOCATION OF PEAK SPECIES MOLE FRACTIONS AND TEMPERATURES IN SIMULATED METHANE-AIR AND BIOGAS-AIR COUNTER-FLOW DIFFUSION FLAMES ($a_s = 200$ s⁻¹ AND $\phi = 1.4$ AT THE FUEL NOZZLE OUTLET).

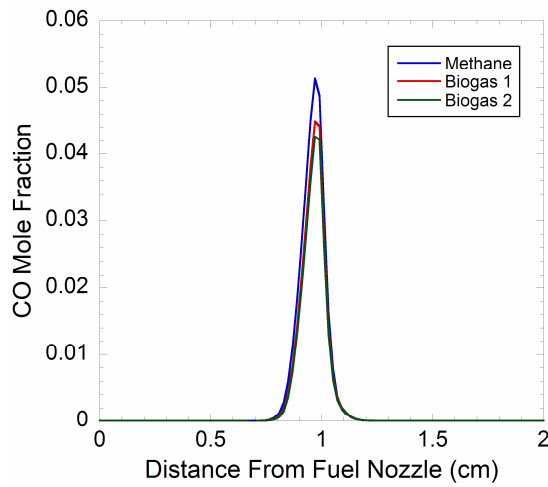
Species	Maximum Mole Fraction	Location of Maximum, x (cm)	Temperature (K)
Methane ($T = T_{max} = 2017.8$ K at $x = 0.95$ cm)			
H ₂	0.0365	0.8344	1732.8
H ₂ O	0.1694	0.8719	1961.9
CO	0.0656	0.8484	1883.0
CO ₂	0.0775	0.975	2005.5
NO	$1.00 \cdot 10^{-4}$	0.925	2009.8
NO ₂	$2.67 \cdot 10^{-6}$	1.1375	812.3
Biogas 1 ($T = T_{max} = 1898.1$ K at $x = 0.95$ cm)			
H ₂	0.0227	0.8859	1638.2
H ₂ O	0.1677	0.9188	1870.7
CO	0.0548	0.9	1795.8
CO ₂	0.1086	0.9625	1897.3
NO	$5.73 \cdot 10^{-5}$	0.95	1898.1
NO ₂	$2.61 \cdot 10^{-6}$	0.8297	703.3
Biogas 2 ($T = T_{max} = 1853.0$ K at $x = 0.95$ cm)			
H ₂	0.0188	0.8953	1618.8
H ₂ O	0.1645	0.925	1831.7
CO	0.0502	0.9063	1745.1
CO ₂	0.1211	0.95	1853.0
NO	$4.34 \cdot 10^{-5}$	0.95	1853.0
NO ₂	$2.25 \cdot 10^{-6}$	0.8391	710.3



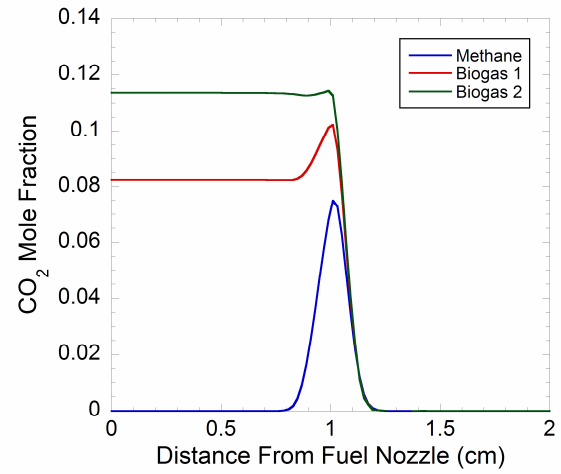
(a)



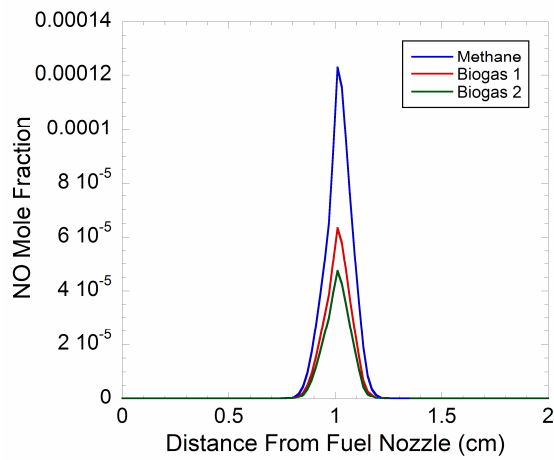
(b)



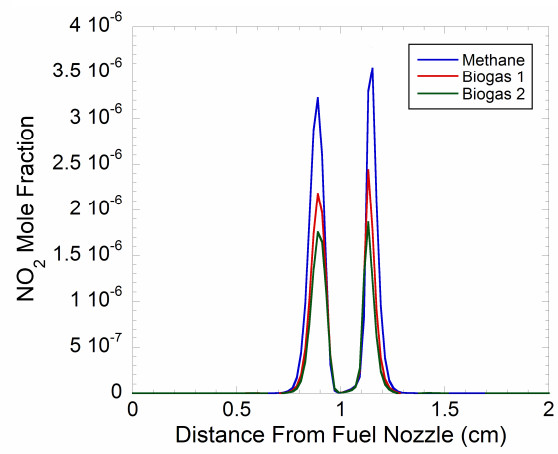
(c)



(d)



(e)



(f)

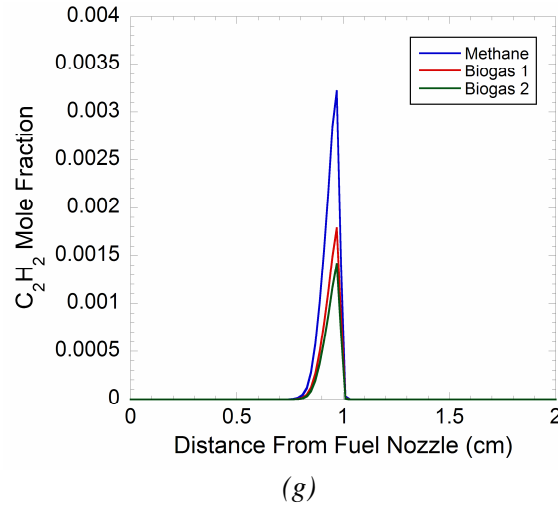


Figure 24. Temperature, axial-velocity, and mole-fraction profiles of main chemical species for methane-air and biogas-air counter-flow flames ($\phi = 3.0$, $T_{inlet} = 300$ K, $P = 1$ atm, $a_s = 200$ s⁻¹).

TABLE VII. LOCATION OF PEAK SPECIES MOLE FRACTIONS AND TEMPERATURES IN SIMULATED METHANE-AIR AND BIOGAS-AIR COUNTER-FLOW DIFFUSION FLAMES ($a_s = 200$ s⁻¹ AND $\phi = 3.0$ AT THE FUEL NOZZLE OUTLET).

Species	Maximum Mole Fraction	Location of Maximum, x (cm)	Temperature (K)
Methane ($T = T_{max} = 1951.5$ K at $x = 1$ cm)			
H ₂	0.0278	0.9625	1733.9
H ₂ O	0.1607	1	1951.5
CO	0.0518	0.975	1847.6
CO ₂	0.0752	1.0188	1908.3
NO	$1.24 \cdot 10^{-4}$	1.0125	1928.6
NO ₂	$3.78 \cdot 10^{-6}$	1.1375	726.6
Biogas 1 ($T = T_{max} = 1858.2$ K at $x = 0.9969$ cm)			
H ₂	0.0194	0.9688	1691.8
H ₂ O	0.1595	0.9938	1854.9
CO	0.0463	0.9813	1798.7
CO ₂	0.1028	1.0031	1853.6
NO	$6.34 \cdot 10^{-5}$	1.0125	1828.4
NO ₂	$2.43 \cdot 10^{-6}$	1.1281	721.0
Biogas 2 ($T = T_{max} = 1824.1$ K at $x = 0.9969$ cm)			
H ₂	0.0170	0.9688	1658.0
H ₂ O	0.1583	0.9938	1821.4
CO	0.0438	0.9844	1785.8
CO ₂	0.1145	0.9969	1824.1
NO	$4.74 \cdot 10^{-5}$	1.0125	1791.0
NO ₂	$1.95 \cdot 10^{-6}$	0.1281	682.3

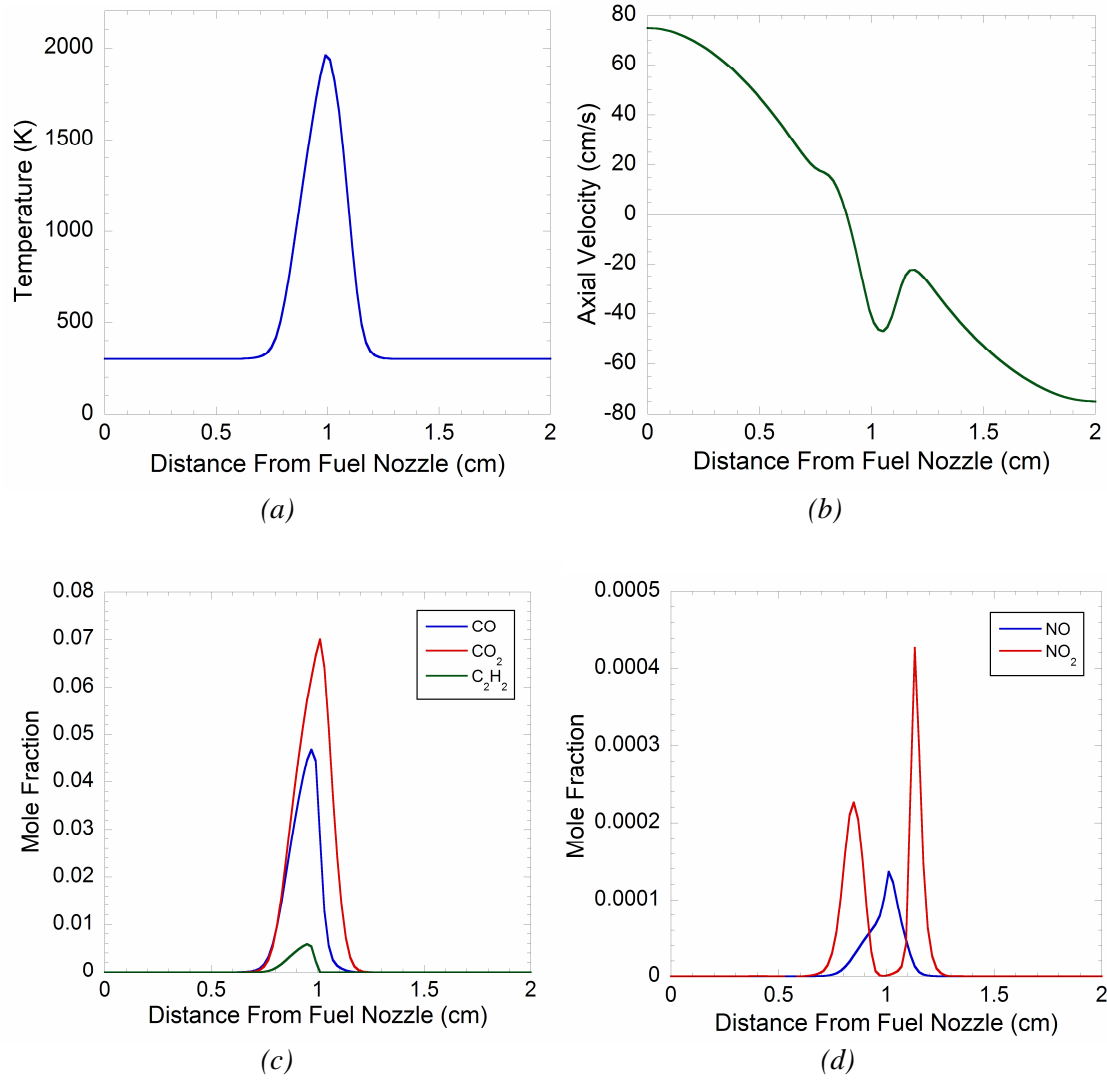


Figure 25. Temperature, axial-velocity, and mole-fraction profiles of main chemical species for methane-air counter-flow flames ($\phi = 10$, $T_{inlet} = 300$ K, $P = 1$ atm, $a_s = 150$ s⁻¹).

TABLE VIII. LOCATION OF PEAK SPECIES MOLE FRACTIONS AND TEMPERATURES IN SIMULATED METHANE-AIR COUNTER-FLOW DIFFUSION FLAMES ($a_s = 150 \text{ s}^{-1}$ AND $\phi = 10$ AT THE FUEL NOZZLE OUTLET).

Species	Maximum Mole Fraction	Location of Maximum, x (cm)	Temperature (K)
<i>Methane ($T = T_{max} = 1971.2 \text{ K at } x = 0.9969 \text{ cm}$)</i>			
H ₂	0.0290	0.9625	1819.0
H ₂ O	0.1671	0.9969	1971.2
CO	0.0469	0.975	1894.3
CO ₂	0.0699	1.0125	1925.3
NO	$1.37 \cdot 10^{-4}$	1.0125	1925.3
NO ₂	$4.25 \cdot 10^{-6}$	1.1281	697.9

4.5.2 Influence of Strain Rate and Equivalence Ratio

Figure 26 shows how the strain rate and the equivalence ratio influence the structure of a methane-air flame. Simulations have been performed for strain rates of 150 s^{-1} and 200 s^{-1} , while equivalence ratio has been set to values of 1.4 and 3.0, respectively. Inlet temperature is set to 300 K for both the fuel and the oxidizer streams. All reported plots show the trend of temperature, axial velocity, and the main species mole-fraction profiles for all combinations listed in Table IX. For what concerns the strain rate, it is easy to state that, as the strain rate increases, the flame becomes narrower, peak temperature decreases, while axial velocity slightly increases. Moreover, emissions of pollutants slightly decrease and the mole-fraction peaks are generally shifted towards the air nozzle.

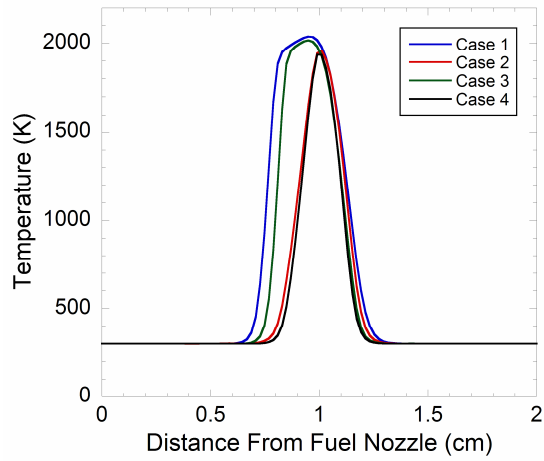
Speaking about the equivalence ratio, we see that for richer mixtures the flame becomes much narrower, peak temperature decreases and is shifted towards the air nozzle, while axial velocity dramatically decreases. Moreover, carbon-dioxide emissions practically do not vary, carbon-monoxide and C₂H₂ emissions dramatically increase and their peaks are shifted towards the air nozzle, while the unburned-fuel fraction beside the air nozzle and nitrogen-oxides production increase a lot.

Furthermore, turning back to Figure 21 through Figure 24, we can state that for richer mixtures the flame structure is almost the same for both biogas and methane for all cases, but biogas still presents much lower C_2H_2 , NO, and NO_2 emissions; carbon-dioxide emissions remain lower for methane, while carbon-monoxide emissions are practically the same for all fuels.

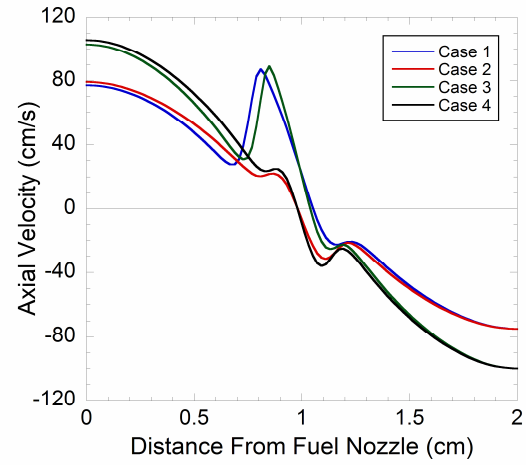
Eventually, turning back to Figure 19, we easily see that for stoichiometric mixtures the flame appears strongly enlarged (even if the peak temperature does not vary) and axial velocity dramatically increases. Also, difference between methane and biogas turns out to be heavier, since axial velocity is almost doubled for methane and temperature is much higher.

TABLE IX. LIST OF COMBINATIONS FOR THE PRESENT COMPUTATION.

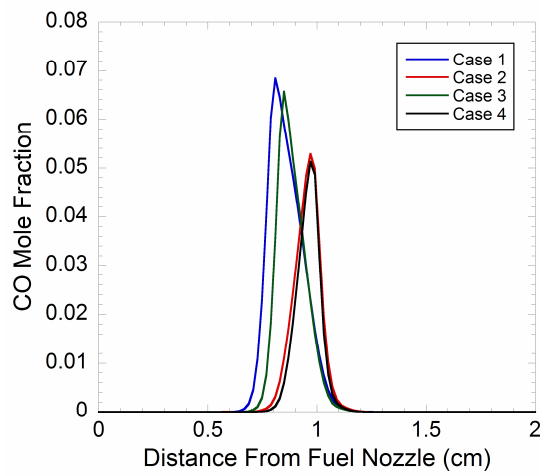
Case	Strain Rate	Equivalence Ratio at the Fuel Nozzle
1	150 s^{-1}	1.4
2	150 s^{-1}	3.0
3	200 s^{-1}	1.4
4	200 s^{-1}	3.0



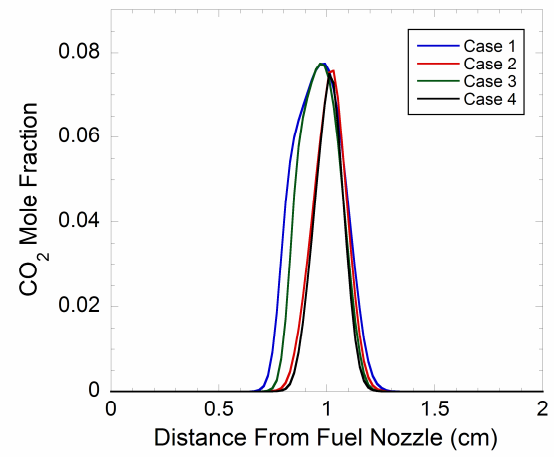
(a)



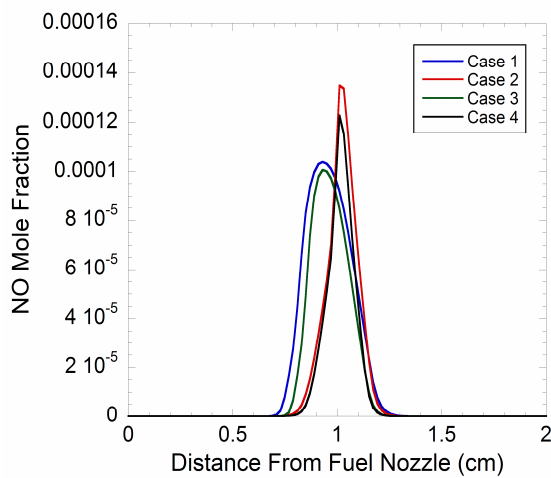
(b)



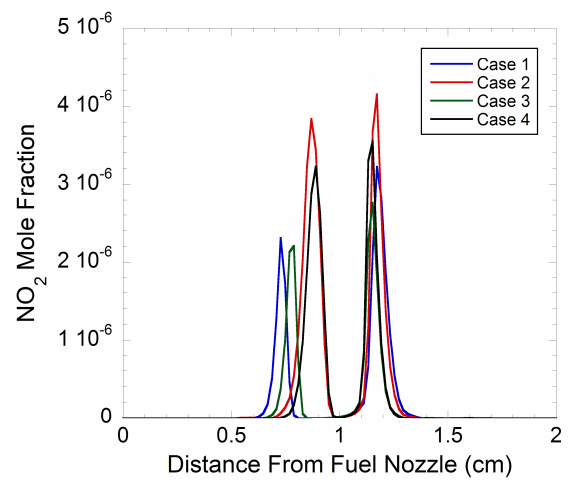
(c)



(d)



(e)



(f)

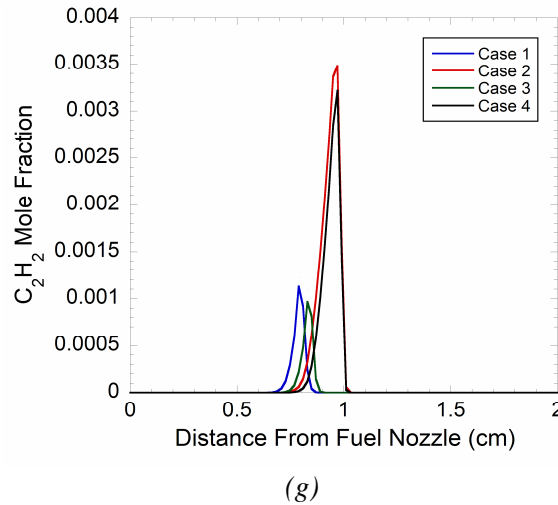


Figure 26. Effect of strain-rate and equivalence-ratio variations on methane-air counter-flow flames for all considered cases ($T_{inlet} = 300$ K, $P = 1$ atm).

4.5.3 Extraction of Stretched Flame Speed

A flame speed for the premixed zone of a partially premixed flame can be extracted by analyzing the peak of carbon-monoxide emissions for each fuel. In particular, the axial-velocity values in correspondence of the latter emission peaks are taken to be the flame speed. Figure 27 shows the peaks of carbon-monoxide emissions for all fuels, when equivalence ratio is set to unity and the strain rate is 150 s^{-1} . Pressure is set to 1 atm, distance between the nozzles is 2 cm, while temperature for both inlet streams is set to 298 K in order to make a comparison with respect to the laminar-premixed-flame case made in the previous chapter. Then Figure 28 presents the extracted flame-speed values for all fuels, clearly showing a relatively light flame-speed increase (around 15% for all fuels) if compared to Figure 6.

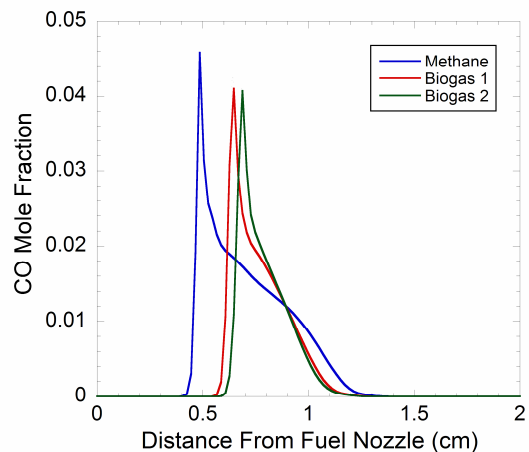


Figure 27. Carbon-monoxide-emission profiles for methane-air and biogas-air counter-flow flames ($\phi = 1$, $T_{inlet} = 298$ K, $P = 1$ atm, $a_s = 150$ s⁻¹).

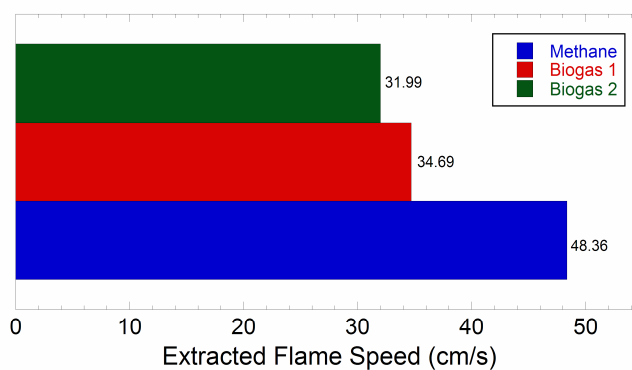
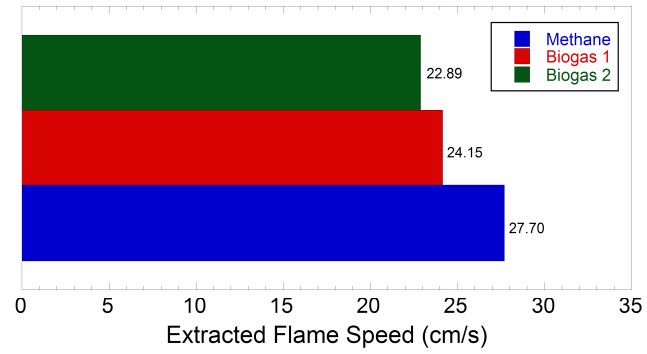


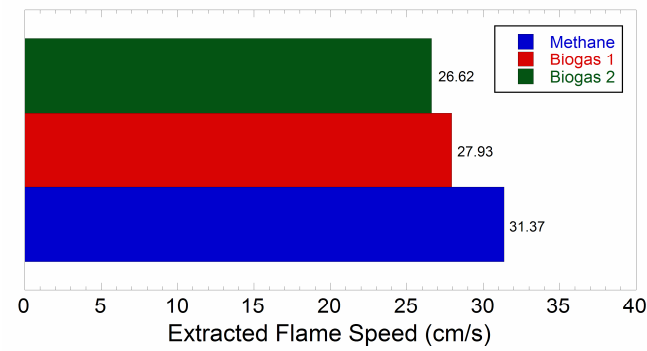
Figure 28. Extracted flame speed for methane-air and biogas-air counter-flow flames ($\phi = 1$, $T_{inlet} = 298$ K, $P = 1$ atm, $a_s = 150$ s⁻¹).

Figure 29 shows how equivalence ratio and the strain rate can influence the extracted flame speed. Simulations have been performed with conditions set as above, when equivalence ratio is 1.4 and the strain rate is 150 s⁻¹ or 200 s⁻¹, and when equivalence ratio is 3.0 and the strain rate is 150 s⁻¹. We can easily see that extracted flame speed presents considerably lower values as the equivalence ratio is increased and relatively higher values as the strain rate is increased. The latter

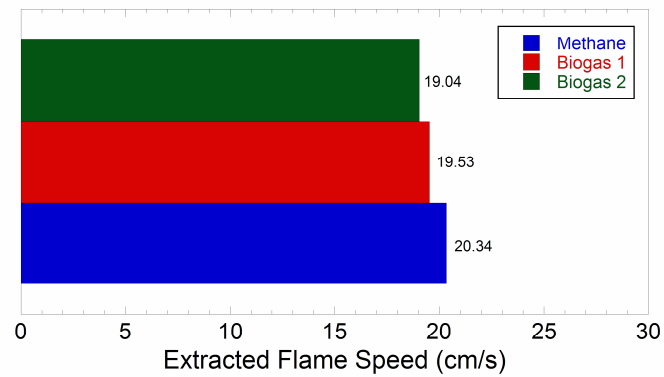
effect is simply due to the fact that the air and the fuel stream velocity is increased and thus the outlet velocity in the premixed zone can be slightly higher. Generally, flame speed should decrease because of the reduction of residence time, but we must say that the flame speed extrapolation may depend much on the chosen number of grid points in the simulation and cannot thus be precisely defined.



(a)



(b)



(c)

Figure 29. Influence of strain rate ($a_s = 150 \text{ s}^{-1}$ for *a* and *c*, $a_s = 200 \text{ s}^{-1}$ for *b*) and equivalence ratio ($\phi = 1.4$ for *a* and *b*, $\phi = 3$ for *c*) on extracted flame speed for methane-air and biogas-air counter-flow flames ($T_{inlet} = 298 \text{ K}$, $P = 1 \text{ atm}$).

4.5.4 Performance Outline

It is well-known that the burning velocity and the heat generation of a particular fuel may be two important parameters in order to evaluate the performance of a combustion process involving that fuel. Table X presents the peak heat fluxes (in W/cm^2) for all PPF cases listed in Table IX and analyzed above. For slightly rich mixtures, methane shows a considerably higher heat production, with biogas 1 and 2 losing 22-24% and 28-30% of heat generation, respectively, while, when considering largely rich mixtures, biogas seems to provide a better heat production (losses to methane become 9-10% and 13-14%, respectively), with biogas 1 being more effective than biogas 2 again. Also, it looks clear that higher strain rates lead to a generally higher heat generation. From the previous considerations, it is easy to state that biogas can represent an important alternative to methane for PPF combustion processes involving rich mixtures when premixing air is supplied at the fuel inlet, since biogas is capable to guarantee lower emissions of pollutants and to provide a reasonably high heat production at the same time.

TABLE X. PEAK HEAT FLUXES IN W/cm^2 FOR METHANE-AIR AND BIOGAS-AIR COUNTER-FLOW FLAMES.

Case	Methane	Biogas 1	Biogas 2
1	51.26	38.87	35.82
2	31.96	28.84	27.72
3	54.78	42.51	39.21
4	36.11	32.44	31.23

4.5.5 Dilution Study

The following paragraph is aimed to give a short account of carbon-dioxide and nitrogen dilution for all considered fuels, and to underline how the strain rate can modify dilution curves. In particular, this study has been conducted for both biogas and methane using an equivalence

ratio of 1.4 and strain rates of 150 s^{-1} and 200 s^{-1} , respectively. Pressure is 1 atm, distance between the nozzles is 2 cm, and temperature for both inlet streams is 300 K. Figure 30 shows carbon-dioxide dilution curves when dilution is carried out in both the fuel and the air stream. In particular, peak temperature is reported as a function of carbon-dioxide mole fraction in the chosen stream. For fuel stream dilution, the stagnation point shows considerable differences depending upon the carbon-dioxide content (on a mole-fraction base it occurs at 0.18% of carbon dioxide for methane, 0.14% for biogas 1, and 0.12% for biogas 2, respectively). Maxima temperatures are constantly higher for biogas, while they present much closer values in correspondence of the stagnation point. For air stream dilution, the stagnation point occurs at 0.43% of carbon dioxide for methane, 0.33% for biogas 1, and 0.29% for biogas 2, with peak temperature being considerably lower for biogas as we approach the stagnation point itself. In general, the more the content of methane in the fuel is the more carbon dioxide is needed for extinction. Moreover, biogas containing less methane contains more carbon dioxide in its initial composition and this may somehow help extinction indeed.

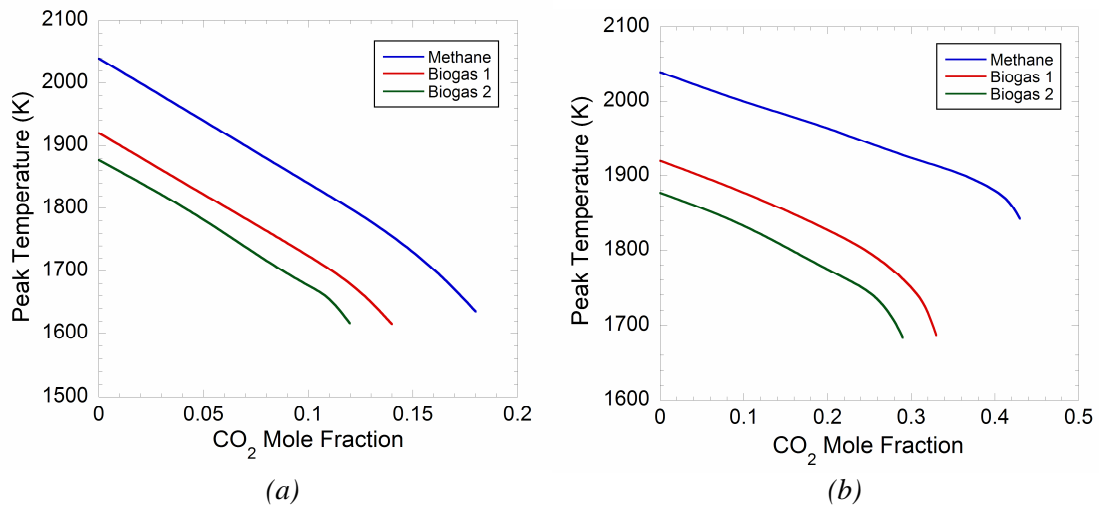


Figure 30. Carbon-dioxide-dilution curves for both the fuel-stream-dilution (a) and the air-stream-dilution (b) case for all considered fuels ($\phi = 1.4$, $T_{inlet} = 300 \text{ K}$, $P = 1 \text{ atm}$, $a_s = 150 \text{ s}^{-1}$).

Figure 31 shows how the strain rate may influence dilution curves for the methane case, when dilution is applied to the fuel stream. The curve is shifted down and the stagnation point moves to the left. Peak temperatures are reasonably higher as the strain rate gets lower, however, temperature is higher in correspondence of the stagnation point for the 200-s⁻¹-case, while carbon-dioxide needed for extinction decreases for the same case.

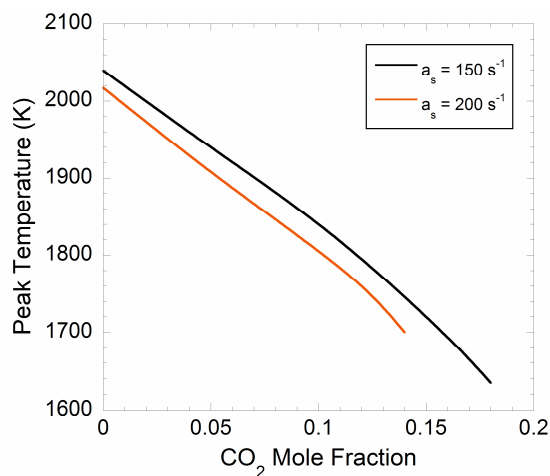


Figure 31. Influence of strain rate on carbon-dioxide-dilution curves for the fuel-stream-dilution case when burning methane ($\phi = 1.4$, $T_{inlet} = 300$ K, $P = 1$ atm).

Figure 32 shows nitrogen dilution curves when dilution is carried out in both the fuel and the air stream. Conditions are the same as above. Generally, for nitrogen dilution we can make the same considerations as in the previous case, since the trend of all curves is practically the same. For fuel stream dilution, the stagnation point occurs at 0.29% of nitrogen for methane, 0.22% for biogas 1, and 0.19% for biogas 2, respectively. For air stream dilution, it occurs at 0.59%, 0.47% , and 0.41% of nitrogen, respectively. Considerations about peak temperatures remain valid for both the carbon-dioxide and the nitrogen dilution cases, with the two biogas curves being one close to the other, and relatively far away from the methane curve.

In general, the amount of nitrogen (in terms of mole fraction) needed for extinction is much higher than that of carbon-dioxide. This is partly due to the carbonaceous nature of methane and to the presence of carbon-dioxide itself in biogas initial composition.

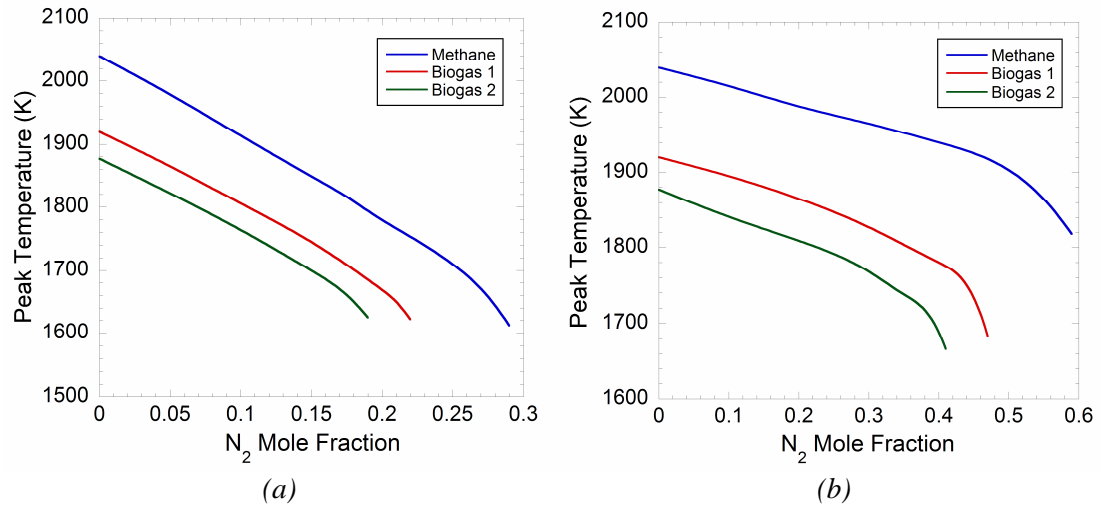


Figure 32. Nitrogen-dilution curves for both the fuel-stream-dilution (a) and the air-stream-dilution (b) case for all considered fuels ($\phi = 1.4$, $T_{inlet} = 300$ K, $P = 1$ atm, $a_s = 150$ s⁻¹).

Figure 33 shows again how the strain rate may influence dilution curves for the methane case, when nitrogen dilution is applied to the fuel stream. Considerations are the same as above for Figure 31.

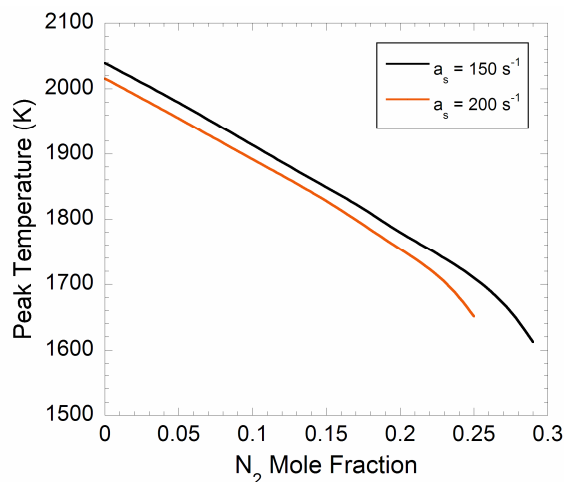


Figure 33. Influence of strain rate on nitrogen-dilution curves for the fuel-stream-dilution case when burning methane ($\phi = 1.4$, $T_{inlet} = 300 \text{ K}$, $P = 1 \text{ atm}$).

4.5.6 Validation and Further Research

As we said before in this work, the aim of this study is mainly to give a general overview on biogas properties by exploiting simulation resources, since biogas may be considered to be one of the most important and efficient *green fuels* available at the moment, and an alternative to methane use. In this sense, simulation can easily help designers understand the fundamental properties of alternative fuels by reducing costs and setup time. Further research could focus on the build-up of an experimental setup, in order to add validation data to the present work. Literature research already contains several experimental investigations about partially premixed flames, and validation studies have been made so far for methane for different *CHEMKIN* mechanism files^[32].

CHAPTER 5

SOFC MODELING AND EXPERIMENTAL SETUP

5.1 Introduction

Solid oxide fuel cells (SOFCs) present a low-pollution technology to generate electricity at high efficiencies^{[44]-[50]}. These fuel cells provide many advantages over traditional energy conversion systems including high efficiency, high kinetics of both chemical and electrochemical reactants, reliability, modularity, fuel adaptability, lack of precious catalysts, and very low levels of polluting emissions.

SOFCs were first being developed for operating primarily in the temperature range of 900 to 1000°C. In addition to the capability of internally reforming hydrocarbon fuels (for instance, methane and natural gas), such high temperature fuel cells provide high quality exhaust heat for cogeneration. However, reduction of the SOFC operating temperature by 200°C or more allows the use of a broader set of materials, is less demanding on the seals and balance-of-plant components, simplifies thermal management, aids in faster start-up and cool-down, and results in less degradation of cell and stack components. Because of these advantages, the development of SOFCs capable of operating in the temperature range of 650 to 800°C has increased dramatically in the last years. However, at lower temperatures, electrolyte conductivity and electrode kinetics decrease significantly; in order to face these significant drawbacks, alternative cell materials and designs are being extensively investigated.

An SOFC essentially consists of two porous electrodes separated by a dense, oxide ion conducting electrolyte. The operating principle of such a cell is illustrated in Figure 34. Oxygen is supplied at the cathode and reacts with incoming electrons from the external circuit to form oxide ions, which migrate to the anode through the oxide ion conducting electrolyte. At the anode, oxide ions combine with hydrogen (and carbon monoxide) in the fuel to form water (and carbon

dioxide), liberating electrons. Electrons (and thus electricity) flow from the anode through the external circuit to the cathode.

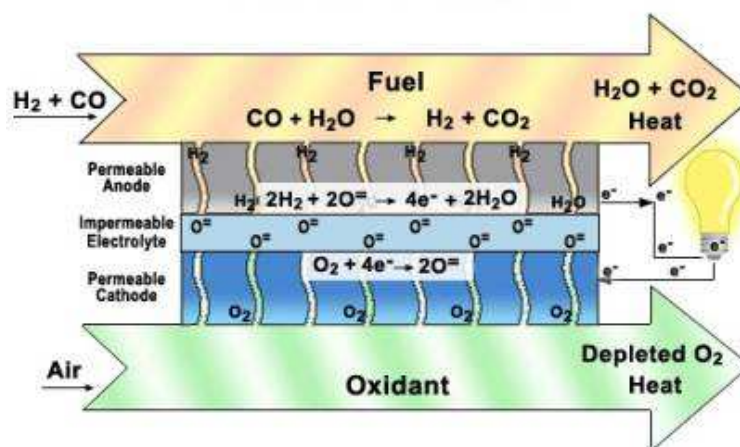


Figure 34. Operating principle of a solid oxide fuel cell.

The materials for the cell components are selected by focusing on suitable electrical conducting properties required for these components to perform their intended cell functions, i.e. adequate chemical and structural stability at high temperatures encountered during cell operation as well as during cell fabrication, minimal reactivity and diffusion among different components, and matching thermal expansion among different components.

5.1.1 Electrolyte

Yttria-stabilized zirconia (YSZ) remains the most widely used material for the electrolyte in SOFCs because of its relatively high ionic conductivity, chemical stability, and mechanical strength. The only drawback of YSZ is the low ionic conductivity encountered in the lower cell operation temperature regime (below about 750°C). Two solutions employed to solve this problem are to decrease the thickness of the YSZ electrolyte and to find other materials to replace yttrium. Scandium-doped zirconium oxide has higher conductivity than YSZ but presents high

costs and detrimental ageing effects. Also, gadolinium-doped or samarium-doped cerium oxide materials possess higher oxide ion conductivity compared to zirconium based materials; however, cerium oxide based materials, under reducing conditions at high temperatures, exhibit significant electronic conductivity and dimensional change. Since operation at temperatures below 600°C overcomes this problem, cerium oxide based materials are successfully being used as electrolyte in SOFCs by Ceres Power Limited (UK). Also, other mixed oxides provide an opportunity to develop oxide ion conducting electrolytes; in fact, a mixture containing gallium oxide has lately attracted attention as an electrolyte, even though it presents two drawbacks (uncertain cost of gallium, and uncertain chemical and mechanical stability of the oxide). Despite the latter problems, Mitsubishi Materials Corporation (Japan) is using this as the electrolyte in its SOFCs and has successfully built and tested up to 10-kW size SOFC power systems.

5.1.2 Cathode

The oxidant gas is represented by air (or oxygen) at an SOFC cathode, and the electrochemical reduction of oxygen requires a series of elementary reactions involving the transfer of multiple electrons. Because of this fact, an SOFC cathode must meet the requirements of high catalytic activity for oxygen reduction, high electronic conductivity, chemical and dimensional stability in environments encountered during cell fabrication and cell operation, thermal expansion match with other cell components, and compatibility and minimum reactivity with the electrolyte and the interconnection. Finally, the cathode must have a stable, porous microstructure so that gaseous oxygen can readily diffuse through the cathode to the cathode-electrolyte interface. These stringent electrochemical and mechanical requirements greatly restrict the number of suitable candidate materials. In general, lanthanum manganite, when doped with calcium or strontium, has good electronic conduction and possesses adequate electrocatalytic activity, a reasonable thermal expansion match to YSZ, and stability in the SOFC cathode operating environment.

For SOFCs operating at substantially lower temperatures, such as 650 to 800°C, alternative cathode materials, typically containing transition metals such as cobalt, iron, and nickel, have been developed and optimized for better performance. In general, these materials offer higher oxide ion diffusion rates and faster oxygen reduction kinetics at the cathode-electrolyte interface (if compared with lanthanum manganite). However, thermal expansion coefficients and electrical conductivities of these materials can sometimes have a strongly negative effect on performance. Nevertheless, good results have been reported using these materials, though in many cases the improved cathodic performance is found to decrease during the cell lifetime as a result of chemical instability. Minimization of cathodic polarization losses is one of the biggest challenges to be overcome for obtaining high, stable power densities from lower temperature SOFCs. Therefore, a thin layer, generally made of a cerium oxide based material, is used to reduce the chemical reactivity of the cathode toward YSZ. It has been also shown that polarization resistance depends on the grain size of the ionic conductor in the electrode and on porosity.

5.1.3 Anode

The anode of an SOFC must be an excellent catalyst for fuel oxidation, stable in the reducing environment of the fuel, electronically conducting, and must have sufficient porosity to allow the transport of the fuel to and the transport of the products of fuel oxidation away from the electrolyte-anode interface where the fuel oxidation reaction takes place. Other requirements include matching of its thermal expansion coefficient with that of the electrolyte and interconnect, integrity of porosity for gas permeation, chemical stability with the electrolyte and interconnect, and applicability to use with versatile fuels and impurities. In addition, cost effectiveness plays always an important role for commercialization.

Nickel-YSZ composites are the most commonly used anode materials for SOFCs, since nickel is an excellent catalyst for fuel oxidation. However, nickel possesses a high thermal expansion coefficient, and exhibits coarsening of microstructure due to metal aggregation through grain growth at cell operation temperatures. YSZ in the anode constrains nickel aggregation and

prevents sintering of nickel particles, decreases the effective thermal expansion coefficient bringing it closer to that of the electrolyte, and provides better adhesion of the anode with the electrolyte. In these anodes, nickel has dual roles of the catalyst for hydrogen oxidation and the electrical current conductor. In addition, it is also highly active for steam reforming of methane (this catalytic property is largely exploited in the so-called internal reforming SOFCs that can operate on fuels composed of mixtures of methane). Although nickel is an excellent hydrogen oxidation and methane-steam reforming catalyst, it also catalyzes the formation of carbon from hydrocarbons under reducing conditions and, unless sufficient amounts of steam are present along with the hydrocarbon to remove carbon from the nickel surface, the anode may be destroyed. As a result, even when using methane as the fuel, relatively high steam-to-carbon ratios are needed to suppress this deleterious reaction. Unfortunately, this approach does not work for higher hydrocarbons, and it is generally not possible to operate nickel-based anodes on higher hydrocarbon-containing fuels without pre-reforming. In spite of this drawback, nickel-YSZ composite remains the most commonly used anode material for SOFCs and is satisfactory for cells operating on clean and reformed fuel.

However, advanced SOFC designs place additional constraints on the anode, such as the ability to tolerate significant quantities of sulphur and hydrocarbon species in the fuel stream. Alternative materials, such as cerium oxide and strontium titanate/cerium oxide mixtures, have yielded some promising results in these designs, but the benefits obtained are counterbalanced by other limitations. Copper based anodes have also been proposed for intermediate temperature (less than 800°C) SOFCs intended to operate directly on hydrocarbon fuels without prior reformation, without leading to significant achievements though.

5.1.4 Interconnect

Since a single cell only produces voltage less than 1 V and power around 1 W/cm², many cells are electrically connected together in a cell stack to obtain higher voltage and power. To

connect multiple cells together, an interconnection is used in SOFC stacks. The requirements of the interconnection are the most severe of all cell components and include:

- nearly 100% electronic conductivity;
- stability in both oxidizing and reducing atmospheres at the cell operating temperature since it is exposed to air (or oxygen) on the cathode side and to the fuel on the anode side;
- low permeability for oxygen and hydrogen to minimize direct combination of oxidant and fuel during cell operation;
- a thermal expansion coefficient close to that of the cathode and the electrolyte,
- non-reactivity with other cell materials;
- manufacturability.

To satisfy these requirements, doped lanthanum chromite is used as the interconnection for cells intended for operation at about 1000°C. In cells intended for operation at lower temperatures (less than 800°C), it is possible to use oxidation-resistant metallic materials for the interconnection, such as metallic alloys that offer improved manufacturability, significantly lower raw material and fabrication costs, and higher electrical and thermal conductivity. However, in order to be useful for the interconnect application, the metallic alloys must satisfy additional requirements, including resistance to surface oxidation and corrosion in a dual atmosphere (simultaneous exposure to oxidizing and reducing atmospheres), thermal expansion matching to other stack components (particularly for stacks using a rigid seal design), chemical compatibility with other materials in contact with the interconnect, such as seals and cell materials, high electrical conductivity not only through the bulk material but also in in-situ-formed oxide scales, and mechanical reliability and durability at the cell operating temperature. Ferritic stainless steels are the most promising candidates, owing to the fact that some alloys in this family offer ease of manufacturing and low cost. Several new ferritic stainless steels have been developed specifically for SOFC interconnects and, although these alloys demonstrate improved performance over

traditional compositions, several critical issues remain (poisoning of cathodes, corrosion and spalling under interconnect exposure conditions, and compatibility with the adjacent components such as electrical contact layers). To overcome some of these problems, some surface coatings can be applied onto metallic interconnects.

5.1.5 Stack Design

In terms of stack design, most development has focused on planar and tubular design cells, each of these designs having a number of interesting variants; for instance, the planar SOFC may be in the form of a circular disk fed with fuel from the central axis, or it may be in the form of a square plate fed from the edges, while the tubular SOFC may be of a large diameter (more than 15 mm), or of much smaller diameter (less than 5 mm), representing the so-called microtubular cells. Also, the tubes may be flat and joined together to give higher power density and easily printable surfaces for depositing the electrode layers. Figure 35 illustrates typical planar cell stacks and a tubular cell bundle (this latter presents the advantage that the air and the fuel are naturally isolated because the tubes are closed at one end).



Figure 35. Illustration of planar cell stacks (top) and a tubular cell bundle (bottom).

In the case of planar cell stacks, an effective seal must be provided to isolate air from the fuel. The seal must have a thermal expansion match to the fuel cell components, must be electrically insulating and must be chemically stable under the operational conditions of the stack. Also, it should exhibit no deleterious interfacial reactions with other cell components, should be stable under both the high temperature oxidizing and reducing operational conditions, should be created at a low enough temperature to avoid damaging cell components (below 850°C for some materials), and should not migrate or flow from the designated sealing region during sealing or

cell operation. In addition, the sealing system should be able to withstand thermal cycling between the cell operation temperature and room temperature. A number of different sealing approaches are under development, including rigid, bonded seals (glass-ceramics and brazes), compliant seals (viscous glasses), and compressive seals (mica-based composites). Successful development of sealing materials and concepts for planar SOFCs is probably the most important issue for the long-term performance stability and lifetime of planar SOFC stacks and hence for their eventual commercialization at competitive costs.

The single biggest advantage of tubular cells over planar cells is that they do not require any high temperature seals to isolate oxidant from the fuel, and this makes performance of tubular cell stacks very stable over long periods of times (several years). However, their areal power density is much lower (about 0.2 W/cm^2) if compared to planar cells (up to 2 W/cm^2 for single cells and at least 0.5 W/cm^2 for stacks), performances are thus relatively low (because of the longer electronic pathways and the higher Ohmic losses), and manufacturing costs are higher. To increase the power density and reduce the physical size and cost of tubular SOFC stacks, alternative tubular geometry cells, as illustrated in Figure 36, were under development by Siemens. Such alternative geometry cells combine all the advantages of the tubular SOFCs while providing higher areal power densities. The performance of these new design cells is already higher than that of cylindrical tubular cells, but still lower than that of anode-supported planar cells^{[44]-[50]}.

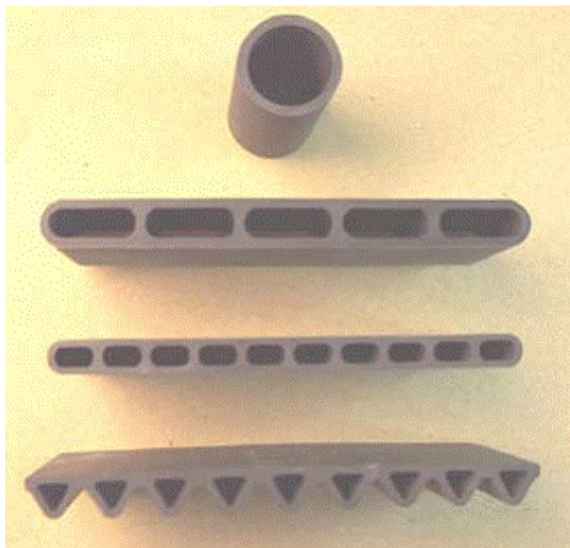


Figure 36. Alternative tubular geometry cells being developed by Siemens.

5.2 SOFC Modeling

The second part of this study has been developed by using *MATLAB R2009a* together with *Cantera 1.6* in order to build up a numerical model for a tubular solid-oxide fuel cell and by validating the same model through a series of experimental tests. For what concerns the numerical simulation behind the model, on one hand, *MATLAB* is a high-level technical computing language and interactive environment for algorithm development, data visualization, data analysis, and numerical computation, that allows the user to solve technical computing problems faster than with traditional programming languages; on the other hand, *Cantera* is a collection of object-oriented software tools (which can be directly interfaced with *MATLAB*) for problems involving chemical kinetics, thermodynamics, and transport processes. Among other things, *Cantera* can be used to conduct kinetics simulations with large reaction mechanisms, to compute chemical equilibrium, to evaluate thermodynamic and transport properties of mixtures, to evaluate species chemical production rates, to conduct reaction path analysis, to create process simulators using networks of stirred reactors, and to model non-ideal fluids. For what concerns

the experimental validation, all tests have been performed on a commercial anode-supported tubular SOFC at *Edison S.p.a. - Centro Ricerca e Sviluppo* in Trofarello, Torino (Italy).

5.2.1 Governing Equations

Although much of the modeling approach described here can be used with any SOFC configuration, we focus in this work on the specific tubular cell configuration. This paragraph aims to be a description of the equations employed by *Cantera* for implementing the present model.

First, since *Cantera* was initially born to study combustion processes and flames, we must follow the so-called *similarity solution* approach (that is the solving process generally used for flames and based on converting a system into a certain number of cylindrical elements where one-dimensional laws can be applied). By doing so, we must consider the following limits:

$$\frac{L}{D} \ll 1, \quad (54)$$

$$Ma \ll 1, \quad (55)$$

where L and D represent respectively the length and the diameter of a cylindrical element obtained from the discretization of the reacting environment, and Ma is the Mach number. Having a low Mach number basically means that pressure is nearly constant. If these limits and the boundary conditions are satisfied, the exact flow equations admit a solution with the following properties:

$$u = u(z), \quad (56)$$

$$v = rV(z), \quad (57)$$

$$T = T(z), \quad (58)$$

$$Y_k = Y_k(z), \quad (59)$$

$$P = P_0 + \Lambda \frac{r^2}{2}, \quad (60)$$

where z is the axial coordinate (following the direction of the cylinder axis), u is the axial velocity of the flow entering the cylinder, r is the radial coordinate (following the direction of the cylinder radius), v is the radial velocity of the flow, V is the normalized radial velocity, T is temperature, Y_k is the mass fraction of the k th chemical species, P is pressure, P_0 is the reference pressure, and Λ is a constant that must be determined as part of the solution. Boundary conditions are set at $z = 0$ and $z = L$, with u , T , and Y_k being independent of r , and with v being linear in r (v is usually set to zero at the boundaries).

For conditions where the similarity solution holds, the flow equations reduce to a set of ordinary differential equations in the axial coordinate z . This is possible because the gas flow in the fuel channel is considered to be one-dimensional and laminar, neglecting variations of the gas composition transverse to the flow direction. This is a good approximation, because the fuel channel typically has characteristic diameters less than a centimeter and mean velocities of less than 100 cm/s. Under these circumstances, the Reynolds number is on the order of 100 or less. The following equations represent the set of ODEs employed to solve the problem in the axial coordinate:

- *Continuity:*

$$\frac{d}{dz}(\rho u) + 2\rho V = 0, \quad (61)$$

- *Radial Momentum:*

$$\rho \frac{dV}{dz} = \frac{d}{dz} \left(\mu \frac{dV}{dz} \right) - \Lambda - \rho u \frac{dV}{dz} - \rho V^2, \quad (62)$$

- *Species Conservation:*

$$\rho \frac{dY_k}{dz} = -\rho u \frac{dY_k}{dz} - \frac{dJ_k}{dz} + W_k \dot{\omega}_k, \quad (63)$$

- *Energy Conservation:*

$$\rho c_p \frac{dT}{dz} = -\rho c_p u \frac{dT}{dz} + \frac{d}{dz} \left(\lambda \frac{dT}{dz} \right) - \sum_k W_k \dot{\omega}_k h_k - \sum_k J_k c_{p,k} \frac{dT}{dz}. \quad (64)$$

In these equations ρ , μ , c_p and λ denote respectively the density, the viscosity, the specific heat at constant pressure, and the thermal conductivity of the gas mixture, t indicates time, while J_k , W_k , $\dot{\omega}_k$, h_k , and $c_{p,k}$ represent respectively the flux through the cylindrical element, the molecular weight, the molar net production rate, the enthalpy, and the specific heat at constant pressure of the k th species. The fluxes J_k can be computed using either the mixture-averaged transport model or the multicomponent transport model, as described in paragraphs 3.3.2 and 4.3.1, while the molar production rates $\dot{\omega}_k$ are evaluated using a heterogeneous mechanism (Table XI). Since the mechanism is formulated in terms of elementary reactions on the catalyst surface, the reaction rates depend both on the concentrations of the gaseous reactants and on the coverages of the surface species representing reactive surface sites and adsorbates. Since these coverages are not known a priori, they must be determined as part of the solution.

Unlike the gaseous species, the surface species are effectively immobile on length scales larger than an individual catalyst particle. Therefore, at steady state, the surface coverages must take on values such that the net production rate due to chemistry is zero for every surface species:

$$\dot{\omega}_{surf,k} = 0 \quad k = 1, \dots, K_s, \quad (65)$$

where K_s is the total number of surface species. The net production rate of any species (gas or surface) is given by:

$$\dot{\omega}_k = \sum_i \nu_{k,i} q_i, \quad (66)$$

where q_i is the rate of reaction i and $\nu_{k,i}$ is the net stoichiometric coefficient of the k th species in reaction i (positive for products, negative for reactants). The reaction rates q_i are computed assuming mass-action kinetics, with temperature-dependant rate coefficients in Arrhenius form:

$$k_i = A_i T^n \exp(-E_i / RT), \quad (67)$$

where A_i is the pre-exponential factor and E_i is the activation energy for the reaction i ^[51].

5.2.2 Finite Difference Approach

In order to compute the convective terms, i.e. $\frac{dV}{dz}$, $\frac{dY_k}{dz}$, and $\frac{dT}{dz}$, an upwind differencing method is employed as follows:

- if $u_j > 0$:

$$\left(\frac{df}{dz}\right)_j = \frac{f_j - f_{j-1}}{z_j - z_{j-1}}, \quad (68)$$

- otherwise:

$$\left(\frac{df}{dz}\right)_j = \frac{f_{j+1} - f_j}{z_{j+1} - z_j}. \quad (69)$$

where f indicates the quantity of interest, while a central differencing method, i.e.:

$$\left(\frac{df}{dz}\right)_j = \frac{f_{j+1} - f_{j-1}}{2(z_{j+1} - z_{j-1})}, \quad (70)$$

is employed to compute the diffusive terms, which are $\frac{d}{dz}\left(\mu \frac{dV}{dz}\right)$, $\frac{dJ_k}{dz}$, and $\frac{d}{dz}\left(\lambda \frac{dT}{dz}\right)$.

The continuity equation propagates information in the following right-to-left way:

$$\frac{(\rho u)_{j+1} - (\rho u)_j}{\Delta z_{j+\frac{1}{2}}} + (\rho V)_j + (\rho V)_{j+1} = 0, \quad (71)$$

where ρu is specified on the right by the right-boundary object, while the lambda equation, i.e.:

$$\Lambda_j = \Lambda_{j-1}, \quad (72)$$

propagates information left-to-right, with Λ being specified on the left by the left-boundary object. If the mass flow rate from the left is specified, then the residual equation for Λ on the left is:

$$(\rho u)_0 = \dot{m}_{left}^{[41]}. \quad (73)$$

5.2.3 Electrochemistry

Charge-transfer processes surely represent one of the least well-understood issues of fuel-cell chemistry. Recently, the common objective in fuel-cell research is to describe the whole charge-transfer kinetics in terms of elementary reaction steps, in such a way that parallels the treatment of thermal heterogeneous chemistry^{[10], [11]}. However, it is often satisfactory to retain a Butler-Volmer formalism for the charge-transfer steps, since this kind of approach provides important information about functional dependencies such as the reaction orders in the exchange current density.

The potential difference E_{cell} across the cell can be written as:

$$E_{cell} = E_c - E_a - \eta_{ohm}(i), \quad (74)$$

where the subscripts c and a indicate respectively the cathode and the anode and $\eta_{ohm}(i)$ is the ohmic overpotential. To use equation (74) to compute E_{cell} as a function of the current density, it would be necessary to supply additional equations to compute the potential differences across both the electrodes. For an ideal reversible cell exposed to the same gas environment as the actual cell, we know that:

$$E_{rev} = E_{c,rev} - E_{a,rev}. \quad (75)$$

Subtracting equation (75) from equation (74) and introducing the activation overpotential, for both electrodes we get:

$$\eta_{act} = E - E_{rev}, \quad (76)$$

it is possible to write the following equation:

$$E_{cell} = E_{rev} - \eta_{act,a}(i) - \eta_{ohm}(i) - |\eta_{act,c}(i)|. \quad (77)$$

If the gas compositions at the triple-phase boundary of each electrode are locally in chemical equilibrium, then the reversible potential is well-defined, and may be computed by applying the Nernst equation to any global oxidation reaction. The simplest form in this case is:

$$E_{rev} = -\frac{RT}{4F} \ln \left(\frac{P_{O_2,c}}{P_{O_2,a}} \right), \quad (78)$$

where F is the Faraday constant and P_{O_2} is the partial pressure of oxygen. The equilibrium assumption will generally be very good on the cathode side, but may not hold on the anode side if residual hydrocarbons are still present in the gas in the triple-phase regions. If the gas composition on the anode side is not locally in equilibrium, then the oxidation reaction for each fuel species would give a different cell potential; in this case, we must know something precise about electrochemically active species in order to compute E_{cell} . For instance, we may assume that the hydrogen pathway is dominant, and so we can compute the reversible cell potential by using the Nernst equation for the hydrogen oxidation as follows:

$$E_{rev} = E^0 + \frac{RT}{2F} \ln \left(\frac{P_{H_2,a}}{P_{H_2O,a}} \right) + \frac{RT}{2F} \ln \left(P_{O_2,c}^{\frac{1}{2}} \right), \quad (79)$$

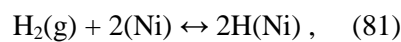
where:

$$E^0 = \frac{1}{2F} \left(\mu_{H_2}^0 + \frac{1}{2} \mu_{O_2}^0 - \mu_{H_2O}^0 \right), \quad (80)$$

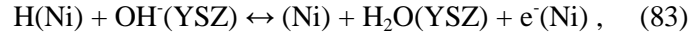
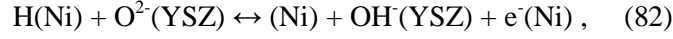
is the ideal standard potential and μ_k^0 are standard-state chemical potentials. As indicated by the subscripts a and c , the gas-phase species partial pressures (measured in atmospheres) in equation (79) are evaluated at both the anode and the cathode.

The charge-transfer activation overpotentials at the electrode-electrolyte interface are computed by inverting Butler-Volmer equations to determine overpotentials as a function of current density. Generally, in developing an expression for the anode activation overpotential in Butler-Volmer form, it is very useful to consider five elementary reactions in Ni-YSZ three-phase region (considering the electrochemical oxidation at the anode to be carried out by hydrogen only), which are the following:

1. Adsorption/desorption on the nickel surface:



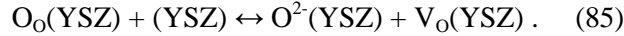
2. Charge-transfer reactions at the TPB region:



3. Adsorption/desorption on the YSZ surface:



4. Transfer of oxygen ions between the surface and the bulk YSZ:



$\text{H}(\text{Ni})$ is an adsorbed atomic hydrogen, (Ni) is an empty surface site, and $\text{e}^-(\text{Ni})$ is an electron within the nickel anode. Within the YSZ electrolyte, $\text{O}_\text{o}(\text{YSZ})$ is a lattice oxygen and $\text{V}_\text{o}(\text{YSZ})$ is an oxygen vacancy. On the YSZ surface there can be three species, which are $\text{O}^{2-}(\text{YSZ})$, $\text{OH}^-(\text{YSZ})$, and $\text{H}_2\text{O}(\text{YSZ})$, and empty sites (YSZ) . The hydrogen adsorption-desorption reaction appears in the thermal heterogeneous chemistry (reactions 1 and 2 in Table XI). Considering the two charge-transfer reactions (reactions 33 and 34), it is useful to assume reaction 34 to be rate-limiting. Consequently, the other four reactions are assumed to be equilibrated. Further, we could assume that the electrolyte surface is nearly fully covered by $\text{O}^{2-}(\text{YSZ})$ ions. Using these assumptions, the current density can be written in the Butler-Volmer form as follows:

$$i = i_0 \left[\exp\left(\frac{(\beta_{34,a} + 1)F\eta_{act,a}}{RT}\right) - \exp\left(-\frac{\beta_{34,c}F\eta_{act,a}}{RT}\right) \right] , \quad (86)$$

where the activation overpotential can be also written as:

$$\eta_{act,a} = E_a - E_a^{eq} , \quad (87)$$

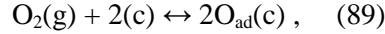
and the exchange current density is given as:

$$i_0 = i_{H_2}^* \frac{\left(\frac{P_{H_2}}{P_{H_2}^*}\right)^{\frac{1}{4}} (P_{H_2O})^{\frac{3}{4}}}{1 + \left(\frac{P_{H_2}}{P_{H_2}^*}\right)^{\frac{1}{2}}} . \quad (88)$$

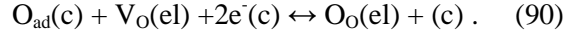
The electric-potential difference between the anode and the electrolyte is E_a , and the equilibrium electric-potential difference E_a^{eq} is the electric-potential difference at which there is no net current flow. Note that the apparent symmetry factor in the anodic direction is $\beta_{34,a} + 1$. As discussed in prior literature, this shift in symmetry factor occurs where there are multiple charge-transfer steps, with one being rate-limiting. The quantity $P_{H_2}^*$ is determined from the balance between adsorption and desorption of hydrogen on nickel, while the parameter $i_{H_2}^*$ is usually taken as an empirical constant.

As with oxidation at the anode, the global oxygen reduction at the electrode-electrolyte interface is assumed to proceed in two steps:

1. Adsorption/desorption:



2. Charge transfer at the TPB:



In these reactions $O_{ad}(c)$ is adsorbed atomic oxygen on the cathode surface, (c) is an unoccupied cathode surface site, $V_O(el)$ is an oxygen vacancy, $e^-(c)$ is an electron within the cathode, and $O_O(el)$ denotes a lattice oxygen ion in the bulk of the electrolyte. The charge-transfer step is assumed to be rate-limiting. The current density can be expressed as follows:

$$i = i_0 \left[\exp\left(\frac{\beta_{44,c} F \eta_{act,c}}{RT}\right) - \exp\left(-\frac{\beta_{44,c} F \eta_{act,c}}{RT}\right) \right], \quad (91)$$

where the cathode activation overpotential can be also written as:

$$\eta_{act,c} = E_c - E_c^{eq}. \quad (92)$$

The exchange current density can be represented as:

$$i_0 = i_{O_2}^* \frac{\left(\frac{P_{O_2}}{P_{O_2}^*}\right)^{\frac{1}{4}}}{1 + \left(\frac{P_{O_2}}{P_{O_2}^*}\right)^{\frac{1}{2}}}, \quad (93)$$

where $i_{O_2}^*$ is taken as an empirical parameter.

The ohmic overpotential is due primarily to resistance of ion transport and can be represented as:

$$\eta_{ohm} = iR_{tot}, \quad (94)$$

where R_{tot} is the total area-specific cell resistance, including the solid electrolyte R_{el} and area-specific resistances in the electrodes R_{ed} . Cermet electrodes with high metal content usually present a negligible resistance; however, in ceramic electrodes (like in LSM cathodes) the ohmic resistance can be important especially for tubular cells, which generally present quite long electronic pathways. The electrolyte resistance is generally determined from the ionic conductivity of the electrolyte σ_{el} as:

$$R_{el} = \frac{L_{el}}{\sigma_{el}}, \quad (95)$$

where L_{el} is the electrolyte thickness, while the ionic conductivity of the electrolyte is generally expressed as:

$$\sigma_{el} = \sigma_0 \frac{1}{T} \exp\left(-\frac{E_{el}}{RT}\right), \quad (96)$$

where E_{el} is the activation energy for ion transport.

Once the current density i is determined, the molar flux of the gas species from the electrochemical reactions can be evaluated as:

$$J_{H_2,a} = -\frac{i}{2F}, \quad (97)$$

$$J_{H_2O,a} = \frac{i}{2F}, \quad (98)$$

for the hydrogen electrochemical oxidation at the anode, and:

$$J_{O_2,c} = \frac{i}{4F}, \quad (99)$$

for the oxygen electrochemical reduction at the cathode. A positive flux at the anode means that mass enters the anode pore space from the anode-electrolyte three-phase boundary, while a positive flux at the cathode means that mass leaves the cathode pore space and enters the electrolyte membrane.

5.2.4 Reaction Mechanism

To solve all equations reported above, it is necessary to specify how to compute the thermal heterogeneous production rates $\dot{\omega}_k$. At a simple level, the heterogeneous production rates may be computed by using experimental correlations capable to express the rate of each species as a function of the local gas composition, without requiring any consideration linked to the surface species. However, most rate expressions come from experimental analysis and do not account for the reverse reactions that can be more and more important as the gas approaches the equilibrium condition. Consequently, this approach shows more than a limit, since reversible potentials can often be affected by considerable errors.

A more complex approach is to create a set of reversible heterogeneous reactions and to consequently compute rates using mass-action kinetics. By doing this, reverse rates can be computed in a way that is completely consistent with thermodynamics. In particular, choosing the reactions and rates to fit experimental analysis, it becomes possible to represent measured rate data under non-equilibrium conditions, and to insure that forward and reverse reactions balance as the equilibrium is approached.

5.2.5 Heterogeneous Chemistry on Nickel

The following paragraph is extracted from references [10], [11], and [52]. As said in the introduction to the present chapter, nickel is the most common anode material (in Ni-YSZ cermet) and is certainly a cost-effective material. Although there are several crucial issues associated with nickel in reforming reactors (carbon deposition, pore blocking, and deactivation on nickel are well-known problems), there is considerable evidence that SOFCs can use nickel anodes effectively. For instance, nickel is successfully used as a catalyst for hydrocarbon reforming and shifting to produce syngas (a mixture of hydrogen and carbon monoxide).

The reactions of methane on nickel have been extensively studied for decades, and different reaction mechanisms and corresponding models have been proposed. Recently, attention has been focused on making a multistep reaction mechanism based on the knowledge of the elementary steps and their energetics.

The reaction mechanism reported in Table XI consists of 42 irreversible reactions among 6 gas-phase and 12 additional adsorbed species. Most reaction rates are represented in Arrhenius form or as a sticking coefficient. However, the net reaction rates of reactions 12, 20, 21, and 23 depend on the carbon-monoxide coverage $\theta_{CO(s)}$ in the form:

$$k = AT^n \exp\left(-\frac{E}{RT}\right) \exp\left(-\frac{\varepsilon_{CO(s)}\theta_{CO(s)}}{RT}\right). \quad (100)$$

Although the reaction mechanism is written as pairs of irreversible reactions, the reverse rate coefficients depend on the forward rate coefficients and the thermodynamics. The reverse rate coefficients are computed to ensure thermodynamic consistency and an asymptotic approach to the equilibrium state.

The unity bond index-quadratic exponential potential (UBI-QEP) approach is used to determine the heats of adsorption, reaction enthalpies, and activation barriers for most relevant reactions. Specifically, the UBI-QEP method is used to evaluate kinetic parameters for the desorption of O₂, CH₄, H₂O, CO₂ (reactions 4, 6, 8, and 10), CO formation and decomposition

(reactions 19 and 20), HCO reactions (reactions 23 and 24), and non-oxidative methane decomposition and formation (reaction 27-34). Steam and carbon-dioxide formation rates (reaction 13-18, 21, and 22), HCO formation (reactions 25 and 26), and oxidative decomposition and formation of methane (reactions 35-42) are derived from a theoretical study of dry methane reforming. The sticking coefficient for hydrogen (reaction 1) is taken from chemisorption studies on Ni(111), and the hydrogen desorption rate (reaction 2) is based on an experimental study on nickel single-crystal surfaces. Owing to a lack of data on nickel surfaces, sticking coefficients for oxygen and steam (reactions 3 and 7) are estimated from studies of methane partial oxidation on rhodium. Sticking coefficients for CH₄ and CO₂ adsorption (reactions 5 and 9) are derived from experimental studies of methane reforming and oxidation over nickel-coated monoliths. The data for CO adsorption/desorption (reactions 11 and 12) are taken from Al-Sarraf et al.^[53].

Elementary reaction mechanisms can be applied more generally than global mechanisms that may be validated only for specific geometric configurations and operating conditions. The mechanism here was initially developed and validated using nickel-coated honeycomb monoliths for the temperature range from 700 to 1300 K. The validation is based on comparing measured product composition with results of two-dimensional reacting flow simulations for a single channel.

Experimental conditions consider partial oxidation and steam reforming of methane, including water-gas-shift and methanation processes. The CH₄/O₂ ratio ranged from 1.5 to 2 and steam was incorporated up to a steam/carbon ratio of 4. The steam/methane mixture, diluted by 75% of argon in terms of volume, is fed into a series of five cordierite honeycomb monoliths, each 15 mm in diameter, which are located in a ceramic tube within a furnace. The monoliths are 1 cm long and composed of straight rectangular channels with hydraulic diameters of 1.1 mm. The center monolith is coated with 3% of nickel (relative to the monolith weight) by wet impregnation. The reactor is isothermal and product composition is analyzed by mass spectrometry.

In addition to the monolith-based validation, the mechanism reported in Table XI has been recently validated in specially designed experiments using porous Ni-YSZ anode structures. These experiments consider both steam and dry reforming of methane.

Because the reaction mechanism is based on elementary molecular processes, it represents all the global processes in an SOFC anode, including steam reforming of CH_4 to CO and H_2 , water-gas-shift processes, and surface coverage. The mechanism includes surface-adsorbed carbon C(Ni) and oxygen on the surface up to one monolayer O(Ni). However, the mechanism has not been specifically validated for conditions where coking and bulk-phase nickel oxidation occur.

Work remains to be done in the development and validation of elementary heterogeneous reaction mechanisms. For instance, elementary mechanisms for carbon-formation and bulk-phase nickel oxidation are particularly needed. Additional experimental data will assist in the further refinement and validation of mechanisms such as the one used here. Moreover, as SOFC technology develops, new materials and material combinations will be used, and new reaction mechanisms will be needed.

The model described in the present work incorporates the heterogeneous chemistry in Table XI. The mechanism was taken from reference [52] and manually translated from *CHEMKIN* to *Cantera* format. In order to do this, precious information about mechanism files contained in Dalle Nogare's work was used^[54].

TABLE XI. HETEROGENEOUS REACTION MECHANISM FOR METHANE REFORMING ON NICKEL-BASED CATALYSTS.

#	Reaction	A^a	n	E^a	$\varepsilon_{CO(s)}$
1	$H_2 + (Ni) + (Ni) \rightarrow H(Ni) + H(Ni)$	$1.000 \cdot 10^{-02 b}$	0.0	0.0	-
2	$H(Ni) + H(Ni) \rightarrow H_2 + (Ni) + (Ni)$	$2.545 \cdot 10^{+19}$	0.0	81.2	-
3	$O_2 + (Ni) + (Ni) \rightarrow O(Ni) + O(Ni)$	$1.000 \cdot 10^{-02 b}$	0.0	0.0	-
4	$O(Ni) + O(Ni) \rightarrow (Ni) + (Ni) + O_2$	$4.283 \cdot 10^{+23}$	0.0	474.9	-
5	$CH_4 + (Ni) \rightarrow CH_4(Ni)$	$8.000 \cdot 10^{-03 b}$	0.0	0.0	-
6	$CH_4(Ni) \rightarrow (Ni) + CH_4$	$8.705 \cdot 10^{+15}$	0.0	37.5	-
7	$H_2O + (Ni) \rightarrow H_2O(Ni)$	$1.000 \cdot 10^{-01 b}$	0.0	0.0	-
8	$H_2O(Ni) \rightarrow (Ni) + H_2O$	$3.732 \cdot 10^{+12}$	0.0	60.8	-
9	$CO_2 + (Ni) \rightarrow CO_2(Ni)$	$1.000 \cdot 10^{-05 b}$	0.0	0.0	-
10	$CO_2(Ni) \rightarrow (Ni) + CO_2(Ni)$	$6.447 \cdot 10^{+07}$	0.0	26.0	-
11	$CO + (Ni) \rightarrow CO(Ni)$	$5.000 \cdot 10^{-01 b}$	0.0	0.0	-
12	$CO(Ni) \rightarrow (Ni) + CO(Ni)$	$3.563 \cdot 10^{+11}$	0.0	111.3	-50.0 ^c
13	$O(Ni) + H(Ni) \rightarrow OH(Ni) + (Ni)$	$5.000 \cdot 10^{+22}$	0.0	97.9	-
14	$OH(Ni) + (Ni) \rightarrow O(Ni) + H(Ni)$	$1.781 \cdot 10^{+21}$	0.0	36.1	-
15	$OH(Ni) + H(Ni) \rightarrow H_2O(Ni) + (Ni)$	$3.000 \cdot 10^{+20}$	0.0	42.7	-
16	$H_2O(Ni) + (Ni) \rightarrow OH(Ni) + H(Ni)$	$2.271 \cdot 10^{+21}$	0.0	91.8	-
17	$OH(Ni) + OH(Ni) \rightarrow O(Ni) + H_2O(Ni)$	$3.000 \cdot 10^{+21}$	0.0	100.0	-
18	$O(Ni) + H_2O(Ni) \rightarrow OH(Ni) + OH(Ni)$	$6.373 \cdot 10^{+23}$	0.0	210.9	-
19	$O(Ni) + C(Ni) \rightarrow CO(Ni) + (Ni)$	$5.200 \cdot 10^{+23}$	0.0	148.1	-
20	$CO(Ni) + (Ni) \rightarrow O(Ni) + C(Ni)$	$1.354 \cdot 10^{+22}$	-3.0	116.1	-50.0 ^c
21	$O(Ni) + CO(Ni) \rightarrow CO_2(Ni) + (Ni)$	$2.000 \cdot 10^{+19}$	0.0	123.6	-50.0 ^c
22	$CO_2(Ni) + (Ni) \rightarrow O(Ni) + CO(Ni)$	$4.653 \cdot 10^{+23}$	-1.0	89.3	-
23	$HCO(Ni) + (Ni) \rightarrow CO(Ni) + H(Ni)$	$3.700 \cdot 10^{+21}$	0.0	0.0	50.0 ^c
24	$CO(Ni) + H(Ni) \rightarrow HCO(Ni) + (Ni)$	$4.019 \cdot 10^{+20}$	-1.0	132.2	-
25	$HCO(Ni) + (Ni) \rightarrow O(Ni) + CH(Ni)$	$3.700 \cdot 10^{+24}$	-3.0	95.8	-
26	$O(Ni) + CH(Ni) \rightarrow HCO(Ni) + (Ni)$	$4.604 \cdot 10^{+20}$	0.0	110.0	-
27	$CH_4(Ni) + (Ni) \rightarrow CH_3(Ni) + H(Ni)$	$3.700 \cdot 10^{+21}$	0.0	57.7	-
28	$CH_3(Ni) + H(Ni) \rightarrow CH_4(Ni) + (Ni)$	$6.034 \cdot 10^{+21}$	0.0	61.6	-
29	$CH_3(Ni) + (Ni) \rightarrow CH_2(Ni) + H(Ni)$	$3.700 \cdot 10^{+24}$	0.0	100.0	-
30	$CH_2(Ni) + H(Ni) \rightarrow CH_3(Ni) + (Ni)$	$1.293 \cdot 10^{+23}$	0.0	55.3	-
31	$CH_2(Ni) + (Ni) \rightarrow CH(Ni) + H(Ni)$	$3.700 \cdot 10^{+24}$	0.0	97.1	-
32	$CH(Ni) + H(Ni) \rightarrow CH_2(Ni) + (Ni)$	$4.089 \cdot 10^{+24}$	0.0	79.2	-
33	$CH(Ni) + (Ni) \rightarrow C(Ni) + H(Ni)$	$3.700 \cdot 10^{+21}$	0.0	18.8	-
34	$C(Ni) + H(Ni) \rightarrow CH(Ni) + (Ni)$	$4.562 \cdot 10^{+22}$	0.0	161.1	-
35	$O(Ni) + CH_4(Ni) \rightarrow CH_3(Ni) + OH(Ni)$	$1.700 \cdot 10^{+24}$	0.0	88.3	-
36	$CH_3(Ni) + OH(Ni) \rightarrow O(Ni) + CH_4(Ni)$	$9.876 \cdot 10^{+22}$	0.0	30.4	-
37	$O(Ni) + CH_3(Ni) \rightarrow CH_2(Ni) + OH(Ni)$	$3.700 \cdot 10^{+24}$	0.0	130.1	-
38	$CH_2(Ni) + OH(Ni) \rightarrow O(Ni) + CH_3(Ni)$	$4.607 \cdot 10^{+21}$	0.0	23.6	-
39	$O(Ni) + CH_2(Ni) \rightarrow CH(Ni) + OH(Ni)$	$3.700 \cdot 10^{+24}$	0.0	126.8	-
40	$CH(Ni) + OH(Ni) \rightarrow O(Ni) + CH_2(Ni)$	$1.457 \cdot 10^{+23}$	0.0	47.1	-
41	$O(Ni) + CH(Ni) \rightarrow C(Ni) + OH(Ni)$	$3.700 \cdot 10^{+21}$	0.0	48.1	-
42	$C(Ni) + OH(Ni) \rightarrow O(Ni) + CH(Ni)$	$1.625 \cdot 10^{+21}$	0.0	128.6	-

^a Arrhenius parameters for the rate constants written in the form: $k = AT^n \exp(-E/RT)$. The units of A are given in terms of moles, centimeters, and seconds. E is in kJ/mol.

^b Sticking coefficient.

^c Coverage-dependent activation energy. Total available surface density Γ is expressed in mol/cm² and represents the tuning parameter.

5.2.6 Model Description

The following model is based on the discretization of the reaction environment of an anode-supported tubular SOFC in such a way that improves the computation of mole fractions of all species involved in the mechanism by quickly reaching convergence. Both thermodynamic and electrochemical aspects are considered in order to ensure completeness and propriety. The implementation of the model is reported in Appendix A as a *MATLAB* script.

Before running a simulation, the user must define and enter all inputs, which are pressure (constant in the present model, nearly constant in reality), temperature (constant in the present model, nearly constant in reality), the translated mechanism file (used to create a gas object and to import all phases and interfaces), current applied to the cell, fluxes (in normal liters per minute) of all chemical species entering the anode, content of water entering the anode (given as a fraction of methane flux), cell-geometry parameters (anode-channel length, anode-channel radius, anode thickness, number of cells for the axial discretization, and number of points for the radial discretization), and a shape function (optional) to define the current profile. Chemical fluxes are converted from NI/min to kmol/s, and are used to compute the initial mole fractions of all species and the mass flow rate of the mixture. Geometric parameters are used to create an axial and a radial grid for the discretization of the problem and to compute both the inlet area and the anode reacting-surface area. It is important to specify how the anode thickness is not used to study the phenomena occurring within the anode, but it is somehow considered to be such an extension of the anode radius. This is an approximation used to improve chemical processes occurring within the anode channel and represents a first challenge for further research, since this model does not aim to precisely explain what happens inside the anode, but focuses on the phenomena occurring in the fuel channel.

The fuel channel is divided into a certain number of axial cells, while every cell is analyzed only along the radial coordinate, that is divided into a certain number of solution points. This is consistent if we consider that the radial behavior of the cell does not represent an issue as

interesting as in the case of the axial behavior. The solution is computed by using a cycle whose number of iterations equals the number of axial cells. Gas initial composition is updated at every iteration with the final results coming from the previous cell. Here come some approximations. First of all, in order to analyze the radial behavior of a cell (from now on, when we talk about a cell in this paragraph we will refer to a cell deriving from the discretization of the fuel channel), a radial wedge is considered to be a one-dimensional rectangular channel, as described in Figure 37. The coordinate for the one-dimensional channel is of course the radial one, varying from zero (which represents the axis of the channel) to the channel radius, which can be extended by exploiting the anode thickness.

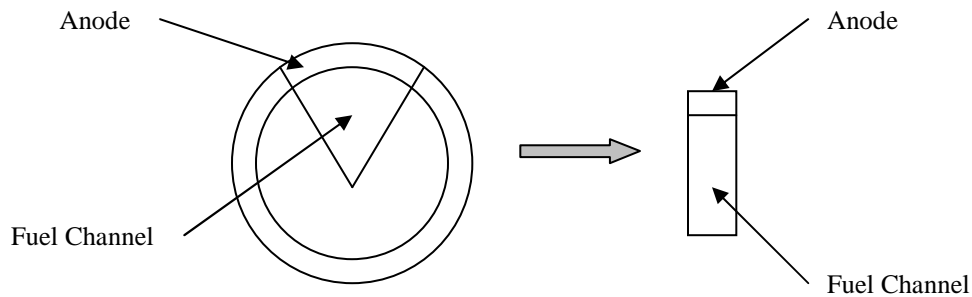


Figure 37. Radial-wedge-to-rectangular-channel approximation.

The radial problem is solved for every cell by creating a stack object, which consists of an inlet (whose flux is computed by dividing the mass flow rate entering the channel by the inlet area), an axis-symmetric flow representing the gas flux along the radial coordinate, and a surface representing the anode reacting surface. This is an approximation again: although we are analyzing the radial behavior of the channel, in order to define the inlet flow rate for the next cell, we divide the radial gas flux by the cross-sectional area of the channel, which is the correct inlet

area for the next cell to come in the computation. Of course, the mass flow rate entering the channel is corrected with the mass flow rate induced by the current applied to the fuel cell if any. It is clear how the main intent is to create an axial flow along the channel by dividing it into a series of radial flows. By doing so, we consider the axial phenomena, which are correlated to diffusion, to be more important than the radial ones, which are correlated to convection. Moreover, the anode is considered to be such a wall, but, as we said before, the aim of this work does not contemplate the study of porous-electrodes theory. Basically, this means that the anode reacting-surface is considered to be only the interface between the anode and the fuel channel by approximation.

Once the boundaries are set for the main quantities (temperature, axial velocity, and radial velocity), the stack object is solved for every cell by first solving the energy equation and by then turning on all surface chemistry relations (surface-species coverages are first advanced by integrating the coverage equations in time for one second, holding the gas composition fixed to generate a good estimate for the actual computation). It is possible to speed up the computation by defining tolerances for both the steady-state problem and for time stepping, while the radial grid can be refined by setting stringent refinement criteria if needed.

In order to compute the final gas composition of a cell and, consequently, the initial gas composition for the next cell to come, net production rates of all chemical species are computed directly from the mechanism files, while production and destruction rates due to the current applied to the fuel cell are computed by exploiting Faraday's law. Once the molar flow for every single species is found, it is easy to compute all mole and mass fractions, and results can be employed in the next cell to carry on the main cycle until the last iteration is solved and the exhaust gas composition is eventually defined.

5.3 Experimental Setup

Experimental tests have been performed on a commercial tubular SOFC produced by *Acumentrics* (US). The cell is an anode-supported based with a Ni-YSZ anode, an 8YSZ cathode, and an LSM cathode. The channel is 331 mm long, while the inner diameter is 10.5 mm. The anode, the electrolyte, and the cathode are 1700, 37, and 50 μm thick, respectively. The cell is designed with a triple current take off to reduce Ohmic losses due to the current collection.

The cell has been experimentally characterized in the *Acumentrics SOFC Test Stand*, designed to operate as a platform for the qualification of up to five individual SOFC cells. The test stand incorporates all the equipment needed to feed the cells, to control their operation conditions and to record experimental results. The *Test Stand* is formed by the following main components:

- the Furnace/Loads, which consist of a furnace (or oven) and a Load Board for the tube electrical testing;
- the Gas Manifold/Water Bottles supplies, which properly moisturize fuel and air entering the SOFC tube through five mass flow controllers;
- the Control Electronics, which contains the Interface Board, the Temperature Controllers, the Fault/Reset Display, the Data Logger, and the Emergency Stop Button; the electrochemical behavior of the fuel cell is investigated, being the current load an input parameter, through five voltmeters placed along the tube;
- the Power Supply, which provides a 2-Volt bias to the load to overcome lead and connection voltage drops; a 24-Volt supply for printed circuit boards is also available;
- the Primary Power Shelf, which supplies the main electrical sources, backup UPS power, and main circuit breakers for the stand, three circuit breakers placed on the front panel control the furnace/oven.

A scheme of the tubular SOFC test rig showing the basic P&ID is reported in Figure 38.

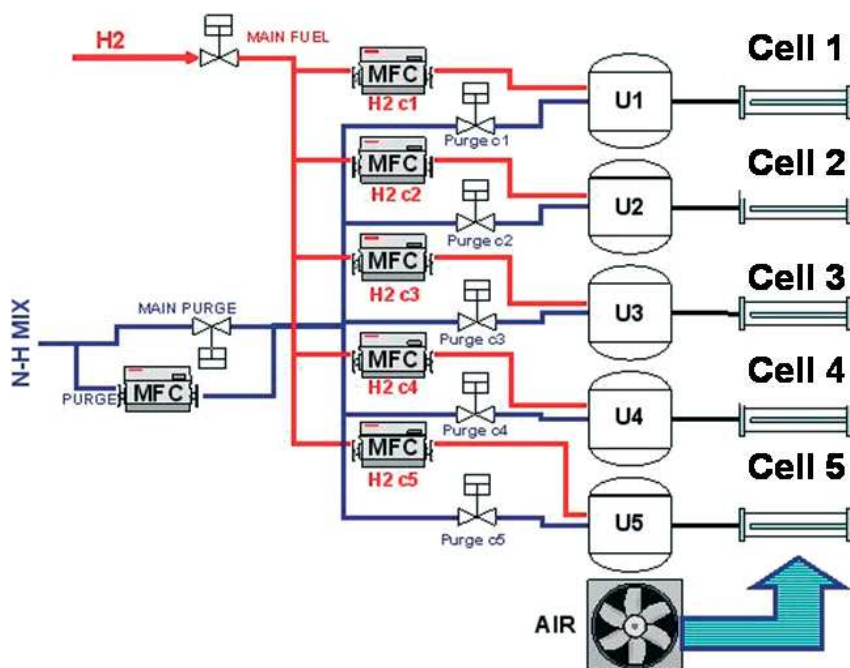


Figure 38. Scheme of the tubular SOFC test rig showing the basic P&ID.

Figure 39 shows both the front and the rear side of the *Test Stand*. In particular, the control electronics, the furnace, the gas manifold, and the exhaust-gas outlet are clearly visible on the front side (*a*), while the rear side (*b*) shows the bubbler and part of the internal piping. Figure 40 shows the tubular SOFC after it was assembled inside the furnace. An overall view is given (*a*), as well as the detailed views of both the fuel-inlet connection (*b*) and the exhaust-outlet connection to the cooling coil (*c*). The latter connection needs the application of a thick layer of a sealing ceramic material in order to avoid leakage. Figure 40c shows the connection before the sealant was applied. Instead, the ceramic sealant (opaque-white colored) is clearly visible in Figure 40a.



(a)

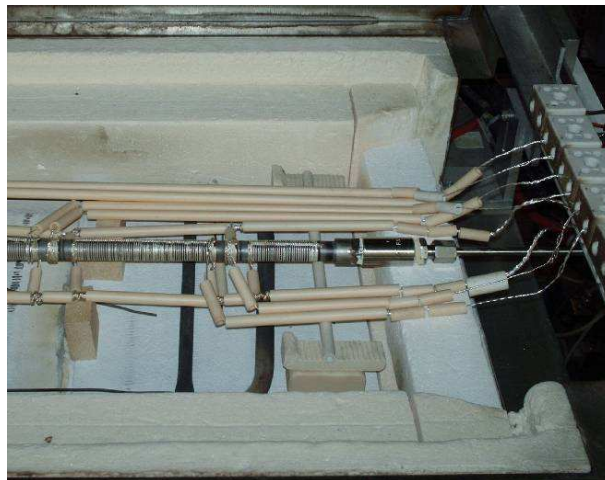


(b)

Figure 39. Acumentrics SOFC Test Stand



(a)



(b)



(c)

Figure 40. Acumentrics tubular SOFC

Since the fuel cell presents an anode-supported design, the fuel flows inside the channel, while the oxidant is provided by a blower to the external side of the cell. The air flow provided by the blower is spread inside the furnace by an air distribution circuit, which is also designed to homogenize temperature inside the furnace. In the anode bulk flow, three thermocouples have been placed along the longitudinal direction to control temperature within the anode volume. Within the ceramic oven, where the cell is placed, electric heaters maintain the oven temperature to a set value. Heat transfer between the cell and the heaters occurs mainly through radiation and convection between the air circulating in the oven and the external (cathodic) side of the tubular cell. The oven temperature was respectively set to values of 830, 780, and 730°C, to guarantee inside the cell temperatures of 800, 750, and 700°C, respectively, depending on the specific experimental investigation considered. This is due to the fact that the temperature inside the cell (i.e., inside the anode volume) is always found to get a somewhat lower value, mainly because the fuel gas mixture is not pre-heated before entering the cell. We can reasonably assume that the fuel is pre-heated only in the few centimeters that separate the cell inlet section from the outside of the furnace. Here, an high-temperature metallic alloy is welded to the ceramic cell to provide a connection between the cell itself and the external stainless steel fuel piping.

Test sessions were aimed to acquire data about the cell performance under conditions simulating processes occurring during a real biogas internal reforming. All details are reported in Appendix B. Tests have been performed with a single cell mounted inside the oven, as follows:

- the cell is kept unloaded until the cell voltage and the oven temperature are stable;
- both dry and steam reforming experiments are performed to investigate the effectiveness of both processes;
- the cell is loaded with different currents and under different fuel flows to produce enough experimental data to draw performance maps of the fuel cell;

- a bio-methane fuel mixture (60% of methane and 40% of carbon dioxide in volume terms) was used for all experiments (we can consider it like a rough biogas composition where all small contaminants are removed and represented by carbon dioxide only);
- several internal dry reforming tests were performed by adding respectively 1, 1.5, and 2 moles of carbon dioxide to each mole of biogas, in order to investigate the carbon-dioxide addition effect;
- several internal steam reforming tests were performed by adding respectively 0.3, 0.4, 0.5, and 0.6 moles of water to each mole of biogas, in order to investigate the steam addition effect;
- temperature was varied inside the furnace as mentioned above in order to study the temperature effect (for the steam reforming case only); three temperatures were taken along the bulk flow of the anode channel (at a distance of 140, 260, and 320 mm, respectively, from the tube exit);
- five voltage values were taken along the fuel cell through five voltmeters; since discrepancies between the voltage values may be quite considerable sometimes, only the voltage of the central voltmeter, which turned out to be the most stable, was taken as reference.

We must note that it was not possible to use biogas compositions as precise as the ones used for the combustion study because of the limits linked to the mass flow controllers, which do not work under a certain threshold. In fact, the mass flow rates to be put inside the controllers must be in the range of 60-1000 Nml/min for dry reforming tests and in the range 80-1000 Nml/min for steam reforming tests. This is due to the different mass flow controllers used for the two experimental sessions. Also, we should specify that the mass flow controllers used for all experiments are not specifically designed for methane and carbon dioxide, and this means that all actual mass flow rates must be timed by a correction factor before entering controllers. Since the correction factor is 1.38 for carbon dioxide and 1.33 for methane, in order to respect the lower

limits of 60/80 Nml for both gases, we cannot practically choose methane mass flow rates which are lower than 50 Nml/min when performing dry reforming, and lower than 87 Nml/min when performing steam reforming. This represents a strong limitation for our study, since it is well-known that having relatively low mass flow rates means achieving high efficiencies.

When performing dry reforming experiments, carbon dioxide coming from biogas is sent to the cell together with the carbon dioxide needed for the reforming process. This is due to the channel net itself, where methane and carbon dioxide presents an only tube each.

When performing steam reforming, the number of moles of water to be added to biogas is determined by varying the temperature of a bubbler that pre-heats water. We must specify that only the methane flow goes through the bubbler and is thus premixed. This is due to the channel net again, where only the main fuel channel is connected to the bubbler (main fuel can be set to be either methane or hydrogen).

Voltage values can present considerable discrepancies (up to 300% sometimes) depending on the specific voltmeter considered. This is essentially due to an excessive thermal expansion of silver connection cables. For this reason, not all voltage values are employed in the computation: voltage-measurement criteria will be specified in the next chapter.

During start up and in case of ordinary or emergency shutdown of the system, a safety gas mixture called *NH-mix* (consisting of 95% of nitrogen and 5% of hydrogen in terms of volume) is sent to the cell anode compartment to purge the system, keeping the anode in reducing atmosphere to preserve its functionality.

CHAPTER 6

SOFC EXPERIMENTAL RESULTS AND MODEL VALIDATION

6.1 Introduction

The following chapter aims to present a large collection of the experimental data acquired while performing multiple tests on the tubular SOFC described in the previous chapter. In particular, several polarization tests have been performed in order to draw polarization curves and fuel utilization maps, while gas analysis was carried out through a gas chromatograph in order to validate the gas composition at the fuel-channel exit, which was first computed by employing the model described in the previous chapter for different operational conditions. For each of these tests, the cell behavior was investigated for both dry and steam reforming processes, respectively.

6.2 Dry Reforming

All dry-reforming experimental tests have been performed by first setting the cell temperature to 800°C. Starting from theoretical considerations and taking the biogas composition chosen as reference (60% of methane and 40% of carbon dioxide in volume terms), at that temperature it is easy to deduce that, for each mole of biogas, it is necessary to add 0.8 moles of carbon dioxide, in order to avoid the so-called carbon deposition phenomenon. For this reason, the cell behavior has been investigated for different carbon dioxide-to-biogas molar ratios, which are 1, 1.5, and 2, respectively (carbon dioxide-to-methane ratios are 2.33, 3.17, and 4, respectively).

6.2.1 Polarization Curves

Polarization tests have been performed starting from the OCV (Open Circuit Voltage) condition and increasing the current load by 2.5 A each time (this operation can only be done manually on the control panel). After the considered voltage value gets stable (or, in general, after 3 minutes), it can be registered for that particular operational condition. Current load can be

generally increased as long as it remains higher than a somehow critical threshold set to 200 mV. This procedure has been repeated for several fuel mass flow rates and for each carbon dioxide-to-biogas ratio.

Figure 41 through Figure 44 present the polarization curves, which show how the cell voltage and the electrical power vary when current density is increased, for different carbon dioxide-to-biogas ratios when methane mass flow rates vary from 60 Nml/min to 160 Nml/min. Since we know biogas composition and carbon-dioxide addition, it is easy to compute carbon-dioxide mass flow rates, which are not reported on plots.

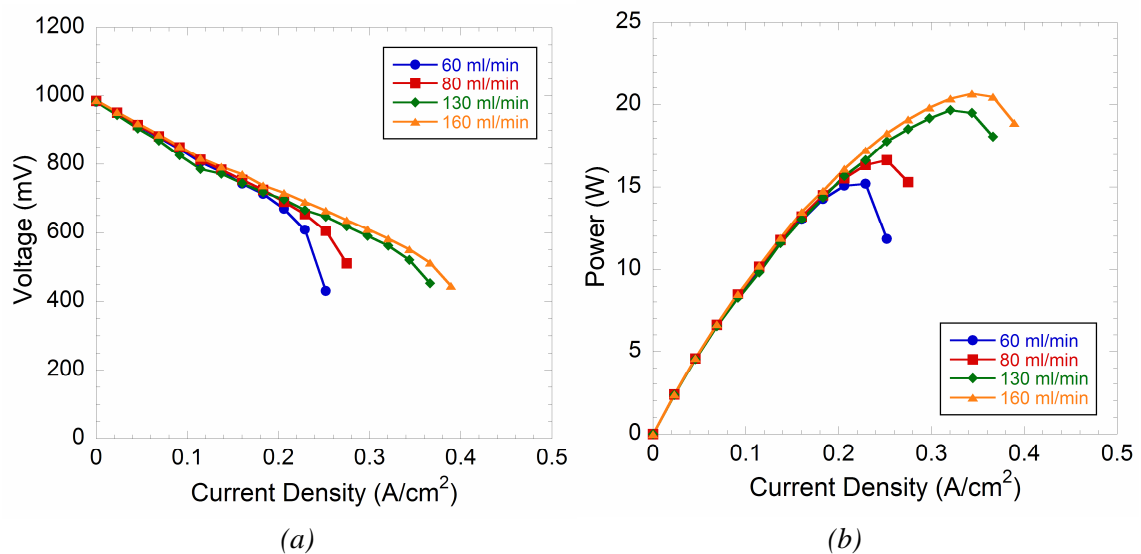


Figure 41. Polarization curves for different methane mass flow rates when carbon dioxide-to-biogas ratio is set to 1.

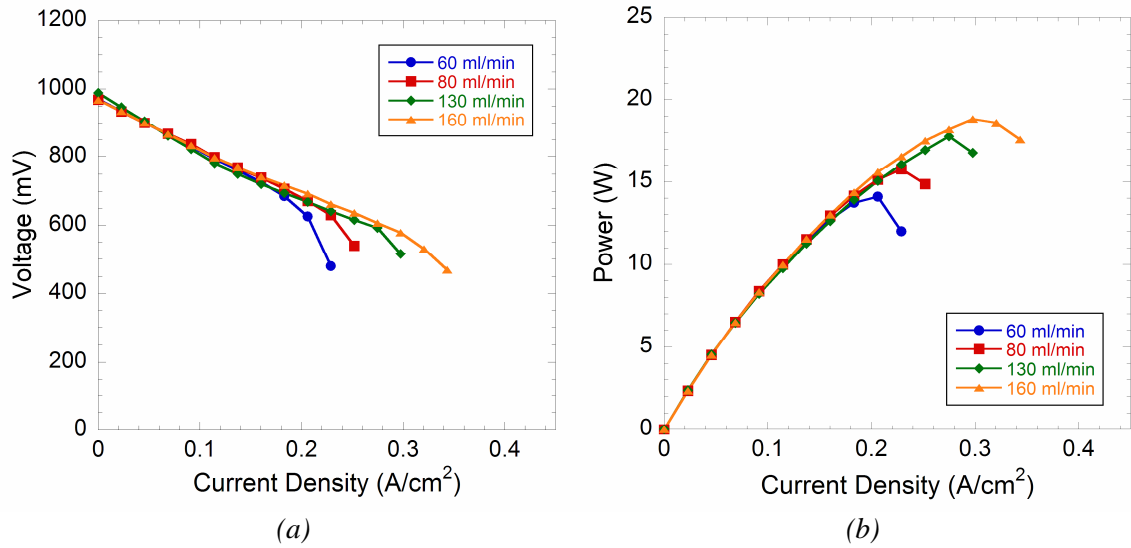


Figure 42. Polarization curves for different methane mass flow rates when carbon dioxide-to-biogas ratio is set to 1.5.

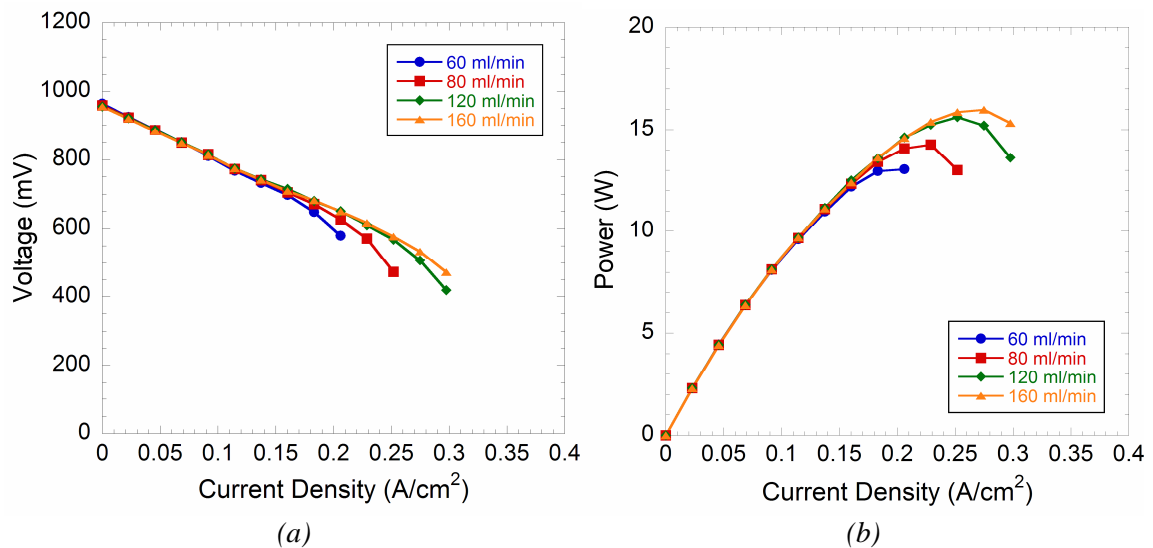


Figure 43. Polarization curves for different methane mass flow rates when carbon dioxide-to-biogas ratio is set to 2.

It is easy to state that the trend of all curves is the same, with Ohmic losses being predominant when current density reaches relatively high values. Power maximum peaks are more appreciable

when methane mass flow rates are high, and this is due to the fact that voltage falls dramatically down after a certain current-load threshold as methane mass flow rate approaches the minimum rate available on the mass flow controllers. When current density is high, best performances are achieved for high methane mass flow rates. This is due to the fact that, at constant current, increasing fuel mass flow rate means getting lower fuel utilization factors. Fuel utilization factor (FU) is defined as follows:

$$FU = \frac{\dot{n}_{CH_4}^{stoich}}{\dot{n}_{CH_4}^{actual}}, \quad (101)$$

where $\dot{n}_{CH_4}^{stoich}$ is the methane stoichiometric molar flow rate (in mol/s), while $\dot{n}_{CH_4}^{actual}$ is the methane molar mass flow rate actually employed for the experimental test. The latter term turns out to be:

$$\dot{n}_{CH_4}^{actual} = \frac{I}{8F \cdot FU}, \quad (102)$$

where I is the current load, F is the Faraday constant, and 8 indicates the number of electrons exchanged for the methane case.

It is important to specify how the performance of the tubular cell exploited for the present investigation can considerably vary depending on the day of use. In fact, the cell is very sensible because of the rather old technology behind it and may sometimes need a couple of days in order to be fully chemically activated. This may lead to discrepancies in the voltage output which are up to 5% (when current load and fuel mass flow rate are set to the same values). In particular, performance grows when the cell is kept switched on the day before, and it gets ultimately stable after a couple of days. Moreover, this kind of fuel cell largely suffers thermal cycles, and thus it is crucial to reduce the number of startups and shutdowns as much as possible.

6.2.2 Influence of Carbon-Dioxide Addition

Figure 44 shows the trend of the cell voltage and the electrical power as functions of the current density when methane mass flow rate is fixed and set to 60 Nml/min. Carbon dioxide-to-

biogas ratios are 1, 1.5, and 2, respectively. Maximum peaks are not appreciable in the power plot because of the excessive voltage drop at high current, but it is easy to see how the trend is the same for all curves.

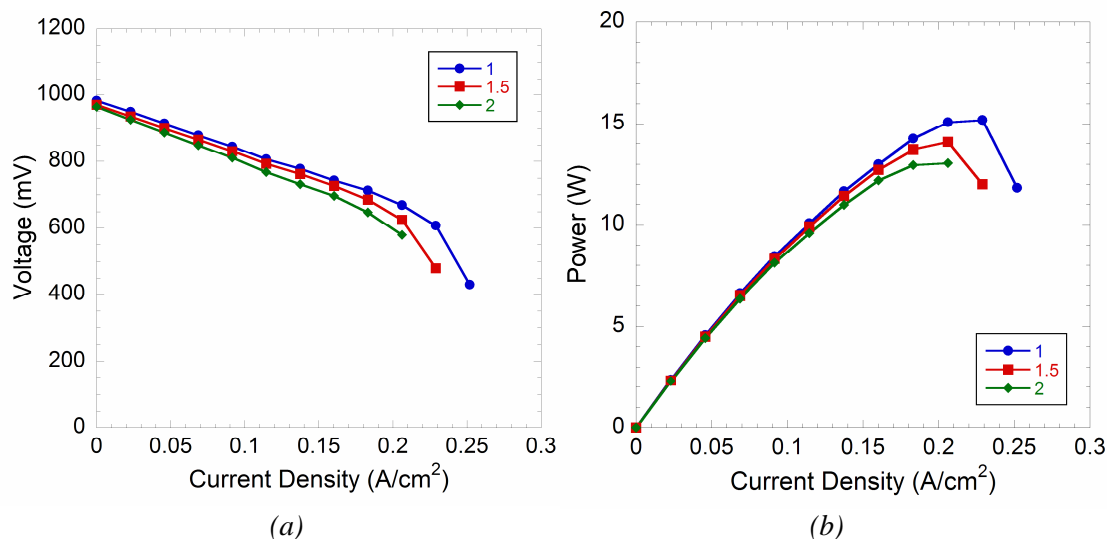


Figure 44. Polarization curves for different carbon dioxide-to-biogas ratios when methane mass flow rate is set to 60 Nml/min.

Best performances are achieved when carbon dioxide-to-biogas ratio is set to unity, with voltage and power decreasing when fuel dilution gets higher. The same fact occurs for different methane mass flow rates, as shown in Figure 45 through Figure 47. Here, methane mass flow rates are set to 80, 140, and 160 Nml/min, respectively. Hence it is clear how dry reforming seems to be more effective for small carbon dioxide-to-biogas ratios from a performance viewpoint. This is partly due to the fact that biogas already contains carbon-dioxide, which actually takes part in the methane-reforming process because of the experimental-setup configuration itself. Then, we can easily understand how a carbon dioxide-to-biogas ratio set to unity means having a carbon dioxide-to-methane ratio which is higher than 2. An extensive exhaust-gas analysis will be useful

in order to further investigate the effectiveness of dry reforming processes inside the tubular SOFC.

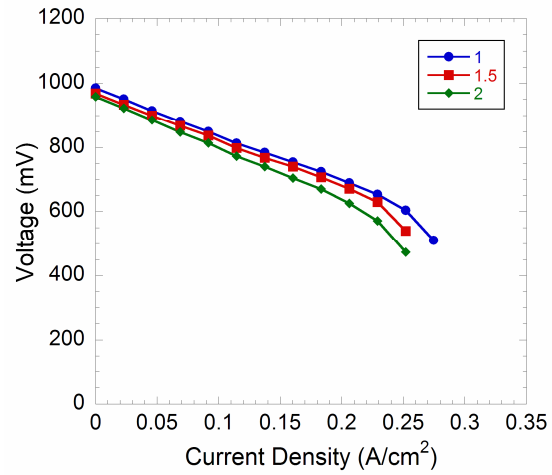


Figure 45. Voltage polarization curve for different carbon dioxide-to biogas ratios when methane mass flow rate is set to 80 Nml/min.

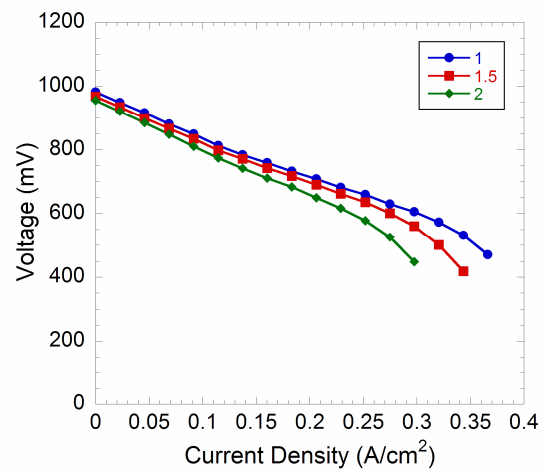


Figure 46. Voltage polarization curve for different carbon dioxide-to biogas ratios when methane mass flow rate is set to 140 Nml/min.

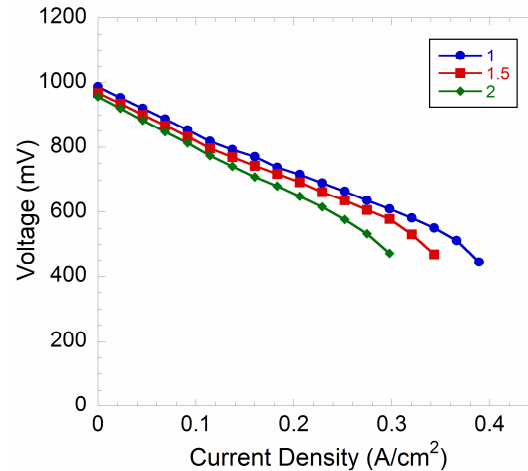


Figure 47. Voltage polarization curve for different carbon dioxide-to biogas ratios when methane mass flow rate is set to 160 Nml/min.

6.2.3 Fuel Utilization Maps

Fuel utilization factor FU can be also defined as the ratio between the current load applied to the cell and the maximum current obtainable with the amount of fuel entering the cell. The latter current is computed through the Faraday's law. Thus:

$$FU = \frac{I}{I_{\max}} \quad (103)$$

Fuel utilization maps (or efficiency maps) have been drawn starting from a certain current load (which was always 7.5 A because of the lower limit imposed by the mass flow controllers) and the methane mass flow rates correspondent to an FU of 25%. The cell voltage was registered when stable and fuel mass flow rates were progressively decreased in such a way to obtain an FU which was 5% higher than before. This was repeated as long as the cell operation was possible (because of mass flow controllers again) and acceptable. After analyzing the cell behavior for a particular current load, the procedure was repeated by increasing the latter load by 2.5 A until a maximum of 25 A. The cell efficiency, which is defined to be the ratio between the power

produced by the cell and the power obtainable with that particular amount of fuel, is computed as follows:

$$\varepsilon = \frac{P}{P_{\max}} = \frac{VI}{\dot{n}_{CH_4} \frac{LHV_{CH_4}}{V_{normal}}}, \quad (104)$$

where V is the cell voltage, LHV_{CH_4} is the lower heating value of methane measured in J/mol, V_{normal} is the volume occupied by a mole of methane under normal conditions (at 1 atm and 273.15 K) measured in liters/mol, and \dot{n}_{CH_4} is the methane volume flow rate measured in liters/s.

Figure 48 through Figure 50 point out the relation existing between the cell efficiency and the electrical power produced by the cell. Carbon dioxide-to-biogas ratio are set to 1, 1.5, and 2, respectively. Lines of the same color connect operational points characterized by the same current load (which is indicated near the points having lower FU). Black lines, generally presenting a slight negative slope, combine points with the same FU (the FU value is shown near the points at lower current).

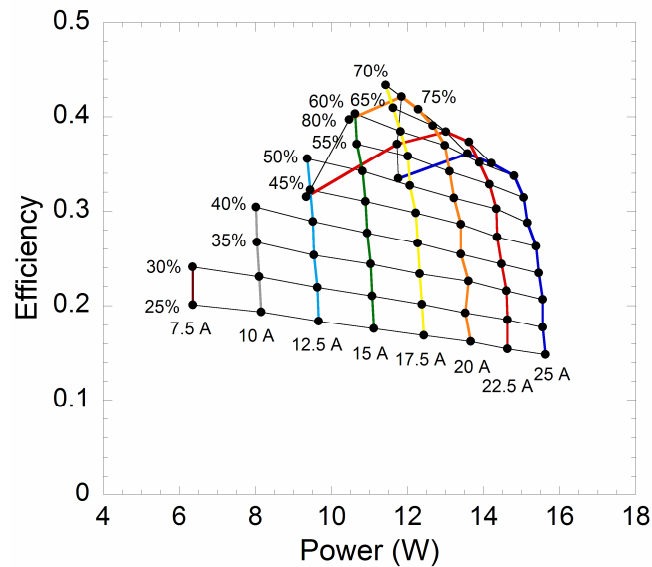


Figure 48. Efficiency map when carbon dioxide-to-biogas ratio is set to 1.

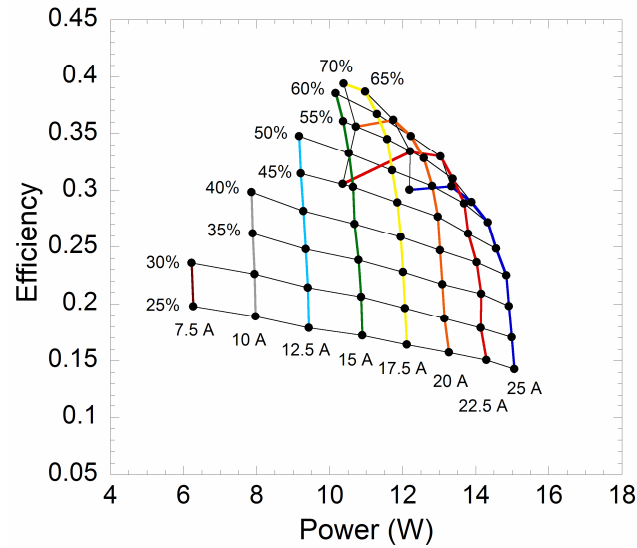


Figure 49. Efficiency map when carbon dioxide-to-biogas ratio is set to 1.5.

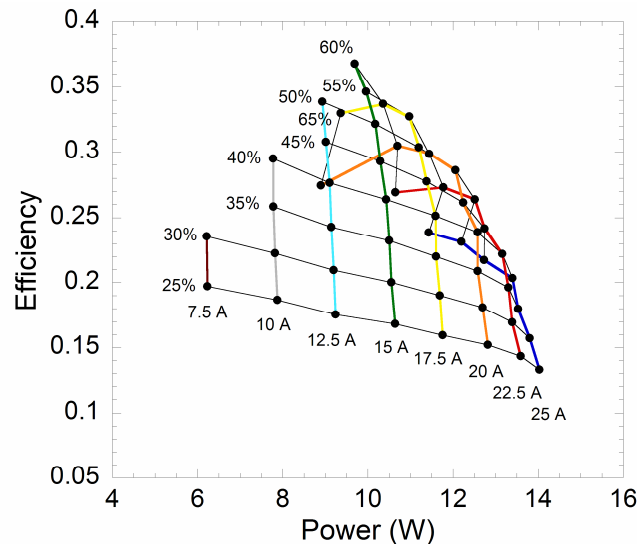


Figure 50. Efficiency map when carbon dioxide-to-biogas ratio is set to 2.

Focusing on the best performance case shown in Figure 48 (when carbon dioxide-to-biogas ratio is set to unity), we can start making some general considerations. First, at constant FU, efficiency

decreases when the current applied to the cell is increased because of Ohmic losses due to current collection. Secondly, if we consider the points at high current having the same load, we can easily see how efficiency grows much for points with lower current, as well as the FU factor correspondent to the efficiency maximum peak. Thirdly, it would be extremely interesting to decrease the fuel mass flow rates (this was not possible because of the limitations mentioned above) at low current, in order to get a very high FU factors. This operational condition should lead to a further rise of efficiency. Generally, high current loads and high FU factors allow the researchers to observe the cell limit operating conditions, beyond which the cell voltage dramatically falls below a critical threshold (around 200-300 mV). This is an issue which is quite peculiar of tubular cells compared to planar cells, since the former generally have longer electronic paths for the electrons to reach the current collecting regions. In the tested cell, a silver mesh, in the form of wrapped wires twisted all over the external side of the cell (cathode surface), acted as a current collector. Otherwise, a much less efficient current collection was available on the anode side. In fact, the cell is fragmented into four sectors: in between two contiguous sectors the anode is left naked (which means that is not covered by neither the electrolyte nor the cathode), and here is where the anode current collection takes places by wrapping silver wires on the naked portions again. This arrangement brings longer electronic paths (compared to the cathode side), which inevitably causes an overall high Ohmic resistance of the cell.

In Figure 48, maximum efficiency (on LHV basis), which is 43.4%, is achieved when FU factor is 70%, current load is 17.5 A, electrical power is 11.4 W, and methane mass flow rate (actual one is 44 Nml/min) is close to the lower limit of the mass flow controller.

Figure 49 and Figure 50 show the performance maps of the tubular cell when carbon dioxide-to-biogas ratio is increased to 1.5 and 2. General considerations made above stay valid for both cases. When the ratio is equal to 1.5, maximum efficiency is 39.4% and is reached when FU factor is 70%, current load is 17.5 A, electrical power is 10.4 W, and methane mass flow rate is 44 Nml/min again, while, for the second case (carbon dioxide-to-biogas ratio equal to 2),

maximum efficiency is 36.8% and is achieved when FU factor is 60%, current load is 15 A, electrical power is 9.7 W, and methane mass flow rate is 44 Nml/min. By analyzing the three maps together, it is clear again how dry reforming seems to be more effective for carbon dioxide-to-biogas ratios which are close to unity.

6.2.4 Gas Analysis and Model Validation

After deciding a significant number of operational points, an extensive analysis of exhaust gases coming out of the fuel channel (anode side) has been performed through a gas chromatograph, which was properly calibrated for this kind of mixtures. In fact, an outlet-gas-composition analysis may represent a precious tool for evaluating the chemical and electrochemical reactions occurring inside the cell, and for making thermodynamic considerations regarding the achievement of chemical equilibrium of the fuel input.

The gas-mixture composition obtained through the gas chromatograph is only related to dry gases and provides the user with the percentage volume of each component in the gas mixture. In all samples analyzed by the gas chromatograph, non-negligible percentages of nitrogen (from 1.5% to 15.4%) were found, and sometimes small amounts of oxygen (up to 2%) were found as well. It is well-known that nitrogen and oxygen should not be among the reaction products if the system is well sealed and there is no leak. Therefore, we can state that this deals with an experimental error, which is probably due to air infiltration inside the furnace or along the outlet pipe before gases are collected. For this reason, concentration values for nitrogen and oxygen were removed from the experimental results by normalizing the sum of other gaseous species to 100%, in order to get a meaningful comparison between the reaction products involved in the process.

A practical experimental constraint is represented by the fact that, when setting low fuel mass flow rates, it may take several hours to adequately fill the gas-collection bag. Also, sometimes the cell voltage may approach critically low values and it may be necessary to increase fuel mass flow rate in order to prevent the cell from damaging. Thus, it may be literally

impossible to perform gas analysis for many operating points (i.e., at low current and high FU factor).

The model described in the previous chapter, which was completely implemented on *Cantera* for predicting mole fractions of chemical species in the anode exhaust gas mixture, has been validated by comparing the results with the experimental data obtained through the gas-chromatograph analysis. Moreover, for the OCV cases only, *CEA* was also used to estimate the final composition of the mixture (by first removing the water content in order to provide a better comparison for dry gases) under conditions of thermodynamic equilibrium (the software minimizes the Gibb's free energy of the mixture at 800°C). This further analysis can be very useful to better understand how far the gas mixture is from the conditions of thermodynamic equilibrium inside the fuel channel.

Figure 51 through Figure 53 present a comparison between the experimental data acquired by the gas chromatograph and the results obtained by exploiting both the present model and *CEA*. No current load is applied to the cell (OCV configuration), methane mass flow rate is set to 50 Nml/min, and carbon dioxide-to-biogas ratios are 1, 1.5, and 2, respectively. In order to get a good match between the experimental data and the results obtained by running *Cantera* simulations, the number of radial cells has been set to 8 (it does not represent a crucially important parameter since mole-fraction radial profiles are almost horizontal lines), the number of axial cells has been set to 50 (convergence is reached very quickly and errors in mole fractions are already lower than 0.01 when using 25-30 axial cells), and surface site density (which depends on the anode structure and represents the only actual tuning parameter in the present model) has been set to $25.00 \cdot 10^9$ mol/cm² for all dry-reforming tests (all programming details are provided in Appendix A). This value is quite high if compared to the one used in references [10], [11], and [52], which is $2.60 \cdot 10^9$ mol/cm². However, this is the only parameter that actually characterises the anode and it strongly depends on the crystalline structure of the anode itself. Furthermore, references [10] and [11] refer to the study of planar SOFCs, while no value for the

tubular configuration is provided by current literature when using the present reaction mechanism.

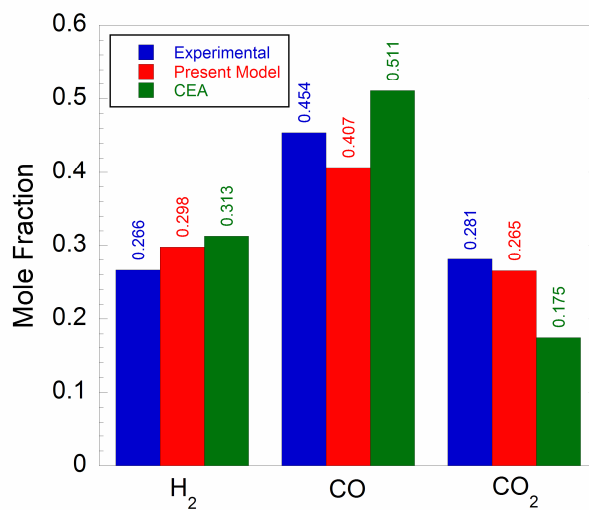


Figure 51. Mole-fraction comparison for main dry-gas species when carbon dioxide-to-biogas ratio is set to 1 (OCV configuration).

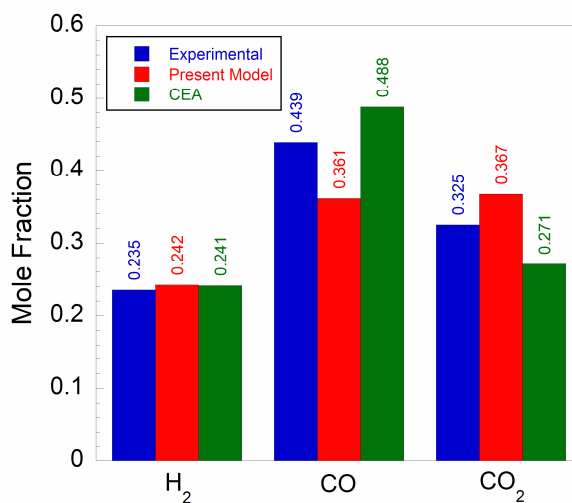


Figure 52. Mole-fraction comparison for main dry-gas species when carbon dioxide-to-biogas ratio is set to 1.5 (OCV configuration).

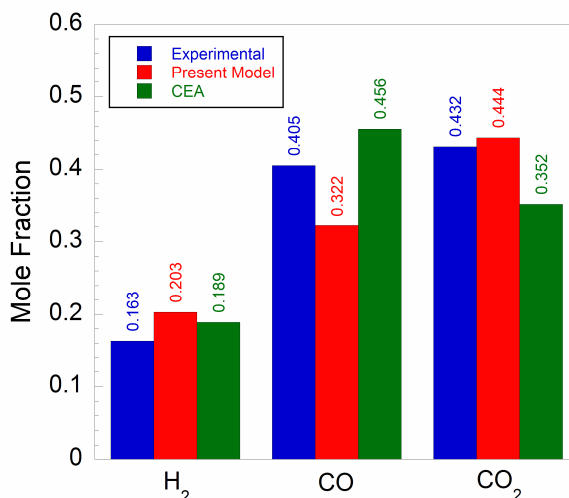


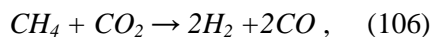
Figure 53. Mole-fraction comparison for main dry-gas species when carbon dioxide-to-biogas ratio is set to 2 (OCV configuration).

In all cases it is clear that the hydrogen and carbon-monoxide mole fractions are lower than the ones needed to achieve thermodynamic-equilibrium conditions, while carbon-dioxide production is much higher than the one expected for the same purpose. Results coming from the present model show a similar trend except for carbon-monoxide, whose mole fraction is lower than the actual value. Predicted methane mole fraction (not reported in figures) is around 3% for all cases. Predicted water content (around 2% for all cases) has been neglected and mole fractions of gaseous species have been normalized to get a better dry-gases comparison. Although the match between the present-model and the experimental results is quite good (errors are higher than 5% only for carbon-monoxide), we should now specify why errors occur. First, as we said before, the model shows a certain amount of methane in the exhaust, that does not take part in the dry-reforming process, and water content has been neglected. This surely introduces an error in the computation of other mole fractions, since no methane and water are found by the gas-chromatograph analysis. Secondly, in each of the previous tests, a relatively high content of nitrogen has been found (8.76% for Figure 51, 8.86% for Figure 52, and 4.95% for Figure 53),

probably due to air infiltration. If air enters the fuel channel (and this is what probably occurs since no oxygen is found in the final composition), this means that oxygen is free to react inside the channel and alternative reactions (like methane and hydrogen combustion) can occur. This could explain why no methane is found in the final composition, why actual hydrogen mole fraction is lower than the one predicted, and why carbon-monoxide production seems to be much higher in reality (carbon monoxide is an unstable intermediate product of methane combustion, which can turn into carbon dioxide in the presence of oxygen or water). It is more difficult to give an effective explanation of what occurs to carbon dioxide (predicted carbon-dioxide content is lower than experimentally found only when carbon dioxide-to-biogas ratio is set to 1), since its production/destruction should depend on the balance existing between dry reforming (destruction), methane combustion (production), and possible gas-shift reaction (production). In fact, when dealing with such complex mechanism files, it may be quite impossible to estimate which chemical process is actually encouraged most. As we will underline later, the mechanism file used for the present model seems to strongly encourage water gas-shift reactions (even though, at high temperatures and for high carbon-dioxide contents, the chemical equilibrium should be shifted towards the inverse gas-shift process), whose overall process is described by:



over both dry reforming reactions, which are globally described by the following reaction:



and steam reforming reactions, which are globally described as follows:



This may generally lead to a much lower carbon-monoxide mole fraction and a considerably higher carbon-dioxide production in simulations if compared to the experimental results. The reason why this occurs is to be found inside the mechanism file through a deep analysis of the parameters for the Arrhenius formulation, whose source is however experimental and extensively validated^{[10],[11]}. For this reason, this aspect will not be further investigated in the present work.

Eventually, focusing on the experimental data only, we can easily state how, in OCV configuration and at constant methane mass flow rate (and biogas mass flow rate indeed), by increasing the carbon dioxide-to-biogas ratio we strongly increase the final carbon-dioxide content, while hydrogen and carbon-monoxide productions are considerably decreased. Thus, considering the composition of biogas fixed for the present work, gas-chromatograph analysis seems to confirm how dry reforming works more efficiently as carbon dioxide-to-biogas ratio gets closer to unity.

Figure 54 through Figure 56 present a comparison between the experimental results and ones obtained by exploiting the present model when current applied to the cell is 15 A, FU factor is 50%, and methane mass flow rate is set to be 53 Nml/min. Carbon dioxide-to-biogas ratio is set to 1, 1.5, and 2, respectively.

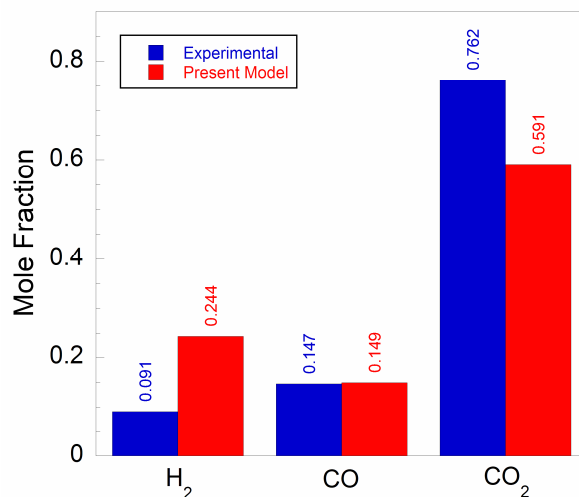


Figure 54. Mole-fraction comparison for main dry-gas species when carbon dioxide-to-biogas ratio is set to 1 ($I = 15$ A, $FU = 50\%$).

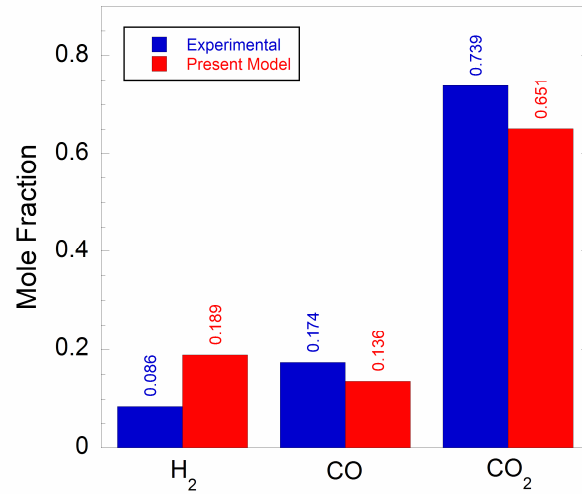


Figure 55. Mole-fraction comparison for main dry-gas species when carbon dioxide-to-biogas ratio is set to 1.5 ($I = 15$ A, $FU = 50\%$).

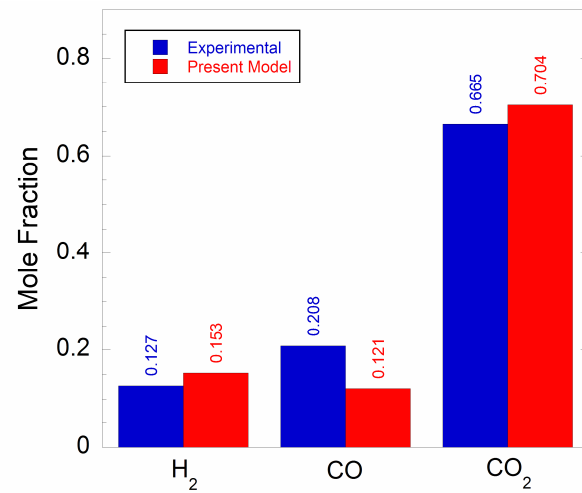


Figure 56. Mole-fraction comparison for main dry-gas species when carbon dioxide-to-biogas ratio is set to 2 ($I = 15$ A, $FU = 50\%$).

Differently from the OCV cases, the trend of dry-gas mole fractions largely differs this time (although conditions for the three tests are set to be the same), depending on the carbon dioxide-to-biogas ratio applied, with the only hydrogen concentration being considerably higher than the

experimental one for all cases. Also, the match between experimental and model results does not seem to be as good as before, although it still looks acceptable. There can be multiple explanations for this mismatch. First, we must consider the water-neglect error again. In fact, final water content is strongly affected by its electrochemical production, which is activated by the current load, with neglected mole fractions varying from 13% to 16% for the present samples. Secondly, relatively high amounts of nitrogen (8.15% for Figure 54, 15.44% for Figure 55, and 13.64% for Figure 56) were found by the gas-chromatograph analysis again, with oxygen concentrations being constantly under 1.3%. Thus, hydrogen and methane (whose concentrations in the final composition are around 2% for all cases) combustion processes may have taken place (and this would partly explain the generally high discrepancies in hydrogen and carbon-monoxide mole fractions), as well as a strong gas-shift process (capable to explain the extremely high concentration of carbon dioxide found in the experimental tests) and a sort of steam reforming (which would have partly increased the hydrogen and carbon-monoxide mole fractions). Anyways, it is clear how the model validation inevitably gets more and more difficult as air-infiltration phenomena become more important. This is a practical limitation due to the experimental setup itself, which may not always be removed because of the high temperatures at which SOFC use to work, capable to cause a very high thermal stress of sealing materials.

At last, Figure 57 and Figure 58 present a comparison between experimental and model results when varying the FU factor and the current load. On one hand, Figure 57 shows what happens when carbon dioxide-to-biogas ratio is set to 1.5, FU factor is 50%, and the current load is 25 A (methane mass flow rate is set to 88 Nml/min in order to reach the latter conditions). On the other hand, Figure 58 shows the exhaust composition when carbon dioxide-to-biogas ratio is set to 1.5 again (it is kept constant in such a way to investigate the influence of both the current load and the FU factor), FU factor is 25%, and the current load is 15 A (methane mass flow rate must be set to 106 Nml/min).

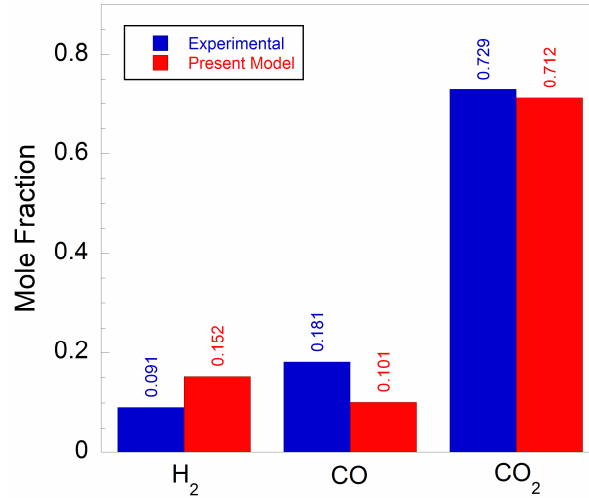


Figure 57. Mole-fraction comparison for main dry-gas species when carbon dioxide-to-biogas ratio is set to 1.5 ($I = 25 A$, $FU = 50\%$).

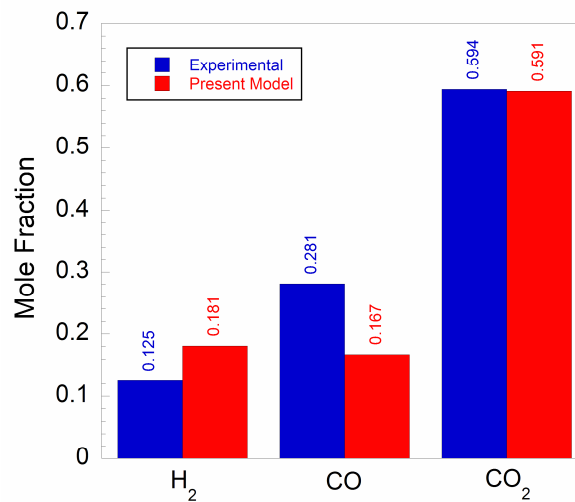


Figure 58. Mole-fraction comparison for main dry-gas species when carbon dioxide-to-biogas ratio is set to 1.5 ($I = 15 A$, $FU = 25\%$).

The match between experimental and model results is almost perfect for carbon dioxide, quite good for hydrogen (errors are little higher than 5%), while there is a significant mismatch for

carbon monoxide. All considerations made above remain valid for these two cases. In fact, methane final content is 3% and 5.6%, respectively, while water production (due to electrochemistry) leads to percentage volumes of 14.93% and 6.92%, respectively. Since nitrogen mole fractions (2.32% and 2.50%, respectively) are quite low, and considering the relatively high water content for both cases, we can state that the discrepancies in the hydrogen and, most of all, carbon-monoxide mole fractions are probably due to the fact that the mechanism file tends to encourage water gas-shift over dry-reforming and steam-reforming processes, so that carbon monoxide in the presence of water is mostly converted into carbon dioxide.

Comparing Figure 57 to Figure 55, it is easy to see the experimental effect of current on the fuel-cell emissions when carbon dioxide-to-biogas ratio is set to the intermediate value of 1.5, since it is clear how hydrogen and carbon-monoxide productions are slightly increased (around 0.5%) as the current load passes from 15 A to 25 A, while carbon-dioxide emission is slightly decreased (around 1%). Although a current rise should cause hydrogen and carbon monoxide to be consumed because of the electrochemical request, when setting such a low fuel mass flow rate, residence time may be considerably increased (with dry-reforming reactions having much more time to occur) and may lead to a general improvement in the conversion process, and thus to a better fuel utilization. On the contrary, when increasing the fuel mass flow rates, experimental results should clearly show the opposite trend.

Comparing Figure 58 to Figure 55, we can see the same effect as that of current rise when the FU factor is varied from 50% to 25% (however, this time hydrogen and carbon-monoxide are increased by around 5% and 10%, respectively, while carbon dioxide is decreased by around 15%). This is again due to a better fuel utilization as the stoichiometric mass flow rate is approached. In fact, it is important to specify how hydrogen and carbon dioxide are the expected dry-reforming products, while carbon dioxide comes from other chemical processes (combustion of methane, water gas shift, carbon-monoxide breakdown in the presence of oxygen, and so on) occurring inside the anode channel.

6.2.5 Mole-Fraction Profiles

Figure 59 and Figure 60 show the predicted mole-fraction profiles of main chemical species along the fuel channel (which is considered to be one-dimensional) for two different OCV cases. Methane mass flow rate is 50 Nml/min, while carbon dioxide-to-biogas ratio is 1 and 1.5, respectively.

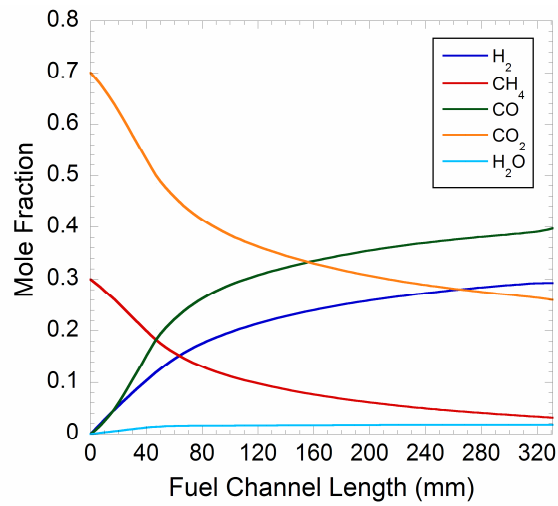


Figure 59. Predicted mole-fraction profiles of main chemical species when carbon dioxide-to-biogas ratio is set to 1 (OCV configuration).

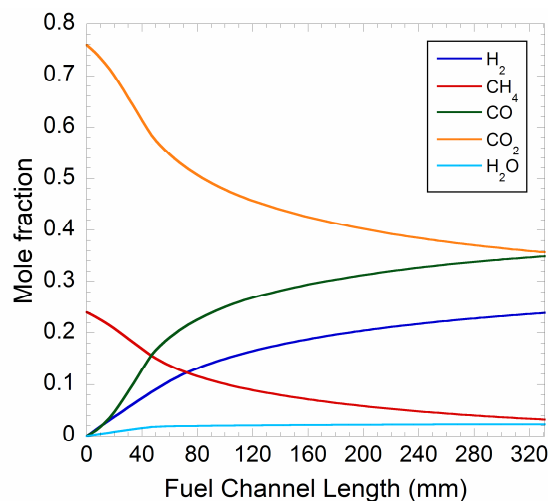


Figure 60. Predicted mole-fraction profiles of main chemical species when carbon dioxide-to-biogas ratio is set to 1.5 (OCV configuration).

For both cases, it is easy to see the quick consumption of methane and carbon dioxide in order to produce hydrogen and carbon monoxide. Also, a small amount of water is produced, and this is probably due to the inverse water gas-shift reactions. Either way, chemical equilibrium is approached but not achieved, even if dry reforming seems to proceed very quickly, especially in the first half of the fuel channel.

Figure 61 shows the predicted mole-fraction profiles of main chemical species along the fuel channel when a current load of 15 A is applied to the cell. Methane mass flow rate is 53 Nml/min and FU factor is 50%, while carbon dioxide-to-biogas ratio is set to 1.

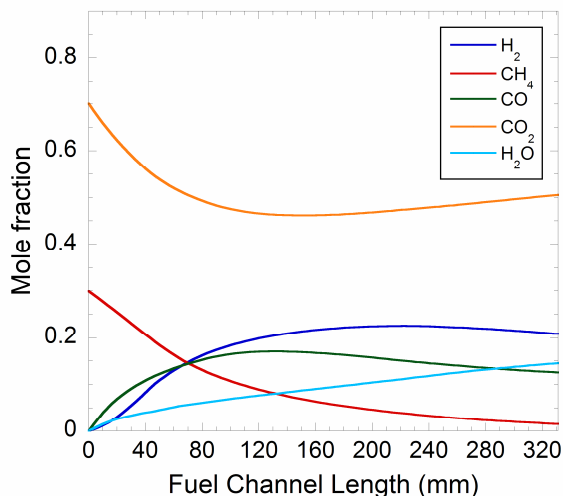


Figure 61. Predicted mole-fraction profiles of main chemical species when carbon dioxide-to-biogas ratio is set to 1 ($I = 15$ A, $FU = 50\%$).

Here, a quite large amount of water is produced because of the electrochemistry of the cell. This is the reason why carbon monoxide is slightly consumed in the last part of the cell, in order to form carbon dioxide when reacting with water (whose trend remains monotone because of its continuous electrochemical production). This particular tendency is due to the apparent dominance of direct water gas-shift reactions over dry- and steam-reforming processes in the mechanism file for given conditions (even if hydrogen content decreases as the channel exit is approached, suggesting the contemporary presence of different chemical processes). Anyway, balances between all chemical processes involved in a mechanism file are usually extremely difficult to be established (because of the overall file complexity), but they can provide researchers with interesting assumptions in order to better investigate the overall cell chemical behavior.

6.3 Steam Reforming

Steam-reforming experimental tests have been performed by setting the cell temperature to 800, 750, and 700°C, respectively. Reference composition for biogas (60% of methane and 40%

of carbon dioxide) was kept fixed, and the cell behavior was investigated for different steam-to-biogas molar ratios, which are 0.3, 0.4, 0.5, and 0.6, respectively (steam-to-methane ratios are 1.17, 1.33, 1.5, and 1.67, respectively).

6.3.1 Polarization curves

Polarization tests have been performed by following the same procedure described for dry-reforming experimental sessions. This procedure was repeated for several fuel mass flow rates, for each steam-to-biogas ratios, and for different cell temperatures.

Figure 62 presents the polarization curves, showing how the cell voltage and electrical power vary as functions of the current density, when the cell temperature is set to 800°C and the steam-to-biogas ratio is set to 0.3. Methane mass flow rates vary from 100 Nml/min to 400 Nml/min. Since we know biogas composition and steam addition, it is easy to compute carbon-dioxide and steam mass flow rates, which are not reported on plots.

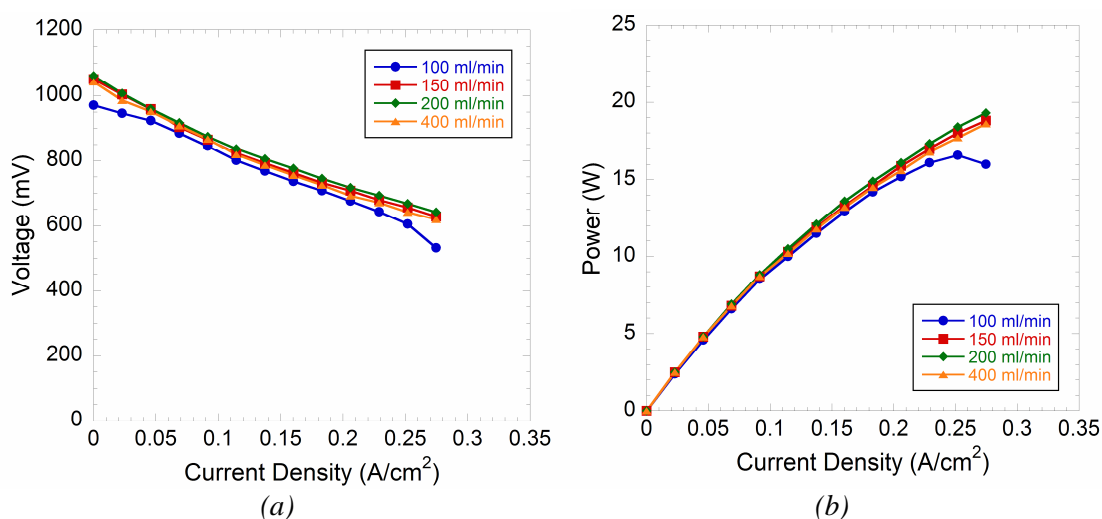


Figure 62. Polarization curves for different methane mass flow rates when steam-to-biogas ratio is set to 0.3 ($T = 800^{\circ}\text{C}$).

The trend of all curves is the same, with Ohmic losses being predominant when current density reaches relatively high values. Power maximum peak is appreciable only for the lowest methane mass flow rate. In order to show the other power peaks, it would be necessary to further increase the current load (because of the relatively high mass flow rates applied for this test), but this would cause the cell voltage to dramatically fall down. This is again a practical limitation (due to the mass flow controllers) which cannot be easily removed. Best performances are achieved for high methane mass flow rates, and this is due to the achievement of a lower fuel utilization factor. In particular, voltage (and consequently power) grow until methane mass flow rates of 200-250 Nml/min are reached. After this threshold, voltage and power asymptotically converge to the same value (even if the 400-Nml/min curve seems to stay below the previous two).

Similarly to what happens for dry reforming, experimental errors may strongly affect the performance of the tubular cell during steam-reforming tests depending on the day of use.

6.3.2 Influence of Steam Addition

Figure 63 shows the trend of the cell voltage and the electrical power as functions of the current density when methane mass flow rate is fixed and set to 100 Nml/min, and the cell temperature is 800°C. Steam-to-biogas ratios are 0.3, 0.4, 0.5, and 0.6, respectively. Then, Figure 64 and Figure 65 show the trend of the same quantities for the same conditions, except for the cell temperature, which is 750°C and 700°C, respectively. Maximum peaks are quite appreciable in the power plots only for the lowest steam-to-biogas ratios (0.3 and 0.4) because of the excessive voltage drop at high current, but it is easy to see how the trend is generally the same for all curves.

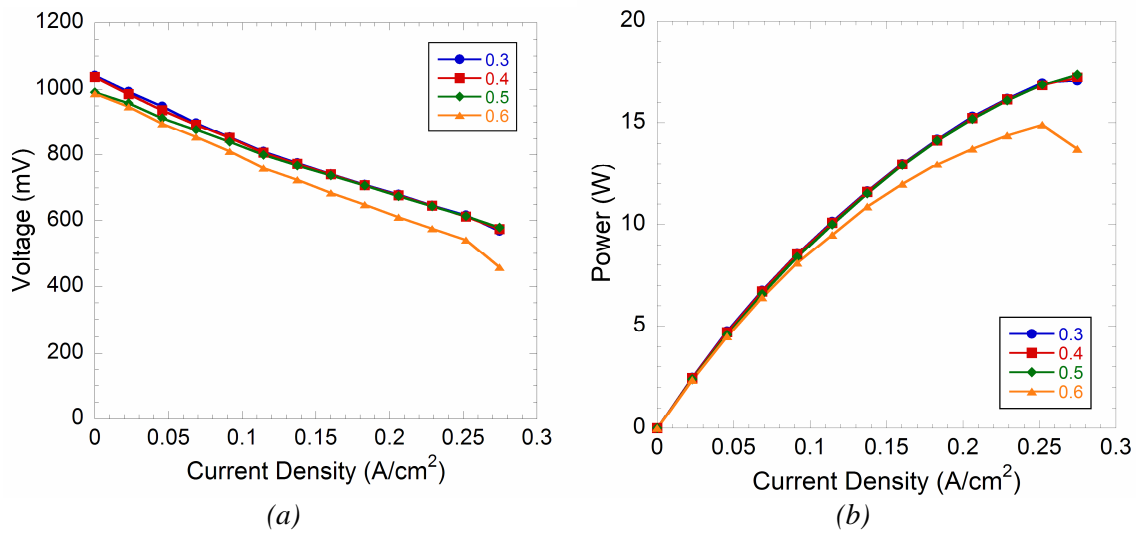


Figure 63. Polarization curves for different steam-to biogas ratios when methane mass flow rate is set to 100 Nml/min ($T = 800^{\circ}\text{C}$).

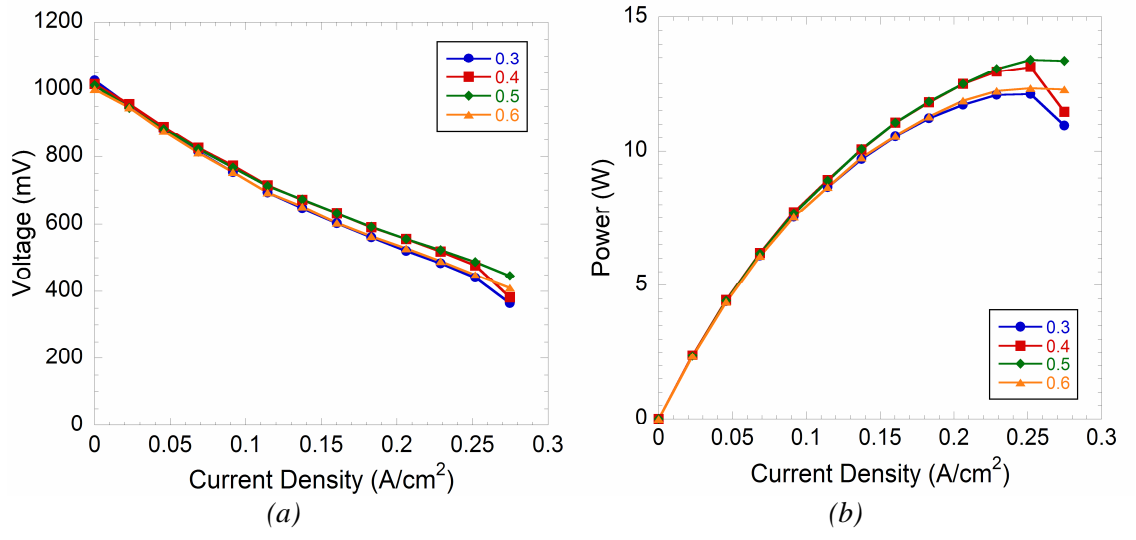


Figure 64. Polarization curves for different steam-to biogas ratios when methane mass flow rate is set to 100 Nml/min ($T = 750^{\circ}\text{C}$).

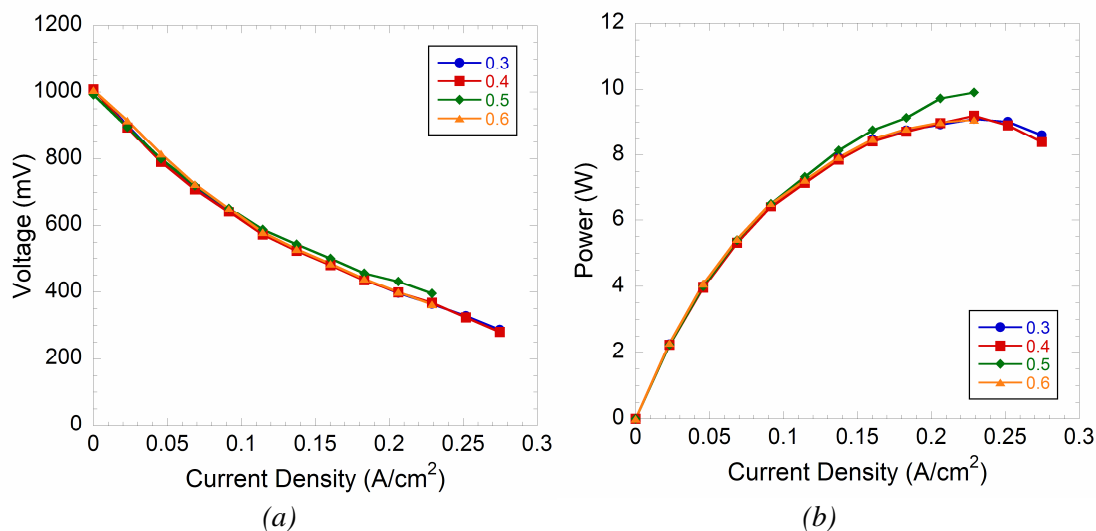


Figure 65. Polarization curves for different steam-to biogas ratios when methane mass flow rate is set to 100 Nml/min ($T = 700^\circ\text{C}$).

Best performances are achieved when steam-to-biogas ratio is set to 0.5 at each temperature. However, considering any possible experimental error, voltage and power values seem to be quite the same for each steam-to-biogas ratio except for the 0.6-case. The latter ratio seems to provide much lower voltage and power only for the 800°C -case (it is important to specify that the tubular SOFC employed for the present work is designed to work around 800°C), with discrepancies between the curves being less important at lower temperatures. In particular, at 750°C all curves are close until the current density does not reach high values, while at 700°C only the 0.5-curve (whose shape suggests however the presence of experimental errors) stays much above the others. Hence we can say that steam reforming seems to be more effective when steam-to-biogas ratio is low (from 0.3 to 0.5 we cannot see appreciable differences for each temperature case). At 800°C a ratio of 0.6 may lead to very low performances, while steam-to-biogas ratio seems to be generally less effective as the cell temperature decreases, with all curves getting closer to each other. This can be due to the presence of carbon dioxide in the fuel, which may take part in possible dry-reforming processes. Then it is clear how dry reforming may take over steam-

reforming effectiveness, and this makes extremely difficult a complete investigation of biogas steam reforming (considering the experimental setup available). We can suppose that a combination of dry- and steam-reforming processes occur inside the fuel channel; however, we cannot easily say which process is predominant. Again, an exhaust gas-analysis may be useful to partly explain what chemically happens on the anode side.

6.3.3 Influence of Cell Temperature

Figure 66 is reported to show how the cell voltage and the electrical power vary as functions of the current density when the cell temperature is set to 800, 750, and 700°C, respectively. Methane mass flow rate is set to 100 Nml/min, while steam-to-biogas ratio is 0.3. The following plots are taken from Figure 63 through Figure 65 and put together in order to easily show off the cell-temperature effect.

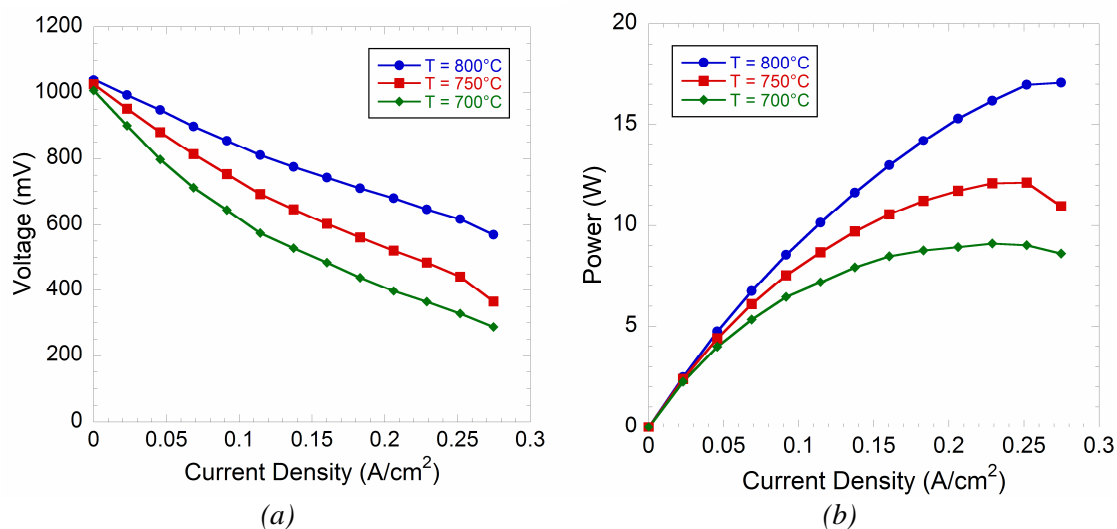


Figure 66. Polarization curves for different cell temperatures when methane mass flow rate is set to 100 Nml/min (steam-to-biogas ratio is set to 0.3).

Power maximum peaks are more appreciable as the cell temperature decreases, but it is extremely clear how performances generally get lower as the cell temperature gets further away from the design temperature, which is around 800°C as we said in the previous paragraph. Also, maintaining an excessively low cell temperature for hours may lead to irreversibly damage the cell, since its electrochemistry could turn out to be not fully activated.

6.3.4 Fuel Utilization Map

A fuel utilization map has been drawn by following the same procedure described for dry-reforming tests, starting from a current load of 10 A and methane mass flow rates correspondent to an FU of 20%. The procedure was repeated by increasing the current load by 2.5 A until a maximum of 30 A.

Figure 67 presents the relation existing between the cell efficiency and the electrical power produced by the cell. Steam-to-biogas ratio is set to 0.3, while the cell temperature is 800°C . Again, lines of the same color connect operational points characterized by the same current load, while black lines, generally presenting a slight negative slope, combine points with the same FU.

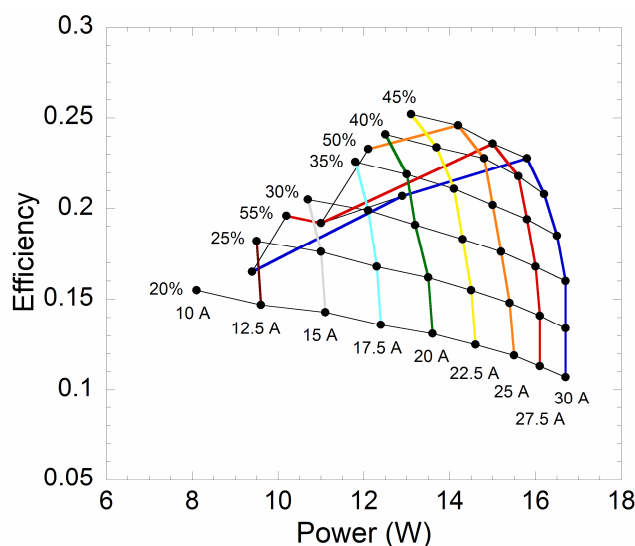


Figure 67. Efficiency map when steam-to-biogas ratio is set to 0.3 ($T = 800^{\circ}\text{C}$).

As shown in dry-reforming efficiency maps, at constant FU, efficiency decreases when the current applied to the cell is increased because of Ohmic losses (which get particularly strong and heavy from 25 A on) due to current collection. A strong limitation in drawing the previous map was the impossibility to decrease the fuel mass flow rates at both low and high current, in such a way to get more data points and relatively high FU factors. In fact, by decreasing fuel mass flow rates it would be possible to generally raise efficiency and to visualize efficiency peaks at lower current loads (efficiency peaks are appreciable only at 25, 27.5, and 30 A, with the last two cases being strongly affected by Ohmic losses when increasing the FU factor).

Maximum efficiency (on LHV basis), which is 25.2%, is achieved when FU factor is 45%, current load is 22.5 A, electrical power is 13.1 W, and methane mass flow rate is 87.1 Nml/min. The latter rate is almost twice as the minimum rate employed when performing dry-reforming tests, and this is now due to the lower limit of the carbon-dioxide mass flow controller, since carbon-dioxide mass flow rates are always lower than those of methane when performing steam reforming tests.

It is clear how efficiency is very low if compared to the values found when performing dry reforming. However, we cannot easily state that dry reforming is more efficient than steam reforming, because of the combination of these two processes probably occurring inside the anode channel. When considering a type of biogas with this specific composition, i.e., containing a large amount of carbon dioxide, it would be very interesting to increase the steam-to-biogas ratio (but this is not an easy operation since methane is humidified by passing through a bubbler, whose temperature must be contained in a specific safety-margin range; moreover, large amounts of vapor may cause water to condense inside the inlet pipe before entering the cell), in order to ensure the dominance of steam reforming over dry reforming and to better investigate the effects of the former on the cell behavior.

6.3.5 Gas Analysis and Model Validation

While performing gas-chromatograph analysis for steam-reforming tests, the tubular cell has been strongly affected by an exhaust-gas leak occurring in the final part of the fuel channel, where the latter is connected to the outlet pipe. Here, the application of a ceramic paste, which is thermally resistant to temperatures up to 1287°C, should guarantee the perfect sealing of the junction during the cell operation. However, the ceramic paste is not easy for the operator to apply (and this does not completely guarantee the absence of leakage itself) and, also, the sealing may damage after an excessive number of startups and shutdowns. While performing steam-reforming tests, a small flame was clearly visible inside the furnace in correspondence of the zone described above.

All analyzed samples presented very high amounts of nitrogen (varying from 18.3% to 45.6%), with oxygen being always under the gas-chromatograph detection limit (1%). This practically means that, if air enters the fuel channel, a quite large amount of oxygen is free to react with the exhaust gases, with the final composition being heavily affected by experimental errors. For this reason, only two cases are reported here in order to provide a qualitative description of the products arising from steam-reforming processes when running in OCV configuration, without any pretension to effectively validate the model implemented in the present work.

Figure 68 and Figure 69 show the comparison between model and experimental results when no current load is applied to the cell, steam-to-biogas ratio is 0.3 and the cell temperature is set to 800°C. Methane mass flow rates are 150 and 200 Nml/min, respectively. Nitrogen concentrations (25.6% for Figure 68 and 18.3% for Figure 69) have been removed from the experimental data, while water content (under 1.5% for both cases) has been neglected in the final-composition mole fractions computed by the model. Consequently, mole-fraction normalizations were carried out as before. It is important to specify that high amounts of methane (7.8% and 9.6%, respectively) were found by the model in the final composition, and this may

result steam reforming to be less effective than dry reforming (which generally keeps unexploited-methane mole fractions under 5%) in converting methane.

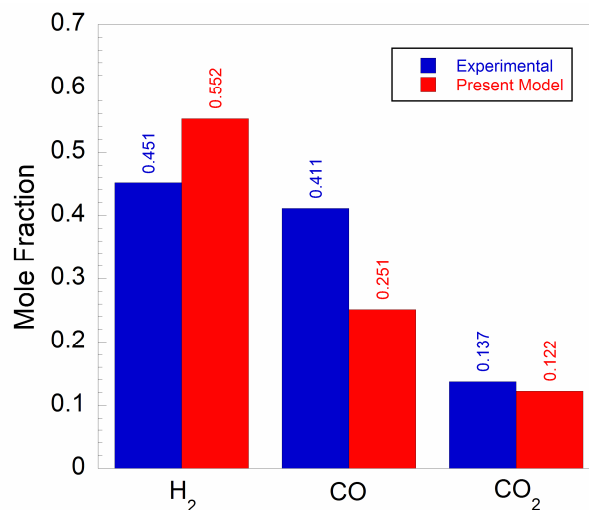


Figure 68. Mole-fraction comparison for main dry-gas species when methane mass flow rate is set to 150 Nml/min (steam-to-biogas ratio equal to 0.3, OCV configuration, $T = 800^{\circ}\text{C}$).

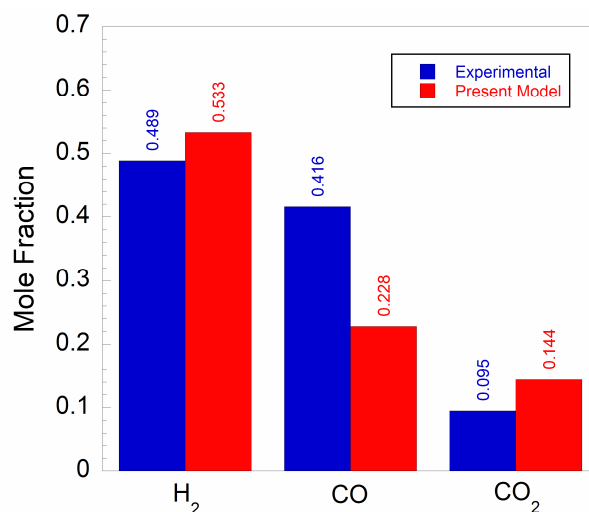


Figure 69. Mole-fraction comparison for main dry-gas species when methane mass flow rate is set to 200 Nml/min (steam-to-biogas ratio equal to 0.3, OCV configuration, $T = 800^{\circ}\text{C}$).

As expected (considering the high nitrogen concentration in the exhaust composition), the match between the model and the experimental data is quite bad. This is certainly due to an excessive air infiltration inside the furnace, which may cause alternative reactions to occur and may somehow shift chemical balances. A shy attempt to explain what happens inside the cell may be the following: air is free to enter the fuel channel, where a relatively high amount of oxygen is free to burn down methane (not found by the gas-chromatograph) and hydrogen (whose actual concentration is much lower than the one computed by the model in the 150-Nml/min case), methane combustion leads to high carbon-monoxide mole fractions (presenting the highest errors up to 18.8% for the 200-Nml/min case), and carbon-dioxide production is again the result of the balance existing between the different chemical processes occurring inside the channel (dry and steam reforming, methane combustion, carbon-monoxide breakdown, and water gas shift). Since this explanation may be chemically consistent, gas-analysis data cannot effectively validate the model for the steam-reforming case.

6.3.6 Mole-Fraction Profiles

Figure 70 shows the predicted mole-fraction profiles of main chemical species along the fuel channel for a particular OCV case. Methane mass flow rate is 200 Nml/min, the cell temperature is 800°C, and the steam-to-biogas ratio is set to 0.3. Although the final composition for given conditions cannot be validated by the experimental data, it is interesting to see how water is completely consumed in the first half of the channel (and this fact, together with the high amount of residual methane, could mean that steam-to-biogas ratio needs to be strongly increased in order to ensure a more effective and complete steam-reforming process), with hydrogen and carbon monoxide being quickly produced in the same region. Carbon dioxide is consumed as well, and its monotone trend suggests that dry and steam reforming may occur together in the first part of the channel until water is totally gone.

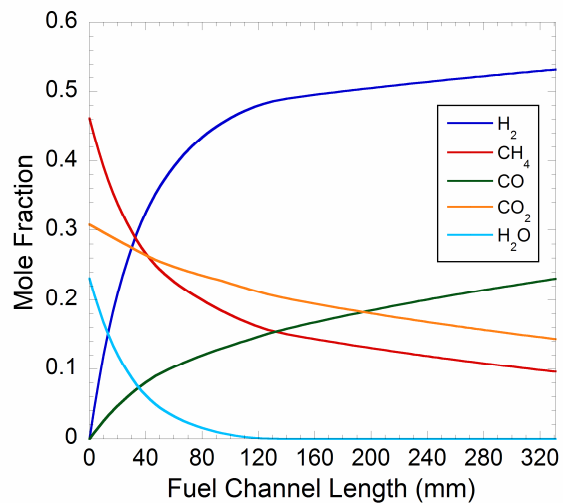


Figure 70. Predicted mole-fraction profiles of main chemical species when methane mass flow rate is set to 200 Nml/min (steam-to-biogas ratio equal to 0.3, OCV configuration, $T = 800^{\circ}\text{C}$).

Due to the experimental errors occurred when performing steam-reforming tests, no direct efficiency or performance comparison between dry- and steam-reforming processes is reported in the present work.

CHAPTER 7

PERFORMANCE COMPARISON FOR PPF AND SOFC PROCESSES

The following chapter presents a brief performance comparison between the two different energy pathways analyzed in the present work. In particular, PPF combustion and SOFC dry reforming are the main aspects that have been considered in order to build up a comparison based on the heat generation per unit mass of fuel. Fuel composition is fixed for both processes and represents the simplified biogas mixture used for the previous SOFC study (i.e., 60% of CH₄ and 40% of CO₂, in volume or molar terms).

On one hand, when considering PPF combustion, the heat generation per unit mass of biogas is computed for the four cases listed in Table IX. Distance between the nozzles is 2 cm, pressure is 1 atm, and the inlet temperature is set to 300 K for both the fuel and the oxidizer streams. The equivalence ratio at the fuel nozzle is set to 1.4 and 3.0, respectively, while the strain rate is set to 150 and 200 s⁻¹, respectively, and all possible combinations are made. Here, the heat generation per unit mass of fuel is computed as the ratio between the heat generation rate (given in W/cm²) and the normalized biogas mass flow rate (given in g/cm²/s). The heat generation rate is computed by integrating the heat flux (which is included in simulation results and is initially given in erg/cm³/s as a function of the distance between the nozzles) along the axial coordinate, while the biogas mass flow rate is computed by first calculating the normalized mass flow rate of the mixture at the fuel nozzle (which is the product between the axial velocity and the density of the mixture at the fuel nozzle) and by then extracting the biogas mass flow rate knowing the equivalence ratio at the fuel nozzle.

On the other hand, when studying SOFC dry-reforming processes, the heat generation per unit mass of fuel may be easily computed by exploiting the experimental data used to draw polarization curves. In fact, that is computed as the ratio between the peak electrical power and the biogas mass flow rate entering the anode channel. The latter rate is computed as the product

between the volume flow rate known a priori and the density of the biogas mixture, which can be easily computed by *Cantera* after defining the mixture composition and temperature. Four different cases are considered and listed in Table XII. CO₂/biogas ratio is set to 1 and 1.5, respectively, while CH₄ mass flow rate is set to 60, 80, and 130 Nml/min, respectively.

TABLE XII. LIST OF DRY-REFORMING COMBINATIONS

Case	CO ₂ /Biogas Ratio	CH ₄ Mass Flow Rate (Nml/min)
1	1	60
2	1	80
3	1	130
4	1.5	60

Table XIII shows the heat generation per unit mass of biogas (in J/g) for both the PPF and the SOFC cases. It is clear how SOFCs seem to exploit biogas much more effectively than PPFs. Generally, the PPF heat generation increases as the equivalence ratio approaches the stoichiometric conditions, with strain rates of 150 s⁻¹ providing a better fuel utilization than with 200 s⁻¹, while the SOFC heat generation (and thus the efficiency, as pointed out in the previous chapters) increases for lower fuel mass flow rates and for CO₂/biogas ratios which are close to unity. In particular, the peak heat generation for SOFCs (case 1) is over four times higher than the one for PPFs (case 1). However, this is partly due to the different nature of the two processes (chemical and electrochemical). In fact, while the heat generation is a proper energy production when considering PPFs (and the temperature rise is due to the chemical reactions occurring between the fuel and the oxidizer), the heat-generation values computed for the SOFC cases represent a virtual energy production extracted from the electrical power (no proper heat is produced, temperature is kept constant by the furnace where the cell is immersed, and power is a

consequence of the current flow arising from the electrochemical reactions occurring inside the cell).

TABLE XIII. HEAT GENERATION PER UNIT MASS OF BIOGAS

Case	Heat Generation per Unit Mass of Biogas (J/g)
PPF 1	1902.0
PPF 2	692.9
PPF 3	1561.5
PPF 4	585.5
SOFC 1	8159.6
SOFC 2	6699.5
SOFC 3	4873.5
SOFC 4	7563.7

Despite the issues linked to the nature of the governing reactions, Table XIII provides significant information on the effectiveness of one of the current up-and-coming electrochemical ways to produce energy. In fact, the tubular SOFC technology is capable to provide the user with high performances and efficiencies (compared to the traditional energy conversion systems) when fed by low fuel mass flow rates.

CHAPTER 8

CONCLUSIONS

Biogas remains an interesting alternative for both chemically and electrochemically producing energy, by providing multiple advantages from different viewpoints.

An extensive simulation analysis on biogas combustion has been performed by using the software *CHEMKIN*, in order to make a comparison between two different types of biogas (produced by exploiting agrifood-industry and household waste, respectively) and methane.

An equilibrium composition study shows that both biogases may reasonably decrease carbon-monoxide and nitrogen-oxides production by increasing carbon-dioxide emissions (however, it is important to specify that a large amount of carbon-dioxide is already contained in biogas initial compositions; hence emissions are not completely due to carbon-dioxide production). Also, both biogases guarantee an adiabatic-flame-temperature maximum peak which is slightly lower than that of biogas (around 200°C below). Main contaminants (carbon dioxide, water vapor, nitrogen, and oxygen) are the main cause for the adiabatic flame temperature to drop (except oxygen, which helps the oxidation process to occur), with carbon dioxide having the strongest effect because of its high concentration.

A laminar-premixed-flames study may confirm that the combustion processes of both biogases can reach temperatures which are very close to that of methane, with temperature profiles (along the axial coordinate) being almost superimposed. Carbon-monoxide (together with all carbonaceous products except carbon dioxide) and nitrogen-monoxide production remain considerably lower for both biogases, while carbon-dioxide emissions stay higher. Nitrogen-dioxide mole-fraction profiles exhibit maximum peaks which are higher than that of methane for both biogases, but a NO_x -emission-index analysis points out how biogas emissions are generally lower than for the methane case. However, biogas flame speeds are considerably decreased if compared to that of methane, with biogas 2 showing a 37% drop (compared to methane) when

burning a stoichiometric air-fuel mixture at atmospheric pressure. Flame speed has been also investigated at elevated pressures (up to 50 atm), showing the same result. Flame-speed profiles (as functions of both equivalence ratio and pressure) and the overall-reaction-order trend (as a function of pressure) have been validated for the only methane case with experimental data taken from previous literature.

Eventually, a partially-premixed-flames study has been performed for different equivalence ratios (at the fuel nozzle) and strain rates, showing the same tendency for emissions, with concentrations of pollutants being considerably lower for both biogases. In particular, we can see a considerable drop of nitrogen-monoxide and soot production for all considered cases. Carbon-monoxide and nitrogen-dioxide emissions are also decreased, while carbon-dioxide concentrations remain once again higher than those of methane, due to biogas initial composition. Biogas flames look generally narrower than those of methane (as clearly shown by temperature profiles), while axial velocity feels a considerably high drop for both biogases. Analyzing the influence of both strain rate and equivalence ratio on the flame structure, it is easy to see that, as the strain rate increases, flames become narrower, peak temperatures decrease, axial velocity slightly raises, and emissions of pollutants slightly decrease, while, considering then the effect of equivalence ratio at the fuel nozzle, we see that, for richer mixtures, flames become much narrower, peak temperatures decrease, axial velocity dramatically falls down, and carbon-monoxide, soot, and nitrogen-oxides emissions dramatically raise. A stretched flame speed can be extracted by analyzing the maximum peaks of carbon-monoxide emissions, with biogas flame speeds being considerably lower than that of methane again. Flame-speed discrepancies between methane and both biogases become less important as the equivalence ratio at the fuel nozzle is increased (and, consequently, flame speed values fall down), while a strain-rate raise generally leads to lower flame-speed values. A performance outline may clearly point out how both biogases provide a considerably high peak heat flux when working with rich mixtures, while methane remains a much more effective solution for slightly rich mixtures. At last, a short

dilution study has been performed in order to show how carbon-dioxide dilution is favored (for both fuel-stream-dilution and air-stream-dilution cases) over nitrogen dilution because of the high carbon-dioxide content in biogas initial compositions. A strain-rate raise generally causes the stagnation point to occur at higher temperatures and lower carbon-dioxide or nitrogen mole fractions.

In the second part of this work, biogas has been investigated when directly feeding a tubular anode-supported SOFC. Several experimental tests have been performed at *Edison S.p.a.* – *Centro Ricerca e Sviluppo* for both dry- and steam-reforming sessions, in order to plot polarization curves and draw efficiency maps of the fuel cell. For both cases, polarization curves easily show that the best performances (due to high voltage and thus high electrical power) are achieved when fuel mass flow rates are increased (and current load does not overtake a certain threshold beyond which Ohmic losses are predominant) until maximum voltage values are asymptotically reached for different operational conditions. On the contrary, from an efficiency viewpoint, fuel utilization maps clearly show that the highest efficiencies are reached when fuel mass flow rates are set to very low values, with quite high fuel utilization factors and current loads. Dry-reforming tests, which have been performed for different carbon dioxide-to-biogas ratios, present higher efficiencies than the ones found for steam-reforming tests. This is certainly due to the actual effectiveness of dry-reforming processes (maximum efficiency is over 43% and is achieved when carbon dioxide-to-biogas ratio is set to unity), but a direct comparison between dry and steam reforming remains difficult to be made because of biogas composition, which implies the possibility for carbon dioxide in the fuel to be directly involved in the chemical processes occurring inside the anode channel.

When performing dry-reforming tests, the influence of carbon dioxide-to-biogas ratio has been studied, with best performances and efficiencies being achieved for a ratio set to unity, and this is again due to the fact that the actual carbon dioxide-to-methane ratio reaches values which are much higher than unity, thus favoring methane reforming to occur.

When performing steam-reforming tests, the influence of steam-to-biogas ratio has been studied at different cell temperatures (with temperature affecting more and more the cell performance as it turns away from the design value, which is set to 800°C), with discrepancies between curves correspondent to different ratios being relatively slight (however, 0.5 seems to be the best steam-to-biogas ratio in order to reach the highest performances at each cell temperature). This is probably due to the fact that what actually occurs inside the cell is a mix of dry- and steam-reforming processes, with the advantages arising from steam reforming being more difficult to appreciate. In order to better investigate the effectiveness of steam reforming, it would be useful to modify experimental conditions in such a way that increases both the steam-to-biogas and the steam-to-methane ratios. Moreover, all experimental limitations due to the lower limit of the mass flow controllers employed for the present work must be removed or alleviated in order to achieve higher fuel utilization factors and lower fuel mass flow rates, and thus to reach higher efficiencies.

An extensive gas-chromatograph analysis has been performed for both dry- and steam-reforming experimental sessions, in order to validate the numerical model implemented in the present work through *Cantera* and *MATLAB* for predicting the final composition of the anode exhaust gases and the mole-fraction profiles of main chemical species along the fuel channel. Results are quite acceptable for dry reforming, even though they have been affected by air infiltration occurring inside the furnace and in the final pipe, while they cannot be used to validate the model for the steam-reforming case, due to heavier air infiltration and massive exhaust-gas leakage inside the furnace. The match between dry-reforming model and experimental results is quite good and the model has been validated although infiltration and leakage phenomena were rather important. Eventually, mole-fraction profiles of main chemical species obtained by the model can confirm all theses made to explain the discrepancies between model and experimental data, by better showing the evolution of the chemical processes occurring inside the anode channel. Also, mole-fraction profiles, together with *CEA*-simulation

results, confirm that thermodynamic-equilibrium conditions are far from being achieved inside the channel.

Eventually, a performance comparison based on the computation of the heat generation per unit mass of biogas may show how SOFCs are capable to exploit biogas much more effectively than PPFs. However, this is partly due to the different nature of the two processes (chemical and electrochemical).

In conclusion, biogas may be an efficient alternative to conventional methane for both chemically and electrochemically producing energy. On one hand, when involved in combustion processes, biogas can offer good performances in terms of temperature, flame speed, and heat generation, by considerably breaking down the emissions of pollutants at the same time. On the other hand, when directly feeding solid oxide fuel cells, biogas can offer high efficiency and good performances in terms of voltage and electrical power, by effectively exploiting different fuel-reforming processes occurring inside the cell. It is crucial to specify once again that, for both energy pathways, high carbon-dioxide contents in the exhaust gases are due to the fact that biogas is a renewable fuel, and thus a large amount of the final carbon-dioxide concentration is a result of the biomass cycle itself and does not represent a new source of carbon extracted from the underground. In this sense, biogas presents all the characteristics to play a significant role in the future for both energy pathways, since it is an efficient alternative to both traditional hydrocarbon fuels, whose production appears to be doomed to end in a few decades, and hydrogen, whose production, storage, and use are currently affected by high costs.

APPENDICES

Appendix A

This appendix contains the implementation on *MATLAB* and *Cantera* (.m file extension) of the electrochemical model employed for predicting mole-fraction profiles of main chemical species inside the anode channel of a tubular SOFC and the mechanism file (*nickel.cti*) for methane reforming kinetics within a Ni/YSZ SOFC anode support in *CHEMKIN* format, which is taken from reference [52], together with its translation in *Cantera* format.

Here is reported the *MATLAB* script:

```
clear all;
close all;
clc;

% Parameters

p = oneatm; % pressure
t = 1073.15; % temperature (K)

transport = 'Mix';
gas = importPhase('nickel.cti','gas');

names = SpeciesNames(gas);
Wi = molecularWeights(gas)'; % kg/kmol
t_amb = 273.15;
conc0 = p/(gasconstant*t_amb); % concentration (kmol/m^3)

current = 0; % [A]

CH4_flow = 0.200; % [l/min]
CO_flow = 0;
CO2_flow = 0.133;
N2_flow = 0;
O2_flow = 0;
H2_flow = 0;
Ar_flow = 0;
humid_percent = 0.5;

% Geometry

R_channel = 0.00525; % [m]
channel_length = 0.331; % [m]
anode_thickness = 0.0017; % [m]
axial_subdivision = 50; % cells
radial_subdivision = 8; % points

shape_function = ones(1,axial_subdivision);
% shape_function = linspace(axial_subdivision,1,axial_subdivision);
% shape_function = linspace(1,axial_subdivision,axial_subdivision);
shape_function = shape_function/sum(shape_function);
shape_current = current*shape_function;
molar_flow = zeros(1,max(size(names))); % kmol/s
```

Appendix A (continued)

```

molar_flow(12) = CH4_flow/60/1000*conc0; % kmol/s
molar_flow(13) = CO_flow/60/1000*conc0;
molar_flow(14) = CO2_flow/60/1000*conc0;
molar_flow(1) = H2_flow/60/1000*conc0;
molar_flow(4) = O2_flow/60/1000*conc0;
molar_flow(16) = N2_flow/60/1000*conc0;
molar_flow(17) = Ar_flow/60/1000*conc0;
H2O_flow = molar_flow(12)*humid_percent;
molar_flow(6) = H2O_flow;

total_flow = sum(molar_flow); % kmol/s
X0 = molar_flow/total_flow; % mole fractions
W0 = sum(X0.*Wi);
total_mass_flow = total_flow*W0; % kg/s

comp = '';

for m=1:max(size(names))
    comp = [comp cell2mat(names(m)) ':' num2str(X0(m)) ', '];
end

comp = comp(1:end-2);

results = zeros(max(size(names)),axial_subdivision+1);
results(:,1) = X0';
results_prime = zeros(max(size(names)),axial_subdivision);

cell_length = channel_length/axial_subdivision;
initial_grid = linspace(0,R_channel,radial_subdivision); % m
axial_grid = linspace(0,channel_length,axial_subdivision+1); % m
A_inlet = pi*R_channel^2;
A = 2*pi*(R_channel+anode_thickness)*cell_length; % reacting-surface area

tol_ss = [1.0e-5 1.0e-9]; % [rtol atol] for steady-state problem
tol_ts = [1.0e-3 1.0e-9]; % [rtol atol] for time stepping
loglevel = 0;
printfigures = 1; % 1 to enable printing, 0 to disable
refine_grid = 1; % 1 to enable refinement, 0 to disable

molar_flow0 = molar_flow;
wdot_current = zeros(1,max(size(names)));

clear gas;

for j=1:axial_subdivision
    gas = importPhase('nickel.cti','gas');
    current_induced_mass_flow = sum(wdot_current.*Wi);
    total_mass_flow = total_mass_flow + current_induced_mass_flow;
    mdot = total_mass_flow/A_inlet;

    % gas object
    set(gas, 'T', t, 'P', p, 'X', comp);

    % interface object
    surfl = importInterface('nickel.cti','Ni_surf', gas);
    setTemperature(surfl, t);

    % integrate the coverage equations in time for 1 s, holding the gas
    % composition fixed to generate a good starting estimate for the

```

Appendix A (continued)

```

% coverages
advanceCoverages(surfl, 1.0);
% create the flow object
f = AxisymmetricFlow(gas, 'flow');
set(f, 'P', p, 'grid', initial_grid, 'tol', tol_ss, 'tol-time', tol_ts);

% create the inlet
inlt = Inlet('inlet');
set(inlt, 'T', t, 'MassFlux', mdot, 'X', comp);

% create the surface
surf = Surface('surface', surfl);
setTemperature(surf, t);

% create the stack
simlD = Stack([inlt, f, surf]);

% set the initial profiles.
setProfile(simlD, 2, {'u', 'T', 'V'}, [0.0          1.0      % z/zmax
                                     0.06         0.0      % u
                                     t             t       % T
                                     0.0          0.0]);

for k = 1:nSpecies(gas)
    y = massFraction(inlt, k);
    setProfile(simlD, 2, names{k}, [0 1; y y]);
end

% start with the energy equation on
enableEnergy(f);

% disable the surface coverage equations, and turn off all gas and
% surface chemistry
setCoverageEqs(surf, 'off');
setMultiplier(surfl, 0.0);
setMultiplier(gas, 0.0);

% solve the problem, refining the grid if needed
solve(simlD, loglevel, refine_grid);

% set more stringent grid refinement criteria
setRefineCriteria(simlD, 2, 100.0, 0.15, 0.2);

% now turn on the surface coverage equations, and turn the
% chemistry on slowly
setCoverageEqs(surf, 'on');

for iter=1:6
    mult = 10.0^(iter - 6);
    setMultiplier(surfl, mult);
    setMultiplier(gas, mult);
    solve(simlD, loglevel, refine_grid);
end

if printfigures == 1
    figure(j)
    clf;
    subplot(3,3,1);

```

Appendix A (continued)

```

plotSolution(sim1D, 'flow', 'T');
title('Temperature [K]');
subplot(3,3,2);
plotSolution(sim1D, 'flow', 'u');
title('Axial Velocity [m/s]');
subplot(3,3,3);
plotSolution(sim1D, 'flow', 'CH4');
title('CH4 Mass Fraction');
subplot(3,3,4);
plotSolution(sim1D, 'flow', 'CO');
title('CO Mass Fraction');
subplot(3,3,5);
plotSolution(sim1D, 'flow', 'CO2');
title('CO2 Mass Fraction');
subplot(3,3,6);
plotSolution(sim1D, 'flow', 'H2O');
title('H2O Mass Fraction');
subplot(3,3,7);
plotSolution(sim1D, 'flow', 'H2');
title('H2 Mass Fraction');
subplot(3,3,8);
plotSolution(sim1D, 'flow', 'V');
title('Radial Velocity [1/s]');
end

% Rates computation

wdot_surf = netProdRates(surf1);           % kmol/m^2/s
wdot_surf = wdot_surf(1:max(size(names)));
wdot_surf = wdot_surf*A;                   % kmol/s

wdot_current(1) = -shape_current(j)/(2*Faraday); % [kmol/s]
wdot_current(6) = shape_current(j)/(2*Faraday); % [kmol/s]
molar_flow = molar_flow + wdot_surf + wdot_current; % kmol/s

for m=1:max(size(names))
    if molar_flow(m) < 0;
        molar_flow(m) = 0;
    end
end

total_flow = sum(molar_flow);
X = molar_flow/total_flow; % final composition
W = sum(X.*Wi);
total_mass_flow = total_flow*W;
results(:,j+1) = X'; % mole-fraction profiles

for m=1:max(size(names))
    profile = writeSolution(sim1D, 'flow', cell2mat(names(m)));
    results_prime(m,j) = profile(end); % mass-fraction profiles
end

comp = '';

for m=1:max(size(names))
    comp = [comp cell2mat(names(m)) ':' num2str(X(m)) ', '];
end

comp = comp(1:end-2);

```

Appendix A (continued)

```

clear sim1D;
clear surfl;
clear f;
clear inlt;
clear surf;

end

```

Here is reported the function called *writeSolution*:

```

function [x,z] = writeSolution(s, domain, component)

n = domainIndex(s,domain);
d = s.domains(n);
z = gridPoints(d);
x = solution(s, domain, component);

```

Here is reported the mechanism file in *CHEMKIN* format:

```

!SURFACE MECHANISM OF CH4 REFORMING AND OXIDATION OVER NI
!*****
!****
!****      CH4 ON Ni - SURFACE MECHANISM
!****
!****
!****      Version 1.2  (March 2006)
!****
!****      L. Maier, V. Janardhanan, B. Schaedel, O. Deutschmann
!****      ITCP, University of Karlsruhe, Germany
!****      Contact: mail@detchem.com (O. Deutschmann)
!****
!****      NOTE: That is a first version that needs further
!****            improvements,
!****            e.g. NiO formation, coking,
!****            temp. range 500-2000°C
!****
!****      References:
!****      L. Maier, B. Schaedel, S. Tischer, O. Deutschmann,
!****            submitted to Catal. Lett.

```

Appendix A (continued)

```

!**** V.M. Janardhanan, O. Deutschmann.
!**** Journal of Power Sources 162 (2006), 1192-1202
!**** Zeitschrift f. Phys. Chem. 221 (2007) 443-479
!**** www.detchem.com/mechanisms
!****
!**** Kinetic data:
!**** k = A * T**b * exp (-Ea/RT)          A          b          Ea
!****                                     (cm,mol,s)  -          J/mol
!****
!**** Surface site density: 2.66E-9 mol/cm**2
!****
!**** (SURFACE CHEMKIN format)
!****
!*****
SITE      /NI_surface/   SDEN /2.66E-09/
  NI(s)           /1/
  H2O(s)          /1/
  H(s)            /1/
  OH(s)           /1/
  CO(s)           /1/
  C(s)            /1/
  CH3(s)          /1/
  CH2(s)          /1/
  CH(s)           /1/
  CH4(s)          /1/
  O(s)            /1/
  CO2(s)          /1/
  HCO(s)          /1/
END
THERMO ALL
  300.0  1000.0  5000.0
CH4      (adjust)  C  1H  4  0  0  300.00  5000.00  1000.00  1
1.68347883E+00  1.02372356E-02-3.87512864E-06  6.78558487E-10-4.50342312E-14  2
-1.00807871E+04  9.62339497E+00  7.78741479E-01  1.74766835E-02-2.78340904E-05  3
3.04970804E-08-1.22393068E-11-9.82522852E+03  1.37221947E+01  4
H2      (adjust)  H  2  0  0  0  300.00  5000.00  1000.00  1
3.06670950E+00  5.74737550E-04  1.39383190E-08-2.54835180E-11  2.90985740E-15  2
-8.65474120E+02-1.77984240E+00  3.35535140E+00  5.01361440E-04-2.30069080E-07  3
-4.79053240E-10  4.85225850E-13-1.01916260E+03-3.54772280E+00  4
H2O     (adjust)  H  2O  1  0  0  300.00  5000.00  1000.00  1
2.61104720E+00  3.15631300E-03-9.29854380E-07  1.33315380E-10-7.46893510E-15  2
-2.98681670E+04  7.20912680E+00  4.16772340E+00-1.81149700E-03  5.94712880E-06  3
-4.86920210E-09  1.52919910E-12-3.02899690E+04-7.31354740E-01  4
CO      (adjust)  C  1O  1  0  0  300.00  5000.00  1000.00  1
3.02507806E+00  1.44268852E-03-5.63082779E-07  1.01858133E-10-6.91095156E-15  2
-1.42683496E+04  6.10821772E+00  3.26245165E+00  1.51194085E-03-3.88175522E-06  3
5.58194424E-09-2.47495123E-12-1.43105391E+04  4.84889698E+00  4
CO2     (adjust)  C  1O  2  0  0  300.00  5000.00  1000.00  1
4.45362282E+00  3.14016873E-03-1.27841054E-06  2.39399667E-10-1.66903319E-14  2
-4.89669609E+04-9.55395877E-01  2.27572465E+00  9.92207229E-03-1.04091132E-05  3
6.86668678E-09-2.11728009E-12-4.83731406E+04  1.01884880E+01  4
O2      (adjust)  O  2  0  0  0  300.00  5000.00  1000.00  1
3.61221390E+00  7.48531660E-04-1.98206470E-07  3.37490080E-11-2.39073740E-15  2
-1.19781510E+03  3.67033070E+00  3.78371350E+00-3.02336340E-03  9.94927510E-06  3
-9.81891010E-09  3.30318250E-12-1.06381070E+03  3.64163450E+00  4
AR      (adjust)  AR  1  0  0  0  300.00  5000.00  1000.00  1
2.50000000E+00  0.00000000E+00  0.00000000E+00  0.00000000E+00  0.00000000E+00  2

```

Appendix A (continued)

```

-7.45375020E+02 4.36600060E+00 2.50000000E+00 0.00000000E+00 0.00000000E+00 3
0.00000000E+00 0.00000000E+00-7.45374980E+02 4.36600060E+00 4
N2 (adjust) N 2 0 0 0 300.00 5000.00 1000.00 1
2.85328990E+00 1.60221280E-03-6.29368930E-07 1.14410220E-10-7.80574650E-15 2
-8.90080930E+02 6.39648970E+00 3.70441770E+00-1.42187530E-03 2.86703920E-06 3
-1.20288850E-09-1.39546770E-14-1.06407950E+03 2.23362850E+00 4
NI(s) (adjust) NI 1 0 0 0 300.00 3000.00 1000.00 1
0.00000000E+00 0.00000000E+00 0.00000000E+00 0.00000000E+00 0.00000000E+00 2
0.00000000E+00 0.00000000E+00 0.00000000E+00 0.00000000E+00 0.00000000E+00 3
0.00000000E+00 0.00000000E+00 0.00000000E+00 0.00000000E+00 0.00000000E+00 4
H2O(s) (adjust) H 2O 1NI 1 0 500.00 2000.00 2000.00 1
3.50421382E+00 6.68594839E-04 1.76268743E-06-1.17030152E-09 2.26185355E-13 2
-3.79129166E+04-1.05582534E+01 3.50421382E+00 6.68594839E-04 1.76268743E-06 3
-1.17030152E-09 2.26185355E-13-3.79129166E+04-1.05582534E+01 4
H(s) (adjust) H 1NI 1 0 0 500.00 2000.00 2000.00 1
1.38522354E+00-3.60291509E-05 1.01482878E-06-6.39234047E-10 1.26064639E-13 2
-5.45886573E+03-5.04262898E+00 1.38522354E+00-3.60291509E-05 1.01482878E-06 3
-6.39234047E-10 1.26064639E-13-5.45886573E+03-5.04262898E+00 4
OH(s) (adjust) H 1O 1NI 1 0 500.00 2000.00 2000.00 1
2.08905501E+00 1.71443903E-03-4.27838552E-07 9.11211411E-12 1.13760370E-14 2
-2.67334298E+04-3.86138841E+00 2.08905501E+00 1.71443903E-03-4.27838552E-07 3
9.11211411E-12 1.13760370E-14-2.67334298E+04-3.86138841E+00 4
CO(s) (adjust) C 1O 1NI 1 0 500.00 2000.00 2000.00 1
1.04958397E+00 5.37825549E-03-3.51895909E-06 1.06323431E-09-1.12689240E-13 2
-2.73744388E+04 7.60559022E+00 1.04958397E+00 5.37825549E-03-3.51895909E-06 3
1.06323431E-09-1.12689240E-13-2.73744388E+04 7.60559022E+00 4
C(s) (adjust) C 1NI 1 0 0 500.00 2000.00 2000.00 1
-3.49330914E+00 5.23524687E-03-3.03308918E-06 6.55611035E-10-1.40966550E-14 2
-2.23124726E+03 7.68421239E+00-3.49330914E+00 5.23524687E-03-3.03308918E-06 3
6.55611035E-10-1.40966550E-14-2.23124726E+03 7.68421239E+00 4
CH3(s) (adjust) C 1H 3NI 1 0 500.00 2000.00 2000.00 1
-6.10760599E-01 8.61612510E-03-2.17714930E-06-6.63815294E-10 3.13819319E-13 2
-8.89792082E+03-2.00828704E+00-6.10760599E-01 8.61612510E-03-2.17714930E-06 3
-6.63815294E-10 3.13819319E-13-8.89792082E+03-2.00828704E+00 4
CH2(s) (adjust) C 1H 2NI 1 0 500.00 2000.00 2000.00 1
-1.56917589E+00 7.30948876E-03-2.33683999E-06-2.63575385E-10 2.08877321E-13 2
1.94307500E+03 4.44265982E+00-1.56917589E+00 7.30948876E-03-2.33683999E-06 3
-2.63575385E-10 2.08877321E-13 1.94307500E+03 4.44265982E+00 4
CH(s) (adjust) C 1H 1NI 1 0 500.00 2000.00 2000.00 1
-2.52762352E+00 6.00297402E-03-2.49669461E-06 1.36758705E-10 1.03915796E-13 2
9.56681068E+03 7.44010148E+00-2.52762352E+00 6.00297402E-03-2.49669461E-06 3
1.36758705E-10 1.03915796E-13 9.56681068E+03 7.44010148E+00 4
CH4(s) (adjust) C 1H 4NI 1 0 500.00 2000.00 2000.00 1
3.47651462E-01 9.92277358E-03-2.01747493E-06-1.06404583E-09 4.18759375E-13 2
-1.38997273E+04-4.61646253E+00 3.47651462E-01 9.92277358E-03-2.01747493E-06 3
-1.06404583E-09 4.18759375E-13-1.38997273E+04-4.61646253E+00 4
O(s) (adjust) O 1NI 1 0 0 500.00 2000.00 2000.00 1
9.33885773E-01 1.49287485E-03-1.51153811E-06 7.60133452E-10-1.42499395E-13 2
-2.88011883E+04-3.47247502E+00 9.33885773E-01 1.49287485E-03-1.51153811E-06 3
7.60133452E-10-1.42499395E-13-2.88011883E+04-3.47247502E+00 4
CO2(s) (adjust) C 1O 2NI 1 0 500.00 2000.00 2000.00 1
2.15782085E+00 8.85798101E-03-7.33295570E-06 3.01455469E-09-4.83617407E-13 2
-5.17211366E+04-3.96778204E-01 2.15782085E+00 8.85798101E-03-7.33295570E-06 3
3.01455469E-09-4.83617407E-13-5.17211366E+04-3.96778204E-01 4
HCO(s) (adjust) C 1H 1O 1NI 1 500.00 2000.00 2000.00 1
1.42054865E+00 6.41898600E-03-3.25611216E-06 6.60406470E-10-1.25958802E-14 2
-1.72299589E+04-1.34060408E+00 1.42054865E+00 6.41898600E-03-3.25611216E-06 3
6.60406470E-10-1.25958802E-14-1.72299589E+04-1.34060408E+00 4

```

Appendix A (continued)

END							
REACTIONS	KJOULES/MOLE						
H2	+	2NI(s)	=>	2H(s)	1.000E-002	0.00	0.0
		STICK					
2H(s)			=>	H2	+ 2NI(s)	2.545E+019	0.00 81.2
O2	+	2NI(s)	=>	2O(s)	1.000E-002	0.00	0.0
		STICK					
2O(s)			=>	O2	+ 2NI(s)	4.283E+023	0.00 474.9
CH4	+	NI(s)	=>	CH4(s)	8.000E-003	0.00	0.0
		STICK					
CH4(s)			=>	CH4	+ NI(s)	8.705E+015	0.00 37.5
H2O	+	NI(s)	=>	H2O(s)	1.000E-001	0.00	0.0
		STICK					
H2O(s)			=>	H2O	+ NI(s)	3.732E+012	0.00 60.8
CO2	+	NI(s)	=>	CO2(s)	1.000E-005	0.00	0.0
		STICK					
CO2(s)			=>	CO2	+ NI(s)	6.447E+007	0.00 26.0
CO	+	NI(s)	=>	CO(s)	5.000E-001	0.00	0.0
		STICK					
CO(s)			=>	CO	+ NI(s)	3.563E+011	0.00 111.3
	COV	/CO(s)				0.000E+000	0.00 -50.0/
H(s)	+	O(s)	=>	NI(s)	+ OH(s)	5.000E+022	0.00 97.9
NI(s)	+	OH(s)	=>	H(s)	+ O(s)	1.781E+021	0.00 36.1
H(s)	+	OH(s)	=>	NI(s)	+ H2O(s)	3.000E+020	0.00 42.7
NI(s)	+	H2O(s)	=>	H(s)	+ OH(s)	2.271E+021	0.00 91.8
2OH(s)			=>	H2O(s)	+ O(s)	3.000E+021	0.00 100.0
H2O(s)	+	O(s)	=>	2OH(s)	6.373E+023	0.00	210.9
C(s)	+	O(s)	=>	NI(s)	+ CO(s)	5.200E+023	0.00 148.1
NI(s)	+	CO(s)	=>	C(s)	+ O(s)	1.354E+022	-3.00 116.1
	COV	/CO(s)				0.000E+000	0.00 -50.0/
CO(s)	+	O(s)	=>	NI(s)	+ CO2(s)	2.000E+019	0.00 123.6
	COV	/CO(s)				0.000E+000	0.00 -50.0/
NI(s)	+	CO2(s)	=>	CO(s)	+ O(s)	4.653E+023	-1.00 89.3
NI(s)	+	HCO(s)	=>	H(s)	+ CO(s)	3.700E+021	0.00 0.0
	COV	/CO(s)				0.000E+000	0.00 50.0/
H(s)	+	CO(s)	=>	NI(s)	+ HCO(s)	4.019E+020	-1.00 132.2
NI(s)	+	HCO(s)	=>	CH(s)	+ O(s)	3.700E+024	-3.00 95.8
CH(s)	+	O(s)	=>	NI(s)	+ HCO(s)	4.604E+020	0.00 110.0
NI(s)	+	CH4(s)	=>	H(s)	+ CH3(s)	3.700E+021	0.00 57.7
H(s)	+	CH3(s)	=>	NI(s)	+ CH4(s)	6.034E+021	0.00 61.6
NI(s)	+	CH3(s)	=>	H(s)	+ CH2(s)	3.700E+024	0.00 100.0
H(s)	+	CH2(s)	=>	NI(s)	+ CH3(s)	1.293E+023	0.00 55.3
NI(s)	+	CH2(s)	=>	H(s)	+ CH(s)	3.700E+024	0.00 97.1
H(s)	+	CH(s)	=>	NI(s)	+ CH2(s)	4.089E+024	0.00 79.2
NI(s)	+	CH(s)	=>	H(s)	+ C(s)	3.700E+021	0.00 18.8
H(s)	+	C(s)	=>	NI(s)	+ CH(s)	4.562E+022	0.00 161.1
CH4(s)	+	O(s)	=>	OH(s)	+ CH3(s)	1.700E+024	0.00 88.3
OH(s)	+	CH3(s)	=>	CH4(s)	+ O(s)	9.876E+022	0.00 30.4
CH3(s)	+	O(s)	=>	OH(s)	+ CH2(s)	3.700E+024	0.00 130.1
OH(s)	+	CH2(s)	=>	CH3(s)	+ O(s)	4.607E+021	0.00 23.6
CH2(s)	+	O(s)	=>	OH(s)	+ CH(s)	3.700E+024	0.00 126.8
OH(s)	+	CH(s)	=>	CH2(s)	+ O(s)	1.457E+023	0.00 47.1
CH(s)	+	O(s)	=>	OH(s)	+ C(s)	3.700E+021	0.00 48.1
OH(s)	+	C(s)	=>	CH(s)	+ O(s)	1.625E+021	0.00 128.6

END

Appendix A (continued)

Here is reported the translated mechanism file (in *Cantera* format):

```

units(length = "cm", time = "s", quantity = "mol", act_energy = "J/mol")

ideal_gas(name = "gas",
           elements = "O H C N Ar",

species = "" gri30: H2  H  O  O2  OH  H2O  C  CH
                    CH2  CH2(S)  CH3  CH4  CO  CO2
                    HCO  N2  AR  "",

           transport = 'Mix',
           reactions = 'gri30: all',
           options = ['skip_undeclared_elements',
                     'skip_undeclared_species'],
           initial_state = state(temperature = 900.0, pressure = OneAtm)
)

ideal_interface(name = "Ni_surf",
                elements = " Ni H O C ",
                species = "" NI(S)  H(S)  O(S)  OH(S)
                          H2O(S)  C(S)  CH(S)  CH2(S)s
                          CH3(S)  CH4(S)  CO(S)  CO2(S)
                          HCO(S)  "",
                phases = "gas",
                site_density = 25.00E-09,
                reactions = "all",
                initial_state = state(temperature = 1073.0, pressure = OneAtm)
)

# Species data

species(name = "NI(S)",
        atoms = " Ni:1 ",
        thermo = (
            NASA( [ 300.00, 1000.00], [ 0.00000000E+00, 0.00000000E+00,
            0.00000000E+00, 0.00000000E+00, 0.00000000E+00,
            0.00000000E+00, 0.00000000E+00] ),
            NASA( [ 1000.00, 3000.00], [ 0.00000000E+00, 0.00000000E+00,
            0.00000000E+00, 0.00000000E+00, 0.00000000E+00,
            0.00000000E+00, 0.00000000E+00] )
        )
)

species(name = "CH4(S)",
        atoms = " C:1  H:4  Ni:1 ",
        thermo = (
            NASA( [ 500.00, 2000.00], [ 3.47651462E-01, 9.92277358E-03,
            -2.01747493E-06, -1.06404583E-09, 4.18759375E-13,
            -1.38997273E+04, -4.61646253E+00] ),
            NASA( [ 2000.00, 2000.00], [ 3.47651462E-01, 9.92277358E-03,
            -2.01747493E-06, -1.06404583E-09, 4.18759375E-13,
            -1.38997273E+04, -4.61646253E+00] )
        )
)

species(name = "H(S)",

```

Appendix A (continued)

```

atoms = " H:1 Ni:1 ",
thermo = (
  NASA( [ 500.00, 2000.00], [ 1.38522354E+00, -3.60291509E-05,
    1.01482878E-06, -6.39234047E-10, 1.26064639E-13,
    -5.45886573E+03, -5.04262898E+00] ),
  NASA( [ 2000.00, 2000.00], [ 1.38522354E+00, -3.60291509E-05,
    1.01482878E-06, -6.39234047E-10, 1.26064639E-13,
    -5.45886573E+03, -5.04262898E+00] )
)

species(name = "H2O(S)",
atoms = " O:1 H:2 Ni:1 ",
thermo = (
  NASA( [ 500.00, 2000.00], [ 3.50421382E+00, 6.68594839E-04,
    1.76268743E-06, -1.17030152E-09, 2.26185355E-13,
    -3.79129166E+04, -1.05582534E+01] ),
  NASA( [ 2000.00, 2000.00], [ 3.50421382E+00, 6.68594839E-04,
    1.76268743E-06, -1.17030152E-09, 2.26185355E-13,
    -3.79129166E+04, -1.05582534E+01] )
)

species(name = "CO(S)",
atoms = " C:1 O:1 Ni:1 ",
thermo = (
  NASA( [ 500.00, 2000.00], [ 1.04958397E+00, 5.37825549E-03,
    -3.51895909E-06, 1.06323431E-09, -1.12689240E-13,
    -2.73744388E+04, 7.60559022E+00] ),
  NASA( [ 2000.00, 2000.00], [ 1.04958397E+00, 5.37825549E-03,
    -3.51895909E-06, 1.06323431E-09, -1.12689240E-13,
    -2.73744388E+04, 7.60559022E+00] )
)

species(name = "CO2(S)",
atoms = " C:1 O:2 Ni:1 ",
thermo = (
  NASA( [ 500.00, 2000.00], [ 2.15782085E+00, 8.85798101E-03,
    -7.33295570E-06, 3.01455469E-09, -4.83617407E-13,
    -5.17211366E+04, -3.96778204E-01] ),
  NASA( [ 2000.00, 2000.00], [ 2.15782085E+00, 8.85798101E-03,
    -7.33295570E-06, 3.01455469E-09, -4.83617407E-13,
    -5.17211366E+04, -3.96778204E-01] )
)

species(name = "O(S)",
atoms = " O:1 Ni:1 ",
thermo = (
  NASA( [ 500.00, 2000.00], [ 9.33885773E-01, 1.49287485E-03,
    -1.51153811E-06, 7.60133452E-10, -1.42499395E-13,
    -2.88011883E+04, -3.47247502E+00] ),
  NASA( [ 2000.00, 2000.00], [ 9.33885773E-01, 1.49287485E-03,
    -1.51153811E-06, 7.60133452E-10, -1.42499395E-13,
    -2.88011883E+04, -3.47247502E+00] )
)

```

Appendix A (continued)

```

species(name = "OH(S)",
  atoms = " O:1 H:1 Ni:1 ",
  thermo = (
    NASA( [ 500.00, 2000.00], [ 2.08905501E+00, 1.71443903E-03,
      -4.27838552E-07, 9.11211411E-12, 1.13760370E-14,
      -2.67334298E+04, -3.86138841E+00] ),
    NASA( [ 2000.00, 2000.00], [ 2.08905501E+00, 1.71443903E-03,
      -4.27838552E-07, 9.11211411E-12, 1.13760370E-14,
      -2.67334298E+04, -3.86138841E+00] )
  )
)

species(name = "C(S)",
  atoms = " C:1 Ni:1 ",
  thermo = (
    NASA( [ 500.00, 2000.00], [ -3.49330914E+00, 5.23524687E-03,
      -3.03308918E-06, 6.55611035E-10, -1.40966550E-14,
      -2.23124726E+03, 7.68421239E+00] ),
    NASA( [ 2000.00, 2000.00], [ -3.49330914E+00, 5.23524687E-03,
      -3.03308918E-06, 6.55611035E-10, -1.40966550E-14,
      -2.23124726E+03, 7.68421239E+00] )
  )
)

species(name = "CH3(S)",
  atoms = " C:1 H:3 Ni:1 ",
  thermo = (
    NASA( [ 500.00, 2000.00], [ -6.10760599E-01, 8.61612510E-03,
      -2.17714930E-06, -6.63815294E-10, 3.13819319E-13,
      -8.89792082E+03, -2.00828704E+00] ),
    NASA( [ 2000.00, 2000.00], [ -6.10760599E-01, 8.61612510E-03,
      -2.17714930E-06, -6.63815294E-10, 3.13819319E-13,
      -8.89792082E+03, -2.00828704E+00] )
  )
)

species(name = "CH2(S)s",
  atoms = " C:1 H:2 Ni:1 ",
  thermo = (
    NASA( [ 500.00, 2000.00], [ -1.56917589E+00, 7.30948876E-03,
      -2.33683999E-06, -2.63575385E-10, 2.08877321E-13,
      1.94307500E+03, 4.44265982E+00] ),
    NASA( [ 2000.00, 2000.00], [ -1.56917589E+00, 7.30948876E-03,
      -2.33683999E-06, -2.63575385E-10, 2.08877321E-13,
      1.94307500E+03, 4.44265982E+00] )
  )
)

species(name = "CH(S)",
  atoms = " C:1 H:1 Ni:1 ",
  thermo = (
    NASA( [ 500.00, 2000.00], [ -2.52762352E+00, 6.00297402E-03,
      -2.49669461E-06, 1.36758705E-10, 1.03915796E-13,
      9.56681068E+03, 7.44010148E+00] ),
    NASA( [ 2000.00, 2000.00], [ -2.52762352E+00, 6.00297402E-03,
      -2.49669461E-06, 1.36758705E-10, 1.03915796E-13,
      9.56681068E+03, 7.44010148E+00] )
  )
)

```

Appendix A (continued)

```

species(name = "HCO(S)",
  atoms = " C:1 O:1 H:1 Ni:1 ",
  thermo = (
    NASA( [ 500.00, 2000.00], [ 1.42054865E+00, 6.41898600E-03,
      -3.25611216E-06, 6.60406470E-10, -1.25958802E-14,
      -1.72299589E+04, -1.34060408E+00] ),
    NASA( [ 2000.00, 2000.00], [ 1.42054865E+00, 6.41898600E-03,
      -3.25611216E-06, 6.60406470E-10, -1.25958802E-14,
      -1.72299589E+04, -1.34060408E+00] )
  )
)

# Reaction data

# Reaction 1
surface_reaction("H2 + 2 NI(S) => 2 H(S)", stick(1.000E-002, 0.00, 0.0))

# Reaction 2
surface_reaction("2 H(S) => H2 + 2 NI(S)", Arrhenius(2.545E+019, 0.00, 81200))

# Reaction 3
surface_reaction("O2 + 2 NI(S) => 2 O(S)", stick(1.000E-002, 0.00, 0.0))

# Reaction 4
surface_reaction("2 O(S) => O2 + 2 NI(S)" Arrhenius(4.283E+023, 0.00, 474900))

# Reaction 5
surface_reaction("CH4 + NI(S) => CH4(S)", stick(8.000E-003, 0.00, 0.0))

# Reaction 6
surface_reaction("CH4(S) => CH4 + NI(S)", Arrhenius(8.705E+015, 0.00, 37500))

# Reaction 7
surface_reaction("H2O + NI(S) => H2O(S)", stick(1.000E-001, 0.00, 0.0))

# Reaction 8
surface_reaction("H2O(S) => H2O + NI(S)", Arrhenius(3.732E+012, 0.00, 60800))

# Reaction 9
surface_reaction("CO2 + NI(S) => CO2(S)", stick(1.000E-005, 0.00, 0.0))

# Reaction 10
surface_reaction("CO2(S) => CO2 + NI(S)", Arrhenius(6.447E+07, 0.00, 26000))

# Reaction 11
surface_reaction("CO + NI(S) => CO(S)", stick(5.000E-001, 0.00, 0.0))

# Reaction 12
surface_reaction("CO(S) => CO + NI(S)", Arrhenius(3.563E+011, 0.00, 111300,
  coverage = ['CO(S)', 0.0, 0.0, -50000]))

# Reaction 13
surface_reaction("H(S) + O(S) => NI(S) + OH(S)", Arrhenius(5.000E+022, 0.00,
  97900))

# Reaction 14
surface_reaction("NI(S) + OH(S) => H(S) + O(S)", Arrhenius(1.781E+021, 0.00,
  36100))

```

Appendix A (continued)

```
# Reaction 15
surface_reaction("H(S) + OH(S) => NI(S) + H2O(S)", Arrhenius(3.000E+020, 0.00,
42700))

# Reaction 16
surface_reaction("NI(S) + H2O(S) => H(S) + OH(S)", Arrhenius(2.271E+021, 0.00,
91800))

# Reaction 17
surface_reaction("2 OH(S) => H2O(S) + O(S)", Arrhenius(3.000E+021, 0.00,
100000))

# Reaction 18
surface_reaction("H2O(S) + O(S) => 2 OH(S)", Arrhenius(6.373E+023, 0.00,
210900))

# Reaction 19
surface_reaction("C(S) + O(S) => NI(S) + CO(S)", Arrhenius(5.200E+023, 0.00,
148100))

# Reaction 20
surface_reaction("NI(S) + CO(S) => C(S) + O(S)", Arrhenius(1.354E+022, -3.00,
116100,
                    coverage = ['CO(S)', 0.0, 0.0, -50000]))

# Reaction 21
surface_reaction("CO(S) + O(S) => NI(S) + CO2(S)", Arrhenius(2.000E+019, 0.00,
123600,
                    coverage = ['CO(S)', 0.0, 0.0, -50000]))

# Reaction 22
surface_reaction("NI(S) + CO2(S) => CO(S) + O(S)", Arrhenius(4.653E+023, -1.00,
89300))

# Reaction 23
surface_reaction("NI(S) + HCO(S) => H(S) + CO(S)", Arrhenius(3.700E+021, 0.00,
0.0,
                    coverage = ['CO(S)', 0.0, 0.0, 50000]))

# Reaction 24
surface_reaction("H(S) + CO(S) => NI(S) + HCO(S)", Arrhenius(4.019E+020, -1.00,
132200))

# Reaction 25
surface_reaction("NI(S) + HCO(S) => CH(S) + O(S)", Arrhenius(3.700E+024, -3.00,
95800))

# Reaction 26
surface_reaction("CH(S) + O(S) => NI(S) + HCO(S)", Arrhenius(4.604E+020, 0.00,
110000))

# Reaction 27
surface_reaction("NI(S) + CH4(S) => H(S) + CH3(S)", Arrhenius(3.700E+021, 0.00,
57700))

# Reaction 28
surface_reaction("H(S) + CH3(S) => NI(S) + CH4(S)", Arrhenius(6.034E+021, 0.00,
61600))
```

Appendix A (continued)

```
# Reaction 29
surface_reaction("NI(S) + CH3(S) => H(S) + CH2(S)s", Arrhenius(3.700E+024, 0.00,
100000))

# Reaction 30
surface_reaction("H(S) + CH2(S)s => NI(S) + CH3(S)", Arrhenius(1.293E+023, 0.00,
55300))

# Reaction 31
surface_reaction("NI(S) + CH2(S)s => H(S) + CH(S)", Arrhenius(3.700E+024, 0.00,
97100))

# Reaction 32
surface_reaction("H(S) + CH(S) => NI(S) + CH2(S)s", Arrhenius(4.089E+024, 0.00,
79200))

# Reaction 33
surface_reaction("NI(S) + CH(S) => H(S) + C(S)", Arrhenius(3.700E+021, 0.00,
18800))

# Reaction 34
surface_reaction("H(S) + C(S) => NI(S) + CH(S)", Arrhenius(4.562E+022, 0.00,
161100))

# Reaction 35
surface_reaction("CH4(S) + O(S) => OH(S) + CH3(S)", Arrhenius(1.700E+024, 0.00,
88300))

# Reaction 36
surface_reaction("OH(S) + CH3(S) => CH4(S) + O(S)", Arrhenius(9.876E+022, 0.00,
30400))

# Reaction 37
surface_reaction("CH3(S) + O(S) => OH(S) + CH2(S)s", Arrhenius(3.700E+024, 0.00,
130100))

# Reaction 38
surface_reaction("OH(S) + CH2(S)s => CH3(S) + O(S)", Arrhenius(4.607E+021, 0.00,
23600))

# Reaction 39
surface_reaction("CH2(S)s + O(S) => OH(S) + CH(S)", Arrhenius(3.700E+024, 0.00,
126800))

# Reaction 40
surface_reaction("OH(S) + CH(S) => CH2(S)s + O(S)", Arrhenius(1.457E+023, 0.00,
47100))

# Reaction 41
surface_reaction("CH(S) + O(S) => OH(S) + C(S)", Arrhenius(3.700E+021, 0.00,
48100))

# Reaction 42
surface_reaction("OH(S) + C(S) => CH(S) + O(S)", Arrhenius(1.625E+021, 0.00,
128600))
```

Appendix A (continued)

This appendix also presents some general rules to follow when translating a mechanism file from *CHEMKIN* to *Cantera* format. More specific information can be found in reference [54].

As we can easily see in paragraph 8.2, the only preliminary information needed by the file in *CHEMKIN* format is represented by the definition of the surface site density and the declaration of the surface species involved in the process, as follows:

```
SITE    /NI_surface/    SDEN /2.66E-09/
        NI(s)           /1/
        H2O(s)          /1/
        H(s)            /1/
        OH(s)           /1/
        CO(s)           /1/
        C(s)            /1/
        CH3(s)          /1/
        CH2(s)          /1/
        CH(s)           /1/
        CH4(s)          /1/
        O(s)            /1/

        CO2(s)          /1/
        HCO(s)          /1/
END
```

When translating to *Cantera* format, more information must be given, including:

- definition of all units:

```
units(length = "cm", time = "s", quantity = "mol", act_energy = "J/mol")
```

- definition of an ideal gas object, including elements, species, transport properties, reactions, and other options (initial state is required just to provide an initial guess when starting an iterative computation) taken from the *GRI 3.0* mechanism, in order to guarantee the occurrence of traditional homogeneous reactions and the correct use of the thermodynamic data:

```
ideal_gas(name = "gas",
           elements = "O H C N Ar",
           species = "" gri30: H2  H  O  O2  OH  H2O  C  CH
                        CH2  CH2(S)  CH3  CH4  CO  CO2
                        HCO  N2  AR  """,
           transport = 'Mix',
           reactions = 'gri30: all',
           options = ['skip_undeclared_elements',
                     'skip_undeclared_species'],
```

Appendix A (continued)

```
initial_state = state(temperature = 900.0, pressure = OneAtm)
)
```

- definition of an ideal interface, including elements, surface species, phases, reactions, surface site density, and other options (this is the information actually taken from the lines in *CHEMKIN* format reported above):

```
ideal_interface(name = "Ni_surf",
  elements = " Ni H O C ",
  species = "" NI(S)  H(S)  O(S)  OH(S)
            H2O(S) C(S)  CH(S) CH2(S)s
            CH3(S) CH4(S) CO(S) CO2(S)
            HCO(S) """,
  phases = "gas",
  site_density = 25.00E-09,
  reactions = "all",
  initial_state = state(temperature = 1073.0, pressure = OneAtm)
)
```

Thermodynamic data must be provided for every chemical species. When translating to *Cantera* format, only the data of the surface species must be specified, since those of traditional species for homogeneous chemistry are indirectly provided by calling the *GRI 3.0* mechanism. Here is a surface-species declaration in *CHEMKIN* format:

```
CO2(s)      (adjust) C  10  2NI  1  0  500.00  2000.00  2000.00  1
 2.15782085E+00 8.85798101E-03-7.33295570E-06 3.01455469E-09-4.83617407E-13 2
-5.17211366E+04-3.96778204E-01 2.15782085E+00 8.85798101E-03-7.33295570E-06 3
 3.01455469E-09-4.83617407E-13-5.17211366E+04-3.96778204E-01 4
```

Its translated version becomes:

```
species(name = "CO2(S)",
  atoms = " C:1 O:2 Ni:1 ",
  thermo = (
    NASA( [ 500.00, 2000.00], [ 2.15782085E+00, 8.85798101E-03,
      -7.33295570E-06, 3.01455469E-09, -4.83617407E-13,
      -5.17211366E+04, -3.96778204E-01] ),
    NASA( [ 2000.00, 2000.00], [ 2.15782085E+00, 8.85798101E-03,
      -7.33295570E-06, 3.01455469E-09, -4.83617407E-13,
      -5.17211366E+04, -3.96778204E-01] )
  )
)
```

Appendix A (continued)

As we can easily see, syntax is quite easy to understand as it always follows the same scheme. It is important to note how the atoms are declared every time and how capital letters are always needed in the name line only (for instance, nickel will be NI(S) in the name line and Ni:1 in the atoms line). If we number all thermo data in *Cantera* format from 1 to 18, they will appear in *CHEMKIN* format by following the order 1, 11, 2/10, 12, 13, 14, 15, 16, 17, 18, 3, 4, 5, 6, 7, 8, 9. This is the reason why the sorting must be done carefully.

When translating chemical reactions, the user can face three different types of reactions.

For general reactions like:

```
NI(s) + OH(s) => H(s) + O(s) 1.781E+021 0.00 36.1
```

the translated reaction can be both:

```
surface_reaction("NI(S) + OH(S) => H(S) + O(S)", Arrhenius(1.781E+021, 0.00, 36100))
```

and:

```
surface_reaction("NI(S) + OH(S) => H(S) + O(S)", [1.781E+021, 0.00, 36100])
```

The Arrhenius formulation will be respected in both cases. Note how the unit for the activation energy is different (the file in *CHEMKIN* format needs it to be declared at the beginning of the reaction data after the word "REACTIONS"). The second type of reactions is represented by a reaction where sticking coefficients are provided:

```
H2 + 2NI(s) => 2H(s) 1.000E-002 0.00 0.0
STICK
```

In this case, translation is quite easy again and comes out to be:

```
surface_reaction("H2 + 2 NI(S) => 2 H(S)", stick(1.000E-002, 0.00, 0.0))
```

Eventually, when coverage data are provided as follows:

```
CO(s) => CO + NI(s) 3.563E+011 0.00 111.3
COV /CO(s) 0.000E+000 0.00 -50.0/
```

the translation will be:

Appendix A (continued)

```
surface_reaction("CO(S) => CO + NI(S)", Arrhenius(3.563E+011, 0.00, 111300,  
coverage = ['CO(S)', 0.0, 0.0, -50000]))
```

Unlike general reactions, in this case the word “Arrhenius” is always necessary.

Appendix B

This appendix contains a list of tables which describe the tests performed to acquire all data used to develop the second part of this study (concerning tubular SOFCs).

The details about dry-reforming tests are shown below:

TABLE XIV. DRY-REFORMING TESTS: GENERAL INFORMATION.

T _{cell} : 800°C				
Fuel Molar Composition	CH ₄	0.6		
	CO ₂	0.4		
Addition	CO ₂	1	1.5	2

gas analysis required

TABLE XV. TEST 1, 2, 3. MATRIX DESIGN VARIABLE: METHANE FLOW RATE (Nml/min).

Current (A)	Fuel Utilization													
	25%	30%	35%	40%	45%	50%	55%	60%	65%	70%	75%	80%	85%	90%
OCV	-	-	-	-	-	-	-	-	-	-	-	-	-	-
2.5	-	-	-	-	-	-	-	-	-	-	-	-	-	-
5	-	-	-	-	-	-	-	-	-	-	-	-	-	-
7.5	53	44	-	-	-	-	-	-	-	-	-	-	-	-
10	71	59	50	44	-	-	-	-	-	-	-	-	-	-
12.5	88	74	63	55	49	44	-	-	-	-	-	-	-	-
15	106	88	76	66	59	53	48	44	-	-	-	-	-	-
17.5	124	103	88	77	69	62	56	51	48	44	-	-	-	-
20	141	118	101	88	78	71	64	59	54	50	47	44	-	-
22.5	159	132	113	99	88	79	72	66	61	57	53	50	47	44
25	177	147	126	110	98	88	80	74	68	63	59	55	52	49

Appendix B (continued)

TABLE XVI. TEST 4, 5, 6. MATRIX DESIGN VARIABLE: FUEL UTILIZATION FACTOR.

Current (A)	Methane Flow (Nml/min)											
	50	60	70	80	90	100	110	120	130	140	150	160
OCV	0.0%	0.0%	0.0%	0.0%	0.0%	0.0%	0.0%	0.0%	0.0%	0.0%	0.0%	0.0%
2.5	17%	17%	16%	15%	15%	14%	13%	13%	12%	12%	12%	11%
5	26%	25%	24%	23%	22%	21%	20%	19%	19%	18%	17%	17%
7.5	35%	33%	32%	30%	29%	28%	27%	26%	25%	24%	23%	22%
10	44%	42%	40%	38%	36%	35%	34%	32%	31%	30%	29%	28%
12.5	52%	50%	48%	45%	44%	42%	40%	39%	37%	36%	35%	34%
15	61%	58%	55%	53%	51%	49%	47%	45%	44%	42%	41%	39%
17.5	70%	66%	63%	61%	58%	56%	54%	52%	50%	48%	46%	45%
20	78%	75%	71%	68%	65%	63%	60%	58%	56%	54%	52%	51%
22.5	87%	83%	79%	76%	73%	70%	67%	65%	62%	60%	58%	56%
25	96%	91%	87%	83%	80%	77%	74%	71%	69%	66%	64%	62%
27.5	105%	100%	95%	91%	87%	84%	80%	77%	75%	72%	70%	67%
30	-	-	-	99%	94%	91%	87%	84%	81%	78%	76%	73%
32.5	-	-	-	-	-	98%	94%	90%	87%	84%	81%	79%
35	-	-	-	-	-	-	-	97%	93%	90%	87%	84%
37.5	-	-	-	-	-	-	-	-	100%	96%	93%	90%
40	-	-	-	-	-	-	-	-	-	-	99%	96%
42.5	-	-	-	-	-	-	-	-	-	-	-	-

The following tables contain the details about the steam-reforming tests:

TABLE XVII. STEAM-REFORMING TESTS: GENERAL INFORMATION.

T _{oven} : 800°C		
Fuel Molar Composition	CH ₄	0.6
	CO ₂	0.4
Addition	H ₂ O	0.3 (T _{bubbler} = 72°C)

gas analysis required

Appendix B (continued)

TABLE XVIII. TEST 1. MATRIX DESIGN VARIABLE: METHANE FLOW RATE (Nml/min).

Current (A)	Fuel Utilization								
	20%	25%	30%	35%	40%	45%	50%	55%	60%
OCV	-	-	-	-	-	-	-	-	-
2.5	-	-	-	-	-	-	-	-	-
5	-	-	-	-	-	-	-	-	-
7.5	-	-	-	-	-	-	-	-	-
10	87.1	-	-	-	-	-	-	-	-
12.5	108.9	87.1	-	-	-	-	-	-	-
15	130.7	104.5	87.1	-	-	-	-	-	-
17.5	152.5	122.0	101.6	87.1	-	-	-	-	-
20	174.2	139.4	116.2	99.6	87.1	-	-	-	-
22.5	196.0	156.8	130.7	112.0	98.0	87.1	-	-	-
25	217.8	174.2	145.2	124.4	108.9	96.8	87.1	-	-
27.5	239.6	191.7	159.7	136.9	119.8	106.5	95.8	87.1	-
30	261.3	209.1	174.2	149.3	130.7	116.2	104.5	95.0	87.1

TABLE XIX. TEST 2. MATRIX DESIGN VARIABLE: FUEL UTILIZATION FACTOR

Current (A)	Methane Flow (Nml/min)								
	100	150	200	250	300	350	400	450	500
OCV	0.0%	0.0%	0.0%	0.0%	0.0%	0.0%	0.0%	0.0%	0.0%
2.5	4.4%	2.9%	2.2%	1.7%	1.5%	1.2%	1.1%	1.0%	0.9%
5	8.7%	5.8%	4.4%	3.5%	2.9%	2.5%	2.2%	1.9%	1.7%
7.5	13.1%	8.7%	6.5%	5.2%	4.4%	3.7%	3.3%	2.9%	2.6%
10	17.4%	11.6%	8.7%	7.0%	5.8%	5.0%	4.4%	3.9%	3.5%
12.5	21.8%	14.5%	10.9%	8.7%	7.3%	6.2%	5.4%	4.8%	4.4%
15	26.1%	17.4%	13.1%	10.5%	8.7%	7.5%	6.5%	5.8%	5.2%
17.5	30.5%	20.3%	15.2%	12.2%	10.2%	8.7%	7.6%	6.8%	6.1%
20	34.8%	23.2%	17.4%	13.9%	11.6%	10.0%	8.7%	7.7%	7.0%
22.5	39.2%	26.1%	19.6%	15.7%	13.1%	11.2%	9.8%	8.7%	7.8%
25	43.6%	29.0%	21.8%	17.4%	14.5%	12.4%	10.9%	9.7%	8.7%
27.5	47.9%	31.9%	24.0%	19.2%	16.0%	13.7%	12.0%	10.6%	9.6%
30	52.3%	34.8%	26.1%	20.9%	17.4%	14.9%	13.1%	11.6%	10.5%

Appendix B (continued)

TABLE XX. TEST 3, 4, 5. MATRIX DESIGN VARIABLES: STEAM-TO-BIOGAS RATIO AND CELL TEMPERATURE ($T_{cell} = 800, 750, 700^{\circ}\text{C}$).

	Methane Flow: 100 Nml/min				Steam Addition (mol-H ₂ O / mol-biogas)
	0,3 (ref.)	0.40	0.50	0.60	
Current (A)	72.0	76.0	79.0	81.5	T_{bubbler} (°C)
OCV	0.0%	0.0%	0.0%	0.0%	
2.5	4.4%	4.4%	4.4%	4.4%	
5	8.7%	8.7%	8.7%	8.7%	
7.5	13.1%	13.1%	13.1%	13.1%	
10	17.4%	17.4%	17.4%	17.4%	
12.5	21.8%	21.8%	21.8%	21.8%	
15	26.1%	26.1%	26.1%	26.1%	
17.5	30.5%	30.5%	30.5%	30.5%	
20	34.8%	34.8%	34.8%	34.8%	
22.5	39.2%	39.2%	39.2%	39.2%	
25	43.6%	43.6%	43.6%	43.6%	
27.5	47.9%	47.9%	47.9%	47.9%	
30	52.3%	52.3%	52.3%	52.3%	

CITED LITERATURE

- [1] <<http://en.wikipedia.org/wiki/Biogas>>.
- [2] Cuellar, A.D. and Webber, M.E.: *Cow power: the energy and emissions benefits of converting manure to biogas*, Environ. Res. Lett., 3: 034002, 2008.
- [3] Bilcan, A., Le Corre, O., and Delebarre, A.: *Thermal Efficiency and Environmental Performances of a Biogas-Diesel Stationary Engine*, Environmental Technology, 24:9, 1165-1173 (2003).
- [4] Yoon, S.H. and Lee, C.S.: *Experimental Investigation on the Combustion and Exhaust Emission Characteristics of Biogas–Biodiesel Dual-Fuel Combustion in a CI Engine*, Fuel Processing Technology, Vol. 92, Issue 5, 992-1000 (2011).
- [5] Henham, A. and Makkar, M.K.: *Combustion of Simulated Biogas in a Dual-Fuel Diesel Engine*, Energy Conversion and Management, Vol. 39, Issues 16-18, 2001-2009 (1998).
- [6] Bedoya, I.D., Saxena, S., Cadavid, F.J., Dibble, R.W., and Wissink, M.: *Experimental Study of Biogas Combustion in an HCCI Engine for Power Generation with High Indicated Efficiency and Ultra-Low NO_x Emissions*, Energy Conversion and Management, Vol. 53, Issue 1, 154-162 (2011).
- [7] Vogler, M., Bieberle-Hutter, A., Gauckler, L., Warnatz, J., and Bessler, W.G.: *Modeling Study of Surface Reactions, Diffusion, and Spillover at a Ni/YSZ Patterned Anode*, Journal of the Electrochemical Society, 156 (5), B663-B672 (2009).
- [8] Hao, Y. and Goodwin, D.G.: *Numerical Study of Heterogeneous Reactions in an SOFC Anode with Oxygen Addition*, Journal of the Electrochemical Society, 155 (7), B666-B674 (2008).
- [9] Goodwin, D.G., Zhu, H., Colclasure, A.M., and Kee, R.J.: *Modeling Electrochemical Oxidation of Hydrogen on Ni-YSZ Pattern Anode*, Journal of the Electrochemical Society, 156 (9), B1004-B1021 (2009).

CITED LITERATURE (continued)

- [10] Zhu, H., Kee, R.J., Janardhanan, V.M., Deutschmann, O., and Goodwin, D.G.: *Modeling Elementary Heterogeneous Chemistry and Electrochemistry in Solid-Oxide Fuel Cells*, Journal of the Electrochemical Society, 152 (12) A2427-A2440 (2005).
- [11] Hecht, E.S., Gupta, G.K., Zhu, H., Dean, A.M., Kee, R.J., Maier, L. and Deutschmann, O.: *Methane Reforming Kinetics within a Ni-YSZ SOFC Anode Support*, Applied Catalysis A: General 295, 40-51 (2005).
- [12] Hao, Y. and Goodwin, D.G.: *Numerical Modeling of Single-Chamber SOFCs with Hydrocarbon Fuels*, Journal of the Electrochemical Society, 154 (2), B207-B217 (2007).
- [13] <<http://www.sandia.gov/chemkin>>.
- [14] Smith, G.P., Golden, D.M., Frencklack, M., Moriarty, N.W., Eiteneer, B., Goldenberg, M., Bowman, C.T., Hanson, R.K., Song, S., Gardiner, W.C., Jr., Lissianski, V.V., and Qin, Z.: <http://www.me.berkeley.edu/gri_mech>.
- [15] <http://www.biogas-renewable-energy.info/biogas_composition.html>.
- [16] Turns, S.R.: *An Introduction to Combustion: Concepts and Applications*, McGraw-Hill International Editions, 2006.
- [17] Chemkin Theory Manual.
- [18] Reynolds, W.C.: *The Element Potential Method for Chemical Equilibrium Analysis: Implementation in the Interactive Program STANJAN*, Department of Mechanical Engineering, Stanford University, 1986.
- [19] Fristrom, R.M.: *Flame Structure and Processes*, Oxford University Press, New York, 1995.
- [20] Hirschfelder, J.O., Curtiss, C.F., and Bird, R.B.: *Molecular Theory of Gases and Liquids*, John Wiley and Sons, New York, 1954.
- [21] Chapman, S., and Cowling, T.G.: *The Mathematical Theory of Non-Uniform Gases*, Cambridge University Press, Cambridge, 1970.

CITED LITERATURE (continued)

- [22] Coffee, T.P., and Heimerl, J.M.: *Combustion and Flame*, 43: 273, 1981.
- [23] Yamaoka, I., and Tsuji, H.: *Determination of burning velocity using counterflow flames*, Symposium (International) on Combustion, Volume 20, Issue 1, Pages 1883-1892, 1985.
- [24] Günther, R., and Janisch, G.: *Measurements of burning velocity in a flat flame front*, *Combustion and Flame*, Volume 19, Issue 1, Pages 49-53, 1972.
- [25] Hassan, M.I., Aung, K.T., and Faeth, G.M.: *Measured and Predicted Properties of Laminar Premixed Methane-Air Flames at Various Pressures*, *Combust. Flame*, 115, 539–550, 1998.
- [26] Egolfopoulos, F.N. and Law, C.K.: *Chain Mechanisms in the Overall Reaction Orders in Laminar Flame Propagation*, *Combust. Flame*, 80, 7–16, 1990.
- [27] Gu, X.U., Haq, M.Z., Lawes, M., and Woolley, R.: *Laminar Burning Velocity and Markstein Length of Methane-Air Mixtures*, *Combust. Flame*, 121, 41–58, 2000.
- [28] Andrews, G.E. and Bradley, D.: *The burning velocity of methane-air mixtures*, *Combustion and Flame*, Volume 19, Issue 2, Pages 275-288, 1972.
- [29] Garforth, A.M. and Rallis, C.J.: *Laminar burning velocity of stoichiometric methane-air: pressure and temperature dependence*, *Combustion and Flame*, Volume 31, Pages 53-68, 1978.
- [30] Babkin, V.S., Korzhavin, A.A., Bunev, V.A.: *Propagation of premixed gaseous explosion flames in porous media*, *Combustion and Flame*, Volume 87, Issue 2, Pages 182-190, 1991.
- [31] Rozenchan, G., Zhu, D.L., Law, C.K., and Tse, S.D.: *Outward Propagating, Burning Velocities and Chemical Effects of Methane Flames up to 60 atm*, *Proc. Combust. Instit.*, 29, 1461–1469, 2002.

CITED LITERATURE (continued)

- [32] Som, S., and Aggarwal, S.K.: *A Numerical Investigation of Methane Air Partially Premixed Flames at Elevated Pressures*, Combustion Science and Technology, 179:6, 1085-1112, 2007.
- [33] Tsuji, H. and Yamaoka, I.: *The Counterflow Diffusion Flame in the Forward Stagnation Region of a Porous Cylinder*, Eleventh Symposium (International) on Combustion, The Combustion Institute, Pittsburgh, PA, p. 979, 1967.
- [34] Hahn, W.A. and Wendt, J.O.L.: *The Flat Laminar Opposed Jet Diffusion Flame: A Novel Tool for Kinetics Studies of Trace Species Formation*, Chemical Engineering Communications, 9: 121-136, 1981.
- [35] Tsuji, H.: *Counterflow Diffusion Flames*, Progress in Energy and Combustion Science, 8: 93-119, 1982.
- [36] Dixon-Lewis, G., et al.: *Calculation of the Structure and Extinction Limit of a Methane-Air Counterflow Diffusion Flame in the Forward Stagnation Region of a Porous Cylinder*, Twentieth Symposium (International) on Combustion, The Combustion Institute, Pittsburgh, PA, p. 1893, 1984
- [37] Flynn, F.F., Durrett, R.P., Hunter, G.L., Loye, A.O.Z., Akinyemi, O.C., Dec, J.E., and Westbrook, C.K.: *An Integrated View Combining Laser Diagnostics, Chemical Kinetics, and Empirical Validation*, Diesel Combustion: Paper 99-01-0509, SAE, 1999.
- [38] Lee, B.J. and Chung, S.H.: *Stabilization of Lifted Tribrachial Flames in a Laminar Non-Premixed Jet*, Combust. Flame, 109, 163–172, 1997.
- [39] Kee, R.J., Miller, J.A., and Evans, G.H.: *Proceedings of the Twenty-Second Symposium (International) on Combustion*, The Combustion Institute, Pittsburgh, PA, p. 1479, 1988.
- [40] Karman, T.V. and Angew A.: *Math. Mech*, 1:233, 1921.
- [41] Schlichting, H.: *Boundary Layer Theory*, McGraw-Hill, New York, 1979.

CITED LITERATURE (continued)

- [42] Evans, G.H. and Grief, R.: *Numerical Heat Transfer*, 14:373, 1988.
- [43] Vagelopoulos, C.M., Egolfopoulos, F.N., and Law, C.K.: *Further Considerations on the Determination of Laminar Flame Speeds with the Counterflow Twin-Flame Technique*, Proc. Combust. Instit., 25, 1341–1347, 1994.
- [44] Eguchi, K., Singhal, S.C., Yokokawa, H., and Mizusaki, J.: *Solid Oxide Fuel Cells 10 (SOFC-X)*, Electrochemical Society Transactions, Vol. 7, No. 1, ECS, Pennington, NJ, 2007.
- [45] Atkinson, A., Barnett, S., Gorte, R.J., Irvine, J.T.S., McEvoy, A.J., Mogensen, M., Singhal, S.C., and Vohs, J.: *Advanced Anodes for High-Temperature Fuel Cells*, Nature Materials, Vol. 3, No. 1, 17-27, 2004.
- [46] Williams, M.C., Strakey, J.P., and Singhal, S.C.: *U.S. Distributed Generation Fuel Cell Program*, Journal of Power Sources, Vol. 131, 79-85, 2004.
- [47] Singhal, S.C. and Kendall, K.: *High Temperature Solid Oxide Fuel Cells: Fundamentals, Design and Applications*, Elsevier, Oxford, 2003.
- [48] Singhal, S.C.: *Solid Oxide Fuel Cells for Stationary, Mobile, and Military Applications*, Solid State Ionics, Vol. 152-153, 405-410, 2002.
- [49] Singhal, S.C.: *Science and Technology of Solid Oxide Fuel Cells*, Materials Research Bulletin, Vol. 25, 16-21, 2000.
- [50] Singhal, S.C.: *Advances in Solid Oxide Fuel Cell Technology*, Solid State Ionics, Vol. 135, 305-313, 2000.
- [51] <<http://www.cantera.org>>.
- [52] <<http://www.detchem.com>>.
- [53] Al-Sarraf, N., Stuckless, J.T., Wartnaby, C.E., and King, D.A.: *Surface Science*, 283, 427 (1993).

CITED LITERATURE (continued)

- [54] Dalle Nogare, D.: *Modeling Catalytic Methane Partial Oxidation with Detailed Chemistry*, PhD Thesis, Dipartimento dei Principi e Impianti dell'Ingegneria Chimica "I. Sorgato", Università degli Studi di Padova, 2008.

VITA

NAME: Francesco Quesito

EDUCATION: Laurea di I Livello in Mechanical Engineering, Politecnico di Torino, I Faculty of Turin, 2009.

Laurea Specialistica in Mechanical Engineering, Politecnico di Torino, I Faculty of Turin, 2011.

Master of Science in Mechanical Engineering, University of Illinois at Chicago, 2012.